SUBBARRIER COULOMB EXCITATION AT REA3 – COMMISSIONING OF THE SEGA-JANUS EXPERIMENTAL SETUP

By

Eric Michael Lunderberg

A DISSERTATION

Submitted to
Michigan State University
in partial fulfillment of the requirements
for the degree of

Physics — Doctor of Philosophy

2017

ABSTRACT

SUBBARRIER COULOMB EXCITATION AT REA3 – COMMISSIONING OF THE
SEGA-JANUS EXPERIMENTAL SETUP

By

Eric Michael Lunderberg

A new experimental setup for low-energy Coulomb excitation was developed at NSCL
and commissioned at the general purpose beam line of the ReA3 reaccelerator facility. The
so-called SeGA-JANUS (Joint Array for NUclear Structure) setup combines γ-ray detec-
tion with the <u>Se</u>gmented <u>Ge</u> <u>A</u>rray (SeGA) with scattered particle detection using a pair
of segmented double-sided Si detectors. The low-energy Coulomb excitation program that
SeGA-JANUS will enable complements intermediate-energy Coulomb excitation studies that
have long been performed at NSCL by providing access to observables that quantify collec-
tivity beyond the first excited state and that are sensitive to the sign and magnitude of
quadrupole moments. This opens up new research opportunities now at NSCL and in the
future at FRIB where the variety of available beams and their intensity will greatly increase.

The commissioning experiment used stable ^{78}Kr beam. With (Z,N)=(36,42), ^{78}Kr has
enough valence protons and neutrons to exhibit collective structures that are strongly excited
in Coulomb scattering. In addition to being a noble gas and well-studied, this made ^{78}Kr
an ideal choice for the SeGA-JANUS commissioning.

In this work, the new detector setup, including data acquisition and analysis will be
presented. The deduced measures of collectivity and shape are compared to literature values.

Due to delays in the ReA3 readiness, this thesis also includes the experimental study of
neutron-rich sulfur isotopes with mass numbers A=38-42. This work used the GRETINA
setup at the S800 spectrograph and resulted in a peer-reviewed publication in Physical

Review C that is reproduced in Appendix C.

To Elisira, my wife, who has been with me throughout graduate school, giving me confidence and support.

ACKNOWLEDGMENTS

Throughout graduate school, I have enjoyed the continued support of friends, colleagues, mentors and family. My list of acknowledgements is by no means exhaustive, and I am thoroughly grateful to those named and unnamed for teaching, words of encouragement, assistance, camaraderie and companionship that made this dissertation possible, productive and enjoyable.

I thank all the members of the gamma group. My advisor, Professor Alexandra Gade, has given me continuous support. Any time, day or night, I know that I can drop into her office with a question about physics, and I will get an enthusiastic response. Often, I will not even be back to my office before I have received emails with more information and papers to read on the topic, thereby broadening my knowledge. I am grateful for this enthusiasm and modeling of the thought processes of a scientist. To Dr. Dirk Weisshaar, who has forgotten more about γ-ray detectors than I will ever know, thank you. Your Socratic dialogues about detectors do a marvelous job of emphasizing how simple detectors are in concept and yet how complicated they can be in execution. To Peter Bender, whose knowledge of physics and of ROOT are commendable, it was fun to talk about program design and deciding how we would jointly design and write the GRUTINIZER analysis package.

To my guidance committee, thank you. It has been a pleasure working with you, and I appreciate all the advice that has led me through the PhD process.

To everyone who has taken the SeGA filling pager, thank you. It is a grave and solemn duty to maintain the flow of liquid nitrogen to the detectors, being woken up in the middle of the night to come to the lab and cool a warming detector; it is a duty better borne together.

I acknowledge Dr. Paul DeYoung, who I worked with in undergrad and whose guidance

through research led me to the MoNA group, and then to NSCL as a graduate student. I pay you to think, is my favorite PDY phrase, pushing students to understand, and never to only work by rote action. Collaborators Ching-Yen Wu and Brian Bucher were instrumental in the setup and analysis of this experiment, and I am most grateful for all the help. I thank Shaofei Zhu, whose gracious sharing of GRETINA/CHICO2 spectra provided a marvelous point of comparison for the SeGA-JANUS setup.

To my mom and my older brother Mark, who preceded me in their own journeys through graduate school, thank you for your understanding and support. My first knowledge of the word dissertation was as a four-year old, learning that it meant not to enter Moms study for a while. Now dissertation means don't enter my office and I will be home later than expected! Your encouragement through the process of research and writing has been incredible.

To my *Dungeons and Dragons* group: who better to sit around a table in a dark basement room and escape from the world of physics for a while? May the adventures we had, unlike Harth and Garth, never be forgotten.

To anyone in the future reading this, I appreciate your dedication! Please know that this work was a labor of love and I hope for your success in all of your academic endeavors. I have a script watching for emails at thesis2017@lunderberg.com. Send an email that way, and it will let you know how many people have made it as far as you have.

Last, I thank my wife, Elisira. She has been supportive and caring, listening when I ramble about work, programming and physics, and still reminding me to nurture the other aspects of my life. In my thesis experiment, we would joke that she was effectively widowed and yet, through experiment and the remainder of the thesis process, I have known that however much time the lab claims, I can come home. Thank you.

TABLE OF CONTENTS

LIST OF TABLES

LIST OF FIGURES

Chapter 1

Introduction

1.1 Coulomb Excitation

The nuclear excitation induced by the electromagnetic field acting between colliding nuclei is referred to as Coulomb excitation. By restricting either the beam energy or the impact parameter through particle scattering angles, the projectile and target can be kept separated by more than the interaction distance of the short-range nuclear force. This technique enables an analysis that does not rely on a model of the nuclear force, allowing consideration of only excitations caused by the well-understood electromagnetic interactions [1].

The cross sections observed for the Coulomb excitation of individual final states in a nucleus are related to the transition matrix elements that connect the excited states with each other and the ground state. The cross sections can be deduced from the measured intensity of, for example, the γ-ray de-excitations of the level (see Fig. 1.1) relative to the number of projectiles and number density of the target. It is noted that, in principle, both the target and the projectile can be excited in the collision. Electric dipole (E1) and electric quadrupole (E2) modes are predominantly excited. E3 excitations are observed as well, while magnetic excitations are heavily suppressed at low beam energies [2] and will be neglected here as an excitation mechanism. In even-even nuclei, Coulomb excitation is mediated predominantly through E2 transition matrix elements that connect the low-lying

1

positive-parity yrast and yrare states.
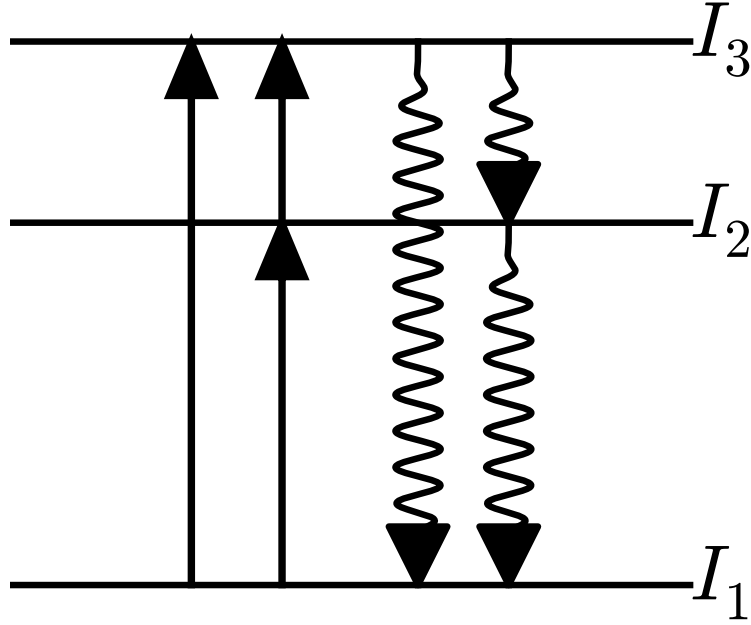
Figure 1.1: Excitations and de-excitations in a simplified 3-state system. Each upward arrow represents a path for Coulomb excitation. Each downward arrow represents de-excitation by γ-ray emission. The excitations create a population of excited states, which can then be tagged by spectroscopy of the subsequent γ-ray emission.

Electromagnetic transition matrix elements deduced from Coulomb excitation cross sections can be translated into the reduced electromagnetic transition strength, $B(\text{E2}; I_i \rightarrow I_f)$. In even-even nuclei, the $B(\text{E2}; 0_1^+ \rightarrow 2_1^+)$ reduced electric quadrupole excitation strength is used extensively as an indicator of collective excitations, such as rotations or vibrations, in which many nucleons outside of inert proton and neutron cores participate [3]. Near shell closures, where the number of valence nucleons available for collective motion is small, $B(\text{E2})$ values are small, while mid-shell, in between two magic numbers, the $B(\text{E2})$ strength is maximized, as shown in Fig. 1.2.

Coulomb excitation was first used to study stable nuclei [5, 6]. The nucleus to be studied was made into a target, which was then bombarded by ^{4}He nuclei or heavier ions such as ^{12}C
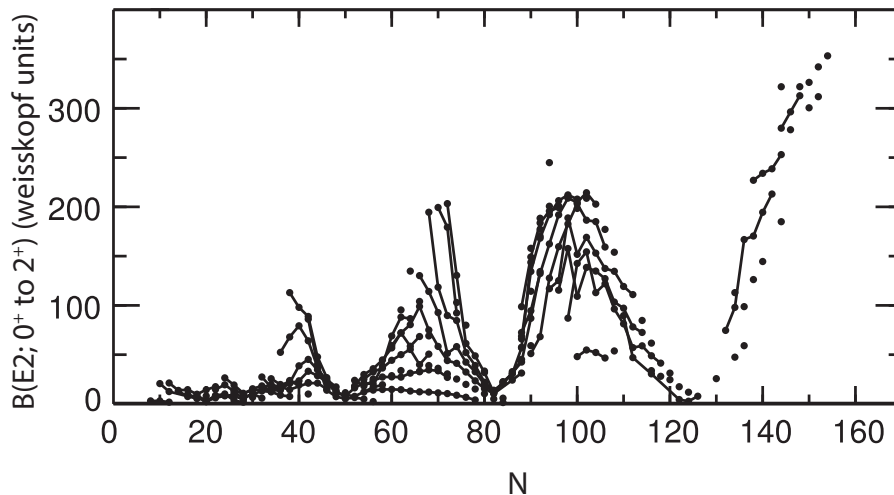
Figure 1.2: The $B(E2; 0_1^+ \rightarrow 2_1^+)$ transition strength for isotopic chains, shown here in Weisskopf units. Minima in the transition strength are clearly seen at magic numbers $N = 50, 82, 126$. (Figure adapted from [4].)

at energies below the Coulomb barrier. Coulomb excitation would excite states with spins as high as 30^+ in the yrast band [1], quantified through the detection of γ rays emitted by the target nucleus. The energy of the Coulomb barrier is as follows, where Z_P and Z_T are the proton number of the projectile and target, respectively, and A_P and A_T are the mass number of the projectile and target:

$$E_{\text{Coulomb barrier}} = \frac{1}{4\pi\epsilon_0} \frac{Z_P Z_T e^2}{r_{\text{min}}}, \tag{1.1}$$

$$r_{\text{min}} = \left[1.25 \left(A_P^{1/3} + A_T^{1/3} \right) + 5 \right] \text{fm}. \tag{1.2}$$

Here, r_{min} is the minimum distance allowed in a Coulomb excitation analysis. Its phenomenological description is based on interaction radius studies [1].

When rare isotopes became available for experiments, changes to the well-known nuclear shell structure [7, 8] were found and prompted experimental research programs world-wide. Since these short-lived nuclei cannot be made into targets and are available as beams of ions
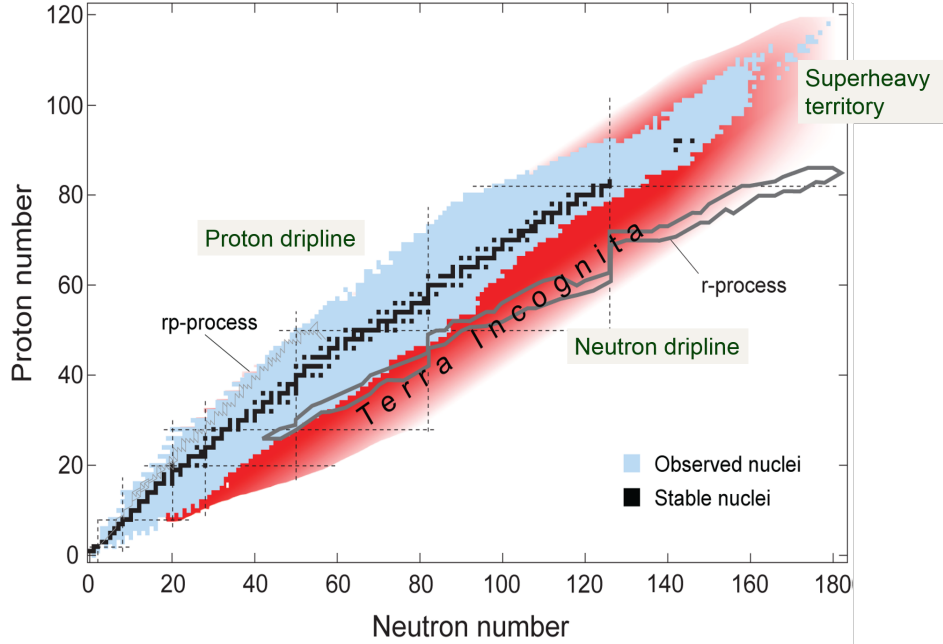
Figure 1.3: The chart of the nuclides, with selected features labeled. Stable nuclei are shown in black, observed unstable nuclei in blue, with the expected extent of all possible nuclei shown in red. Figure adapted from [9].

for experiments, well-established measurement techniques had to be adapted to deal with "inverse kinematics," a reaction scheme in which the nucleus of interest is the projectile. As shown in Fig. 1.3, the vast majority of isotopes are unstable, including key isotopes relevant for nuclear astrophysics along the r-process and rp-process paths.

The most exotic beams are created through projectile fragmentation at energies typically exceeding $100\,\mathrm{MeV/u}$ and subsequent in-flight separation [10]. After fragmentation and separation, the fragments are typically available at velocities exceeding $v/c \approx 0.3$. At these velocities, the collision between projectile and target occurs above the Coulomb barrier for all possible target-projectile combinations. Whereas earlier Coulomb excitation experiments could rely on sub-barrier energies to prevent nuclear interactions from occurring, these intermediate-energy Coulomb excitation experiments [11] consider only events that scatter at small scattering angles, which correspond to sufficiently large impact parameters. The exact

relationship between impact parameter and scattering angle is given in Eq. 1.3, where $\theta_{\text{max}}^{\text{cm}}$ is the maximum projectile scattering angle in the center of mass reference frame, $\beta = v/c$ is the beam velocity relative to the speed of light, $\gamma = \frac{1}{\sqrt{1-\beta^2}}$ is the Lorentz factor, Z_P and Z_T are the proton numbers of projectile and target, respectively, and m_0 is the reduced mass of the projectile-target system [11]:

$$b_{\text{min}} = \frac{a}{\gamma} \cot\left(\frac{\theta_{\text{max}}^{\text{cm}}}{2}\right) \tag{1.3}$$

$$a = \frac{Z_P Z_T e^2}{m_0 c^2 \beta^2}. \tag{1.4}$$

The higher beam energy also affects the range of states accessible in the Coulomb excitation process. The short interaction time of projectile and target at high collision velocities suppresses multi-step excitations and restricts the accessible states largely to the ones that can be excited from the ground state in a single step [12, 11]. This simplifies the analysis significantly, as each de-excitation γ ray observed corresponds to a single excitation path without feeding from higher-lying states reached in multiple steps. Using relativistic calculations developed by Alder and Winther, also in this regime, the observed Coulomb excitation cross sections were related to the $B(E2)$ transition strengths, such as $B(E2; 0_1^+ \rightarrow 2_1^+)$ in even-even nuclei [12]. In intermediate-energy Coulomb excitation, thick high-Z targets can be used, increasing luminosity and allowing for experiments at a few ions per second [11].

Inverse kinematic Coulomb excitation, was first pioneered at RIKEN to quantify the onset of collectivity as the neutron magic number $N = 20$ breaks down in exotic ^{32}Mg [13], and subsequently implemented at the National Superconducting Cyclotron Laboratory (NSCL) and other laboratories with beams in a similar energy regime. For example, using the Segmented Germanium Array (SeGA) to detect γ rays and the S800 spectrograph to

detect the scattered projectiles [14, 15, 16, 17, 18, 19], the $B(\text{E2}; 0_1^+ \rightarrow 2_1^+)$ values for a wide variety of rare isotopes were measured.

Extending low-energy Coulomb excitation to rare isotopes allows for more comprehensive measurements of these nuclei, accessing collectivity beyond the first excited state through multi-step excitations [1]. A particularly interesting case of a multi-step excitation can occur among the M-substates of a nuclear level. This so-called Coulomb nuclear reorientation allows experimental measurements of the magnitude and sign of the diagonal matrix element $\langle I||\mathcal{O}(\text{E2})||I\rangle$, which is related to the quadrupole moment [20]. The magnitude of the quadrupole moment quantifies the degree of deformation and its sign signals the shape as prolate or oblate. In the regime of rare isotopes, shape coexistence has been observed where magic numbers break down [21], and quantities that characterize shape become important.

At ISOL facilities, which complement facilities that use in-flight production and separation of rare isotopes, selected chemistry-dependent rare-isotope beams are available at a few MeV/u, around the Coulomb barrier of typical projectile-target combinations [22]. ISOL facilities produce rare isotopes by fragmentation of a heavy production target, for example uranium carbide, with a high-intensity proton beam. The fragments produced then diffuse out of the production target, are ionized, and are then accelerated to sub-barrier energies, in order to perform Coulomb excitation. Some recent highlights are as follows. At the TRIUMF-ISAC facility, studies of transitions in the radioactive nuclei ^{20,21}Na [23], ^{78,80}Zn [24], and ^{11}Be [25] have been performed. At CERN-ISOLDE, measurements of ^{220}Rn and ^{224}Ra have provided circumstantial evidence of octupole deformation [26], possibly relevant for electric dipole moment (EDM) searches, and isomeric beams of ^{68,70}Cu and ^{106,108}In have enabled the study of transition matrix elements based on isomeric states [27, 28]. A different method of beam production is employed by CARIBU, located at Argonne National

Laboratory (ANL), where a $1\,\text{Ci}$ ^{252}Cf source produces fission fragments, which are then thermalized in a gas catcher, extracted, charge-bred, and accelerated to a few MeV [29]. CARIBU has been used to perform low-energy Coulomb excitation experiments, measuring transition and diagonal matrix elements in ^{144,146}Ba [30, 31] and ^{110}Ru [32]. Such low-energy experiments typically require projectile intensities exceeding $10^4 - 10^5$ particles per second, and are therefore limited to less exotic nuclei as compared to intermediate-energy Coulomb excitation.

While ISOL facilities are limited to elements with a chemistry that allows extraction from a thick production target and CARIBU to ^{252}Cf fission fragments, with NSCL's new and world-unique scheme of in-flight production and separation, combined with subsequent beam thermalization in a gas cell, charge breeding, and re-acceleration [33], the element limitation is largely removed and in principle all isotopes produced at sufficient intensities can be made available as beams at Coulomb barrier energies for experiments. The variety of beams and intensities available will increase at the upcoming Facility for Rare-Isotope Beams (FRIB), extending the range of isotopes that can be studied with low-energy Coulomb excitation. With this in mind, the development of a new experimental setup designed for low-energy Coulomb excitation at the NSCL has been pursued and is the subject of this work, opening new opportunities to comprehensively assess collectivity and shapes in nuclei not otherwise available for such studies.

While γ-ray tagging can still be used at low energies, the scattering-angle range of the projectiles is essentially $180°$, requiring a more complete angle coverage for the particle detection system, in contrast to the strongly forward-focused scattered projectiles at intermediate beam energies. The Joint Array for NUclear Structure (JANUS), composed of two annular double-sided segmented silicon detectors surrounded by the Segmented Germanium Array

(SeGA) [34] for γ-ray detection, can detect particles scattering to large angles. With a solid angle coverage of 29% of 4π, and an effective solid angle coverage after projectile reconstruction from the target recoil of 78% of 4π (see Sec. 3.2.1), the JANUS system presented here is well-suited for low-energy Coulomb excitation.

The stable isotope ^{78}Kr was chosen as the in-beam commissioning beam, due to its high collectivity and ease of use as a noble gas. It has proton and neutron numbers of $Z = 36$ and $N = 42$, far from the nearest magic numbers of 28 and 50. As a result, it exhibits large $B(\mathrm{E2})$ transition strengths connecting the low-lying positive-parity states. As it is stable and gaseous, producing a beam of ^{78}Kr is a straightforward task. In addition, as ^{78}Kr has previously been studied using low-energy Coulomb excitation, existing work will provide a point of comparison, in order to verify the experimental scheme and data analysis.

In this work will be presented the commissioning experiment of the SeGA-JANUS experimental setup, performing low-energy Coulomb excitation of ^{78}Kr at the ReA3 facility at NSCL.

1.2 Transition and Diagonal Matrix Elements

In inverse-kinematics Coulomb excitation experiments, the Coulomb field of the target nucleus provides a time-dependent perturbation on top of the nuclear Hamiltonian that describes the projectile. The Coulomb field felt by the projectile can be approximated using the classical hyperbolic trajectory [35, 1]. By expanding the time-dependent wave function in terms of the unperturbed eigenstates, one can determine the outgoing nuclear states in a coupled channels calculation as shown below, where $\psi(t)$ is the time-dependent wave function of the projectile, H_0 is the unperturbed nuclear Hamiltonian, E_n and ϕ_n are the eigenvalues

and eigenstates of H_0, $a_n(t)$ are the excitation amplitudes, and $V(t)$ is the time-dependent potential generated by the target nucleus [1]:

$$i\hbar\dot{\psi}(t) = [H_0 + V(t)]\,\psi(t) \tag{1.5}$$

$$\psi(t) = \sum_n a_n(t)\phi_n \tag{1.6}$$

$$i\hbar\dot{a}_n(t) = \sum_m \langle n|V(t)|m\rangle \exp\left(\frac{i(E_n - E_m)t}{\hbar}\right) a_m(t). \tag{1.7}$$

The electromagnetic interaction $V(t)$ between the two extended nuclei is then expanded in terms of electric and magnetic multipoles [1, 2]. After mathematical transformations that can be found in [36], these coupled differential equations can be expressed in terms of the reduced transition matrix elements $\langle f||\mathcal{O}(\lambda)||i\rangle$, where $|i\rangle$ is the initial state, $\langle f|$ is the final state, and $\mathcal{O}(\lambda)$ is an operator for an electromagnetic transition with multipolarity λ.

The operators for the electric transition of multipolarity λ are given in Eq. 1.8, where Y_μ^λ are the spherical harmonics, e_{t_z} are the charge of the particle being integrated over, e is the elementary charge [4]:

$$\mathcal{O}(E\lambda) = r^\lambda Y_\mu^\lambda(\hat{\boldsymbol{r}})e_{t_z}e, \tag{1.8}$$

$$\text{e.g. } \langle f||\mathcal{O}(E2)||i\rangle = \left\langle f\left|\left|(r^2 e_{t_z}e)Y_\mu^2(\hat{\boldsymbol{r}})\right|\right|i\right\rangle. \tag{1.9}$$

$B(E\lambda)$ transition strengths are a useful quantity derived from the transition matrix elements, as defined in Eq. 1.10. $B(E2)$ values are often expressed in terms of Weisskopf units (plotted in Fig. 1.2, which remove the dependency of the transition strength on the nucleon

number [4]:

$$B(\text{E2}; i \to f) = \frac{\langle f||\mathcal{O}(\text{E2})||i\rangle^2}{2J_i + 1}, \tag{1.10}$$

$$B_{\text{w.u.}}(\text{E}\lambda) = \left(\frac{1}{4\pi}\right)\left[\frac{3}{3+\lambda}\right]^2 \left(1.2A^{1/3}\right)^{2\lambda} e^2 \text{ fm}^{2\lambda}, \tag{1.11}$$

$$B_{\text{w.u.}}(\text{E2}) = 0.0594A^{4/3}e^2 \text{ fm}^4. \tag{1.12}$$

While off-diagonal transition matrix elements characterize the transition between two states, diagonal matrix elements $\langle J||\mathcal{O}(\text{E}\lambda)||J\rangle$ describe transitions between magnetic M sub-states of the same J^{π} state, and are related to the spectroscopic quadrupole moment [37]:

$$Q = \sqrt{\frac{16\pi}{5}} \frac{\langle J \ J \ 2 \ 0|J \ J\rangle}{\sqrt{2J+1}} \langle J||\mathcal{O}(\text{E2})||J\rangle. \tag{1.13}$$

Inside a strong electric field gradient, there is a strong time-dependent interaction energy, given in Eq. 1.14 [20]:

$$E(t) = \frac{eQZ}{r^3(t)} \left(\frac{3M^2 - J(J+1)}{4J(2J-1)}\right). \tag{1.14}$$

This interaction energy will cause spin-degenerate energies to split into the M sub-states, as shown in Fig. 1.4. This splitting is sizable, for example typically on the order of $\sim 100\,\text{keV}$ when oxygen ions are used as probe [20]. Since the splitting depends on both the magnitude and sign of Q, magnetic substates of prolate nuclei ($Q < 0$) and oblate nuclei ($Q > 0$) will be split in opposite directions.

The obvious effect of this splitting is that some of the M states will be lower in energy,
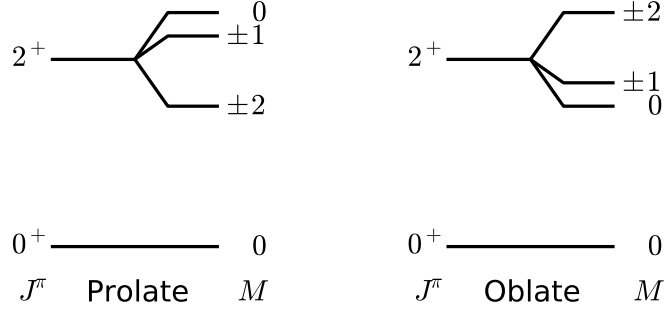
Figure 1.4: The energy splitting caused by a strong electric field, as described in Eq.1.14. The energy splitting is fairly large, for example on the order of $\sim 100\,\text{keV}$ when using oxygen as the probe [20]. As oblate and prolate nuclei have quadrupole moments with opposite signs, their spin-degenerate substates are split in the opposite direction.

and therefore be preferentially populated in Coulomb excitation, causing a polarization effect for the Coulomb scattered particles [20]. For this reason, this effect is known as the "reorientation effect." The more prominent effect for the purpose of a low-energy Coulomb excitation analysis is a change in the angle-dependent excitation probability. The excitation probability depends strongly on the difference in energy between the initial and final states. By altering the energy of some of the spin-degenerate substates, the reorientation effect will cause changes to the excitation probabilities [20].

When two nuclei scatter off each other, the largest scattering angles correspond to the smallest impact parameters. Since the magnitude of the quadrupole interaction energy depends on $\frac{1}{r^3}$ as shown in Eq. 1.14, events occurring at large scattering angles will have a much larger splitting of spin-degenerate substates, and will be affected by the reorientation

effect more strongly. One can then quantify the reorientation effect and so access information on the shape by measuring the Coulomb excitation cross section for a state in different scattering angle regions.

For example, in the case of a projectile with spin 0^+ beam impinged on a target with the same spin, only the $M = 0$ substate of the 2^+ state can be populated. In a prolate nucleus, the $M = 0$ substate will be at higher energies when the projectile scatters at backward angles than at forward angles, and so the 2^+ state will have a lower excitation cross section. An oblate nucleus, on the other hand, will have a decreased energy of the $M = 0$ substate at large scattering angles, and will therefore have a larger excitation cross section to the 2^+ state. By comparing the excitation cross section observed at high scattering angles relative to that observed at low scattering angles, one obtains a clear experimental signature to distinguish between prolate and oblate shapes.

Unlike intermediate-energy Coulomb excitation, which can only probe states accessible in a single step from the ground state [11], low-energy Coulomb excitation can excite a nucleus in multiple steps, probing higher excited states that form collective structures such as rotational bands [1]. The prevalence of multi-step excitations in low-energy Coulomb scattering, including the reorientation effect which is a two-step excitation into the magnetic substates of a level, leads to an extensive network of coupled differential equations (see Eq. 1.7). In practice, computer codes that model the semi-classical Coulomb excitation theory are used to extract matrix elements from large sets of yields or cross sections measured for different scattering angle ranges. The most modern code, GOSIA [36, 38, 1], takes as input the efficiency-corrected γ-ray yields that signal the direct and indirect population of excited states and, in an involved χ^2 minimization, provides a set of transition and diagonal matrix elements that describe the measured data.

Gosia was designed and optimized to perform such high-dimensional χ^2 minimization. Gosia uses analytic approximations to increase the speed of the minimization, and can fit up to 200 matrix elements simultaneously to measured yields of the directly and indirectly populated states. In addition, previous measurements of lifetimes, multipole mixing ratios, and branching ratios can be used as additional components of the χ^2 calculation, helping to constrain matrix elements that are not otherwise well-constrained by the measured yields, without introducing model dependency.

Chapter 2

Experimental Setup

In an inverse kinematics low-energy Coulomb excitation experiment, a projectile nucleus impinges on a stationary target, and is excited in the Coulomb field of the target nuclei. Detection of de-excitation γ rays emitted from the scattered projectile is used to tag and quantify the population of states resulting from the Coulomb excitation process.

The SeGA-JANUS setup consists of two main parts: particle detectors, composed of silicon semiconductors, to detect scattered projectiles or recoiling target nuclei, and γ-ray detectors, consisting of high-purity germanium, to detect the de-excitation γ rays. Fig. 2.1 shows an illustration of the major parts of the setup.

2.1 Particle Detection

2.1.1 Principles

As charged particles pass through matter, they deposit energy into the surrounding material. This occurs primarily through inelastic collisions with electrons in the material, with each electron carrying away a small portion of the energy. These electron inelastic collisions transfer energy to the electrons, resulting either in excitations of atomic levels or in ionization of atoms in the surrounding material. Since the cross sections for these collisions are quite high, on the order of 100 megabarns [39], a large number of collisions occur over a short

14
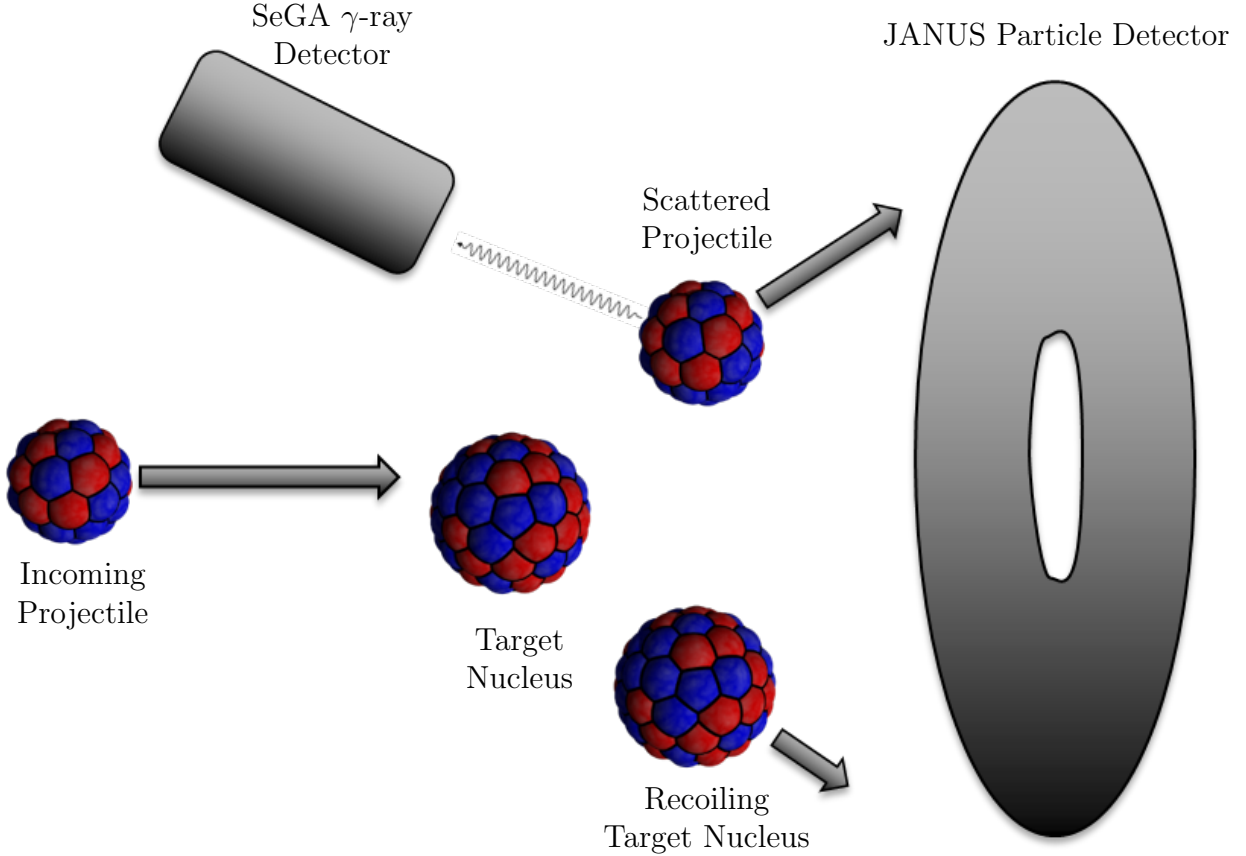
Figure 2.1: An illustration of the experimental setup, showing a projectile scattering off of a target nucleus, and subsequently emitting a γ ray. The scattered and recoiling nuclei are detected in the JANUS particle detectors, while the emitted γ rays are detected in the SeGA detectors.

distance, each removing a small amount of energy from the heavy ion, one can consider the stopping power $\frac{dE}{dx}$ of a material, rather than treating each collision individually.

Since each electron carries away only a small portion of the total energy of the passing charged particle, a classical approximation of the energy loss can be performed by determining the energy imparted to an electron by a heavy particle of constant velocity [39]. The energy loss per collision is then as follows, where Z is the charge of the heavy ion, e is the electron charge, m_e is the electron mass, v is the velocity of the heavy ion, and b is the

impact parameter:

$$\Delta E = \frac{2Z^2 e^4}{m_e v^2 b^2}. \tag{2.1}$$

For a beam of $3.9\,\mathrm{MeV/u}$ $^{78}\mathrm{Kr}$, with reasonable values of the impact parameter b, this results in energy losses per collision of a few eV up to a few keV. This validates the earlier assumption that only a small amount of energy is transferred to an individual electron. Following this classical approach, averaging over many such collisions in a solid, leads to the following formula for the differential energy loss, where N_e is the density of electrons in the material, $\gamma = \frac{1}{\sqrt{1-v^2/c^2}}$, and $\bar{\nu}$ is the mean frequency of revolution of a bound electron around the nucleus in the material:

$$\frac{dE}{dx} = -\frac{4\pi Z^2 e^4}{m_e v^2} N_e \ln\left(\frac{\gamma^2 m_e v^3}{Z e^2 \bar{\nu}}\right). \tag{2.2}$$

A fully quantum mechanical description of the inelastic collision between energetic heavy ions and the electrons in a medium yields the Bethe-Bloch equation, where N_a is Avagadro's number, r_e is the classical electron radius, m_e is the electron mass, c is the speed of light, z and A are the atomic number and mass of the absorbing material, Z is the charge of the heavy ion, β is the v/c of the heavy ion, $\gamma = \frac{1}{\sqrt{1-\beta^2}}$, I is the mean excitation potential of the absorbing material, and W_{max} is the maximum energy transfer to an electron in a single collision [39]:

$$\frac{dE}{dx} = -2\pi N_a r_e^2 m_e c^2 \rho \frac{z}{A}\frac{Z^2}{\beta^2}\left[\ln\left(\frac{2m_e\gamma^2 v^2 W_{\mathrm{max}}}{I^2} - 2\beta^2\right)\right]. \tag{2.3}$$

Modern calculations, such as those performed by SRIM [40], are based on the Bethe-Bloch

16

equation, with additional corrections applied.

In a semiconductor detector, such as a silicon detector used here for particle detection, energy deposited in the material is converted into a proportional number of electron-hole pairs in the band structure of the semiconductor. In the electric field of the applied bias voltage, the electrons and holes travel to the corresponding contacts, and can be collected and measured as a charge, usually with a charge-sensitive preamplifier. The amplitude of the voltage signal delivered by the preamplifier is proportional to the energy deposited in the detector. The contacts of the semiconductor detector can be segmented, and by identifying the contact segments which collected the charges enables inference of the location where the particle interacted within the detector, thus providing position sensitivity.

2.1.2   JANUS Particle Detection

The Joint Array for Nuclear Structure (JANUS) consists of two S3 detectors manufactured by Micron Technology, Inc. These are annular double-sided silicon detectors, each with an inner radius of 1.1 cm, and an outer radius of 3.5 cm. Each detector has at one surface a 24-fold segmentation in the radial direction, and on the other surface a 32-fold segmentation in the ϕ direction. By recording in which ring and which sector energy was deposited, the pixel of interaction can be determined, as shown in Fig. 2.2. In this geometry, the S3 detector delivers 56 signals, but establishes a segmentation into 768 pixels of about 1 mm by 5 mm in size each. At a typical distance of 3.0 cm from a particle source, this translates to an angular resolution of about $1.5°$ in θ and $11.25°$ in ϕ.

The upstream detector had a thickness of $302 \, \mu$m, and the downstream detector had a thickness of $313 \, \mu$m. Based on SRIM calculations [40], the ^{78}Kr ions will stop in under $50 \, \mu$m of silicon, so the full energy of the ions will be deposited and measured.
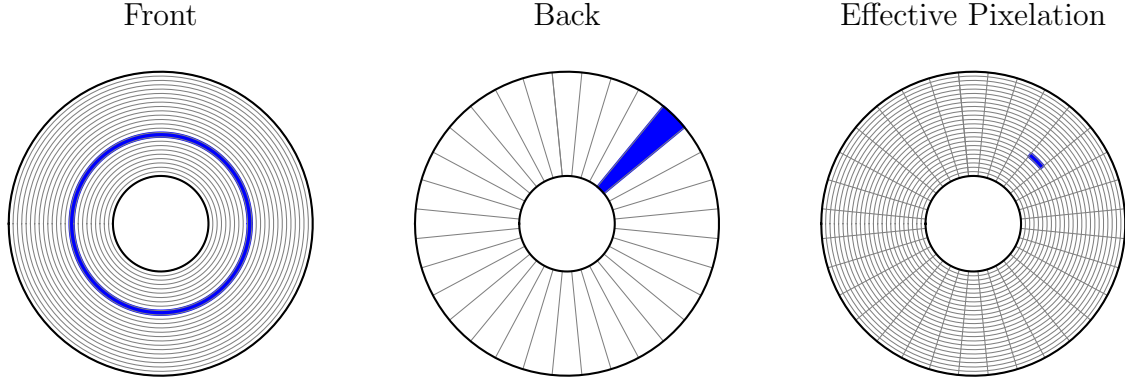
Figure 2.2: The segmentation in rings on one surface and in sectors on the other of a JANUS S3 detector. Shown in blue is a hypothetical energy deposition into a ring and sector, with the corresponding pixel in which energy was deposited.

The detectors were placed perpendicular to the path of the beam, one at 3.0 cm upstream of the target position, and one at 3.0 cm downstream of the target position. This gave angular coverage at scattering angles of 20.1-49.4° in the downstream detector, and 130.6-159.9° in the upstream detector.

The JANUS assembly is shown in Fig. 2.3, with both detectors, the target wheel, and an upstream 5 mm aperture. The target assembly contains two thin-foil targets, one empty frame, and one 3 mm aperture. A wire is connected to each aperture allowing beam current deposited on the apertures to be measured for beam-tuning purposes. In addition, the target assembly can be given a positive high voltage. This suppresses the emission of δ electrons[1] from the target into the JANUS detector, which would otherwise become background in the detector spectrum.

A bias voltage of 40 V was applied across each detector. As the bias voltage was increased, the leakage current was observed to increase linearly at low voltages before leveling off. This indicates that the detectors were fully biased, and were no longer in the ohmic region.

---

[1] δ electrons are secondary electrons produced by the projectile passing through the target that have sufficient energy to leave the target.
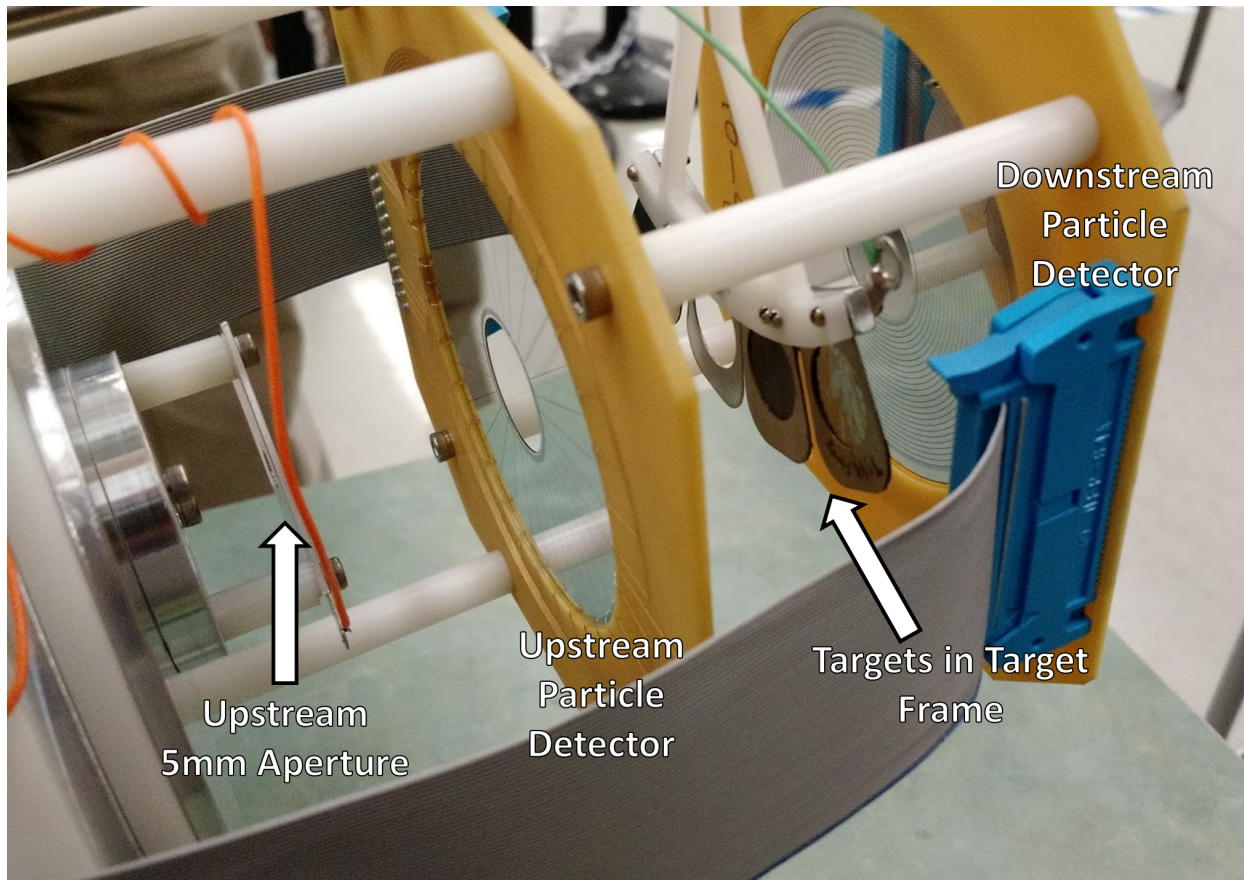
Figure 2.3: The target position of the JANUS assembly. Shown here are the two silicon detectors that compose JANUS, with the target wheel mounted between them. From left to right, the target frame contains a $3\,\mathrm{mm}$ aperture, an empty frame, a ^{208}Pb target, and a ^{48}Ti target. The target wheel is operated manually through a rod system that is not shown here. The orange and green wires allow collected charge on the apertures to be measured, for beam-tuning purposes.

The 112 signals from JANUS were pre-amplified using preamplifiers provided by Swan Research, before being shaped using Shaper/Discriminator modules manufactured by PICO Systems, which were controlled through a CAMAC interface. The shaped output of these modules was sent to CAEN v785 analog-to-digital converters (ADCs) , while a secondary output signal was sent to CAEN v775 time-to-digital converters (TDCs). The ADC and TDC modules were read out through a VME interface. The output trigger signal from the Shaper/Discriminator modules was used to generate the trigger condition for the complete JANUS system.

The PICO shaper has an input range of $500\,\mathrm{mV}$, while the silicon signal is expected to have an amplitude of $\sim 1\,\mathrm{V}$ for energy deposition of $300\,\mathrm{MeV}$, expected for projectiles detected in typical in-beam experiments. Therefore, a simple attenuator consisting of a $100\,\Omega$ resistor was used to attenuate the output signal from the preamplifiers, prior to being sent to the PICO shapers. This was necessary only for the downstream JANUS detector, as discussed in Sec. 3.2.1.

To reduce triggering on noise, while still operating at a low particle energy threshold, a coincidence between the two sides of a single detector was required to trigger the readout of JANUS.

2.2   Gamma-Ray Detection

2.2.1   Principles

In order to detect a γ ray, it must first interact with the bulk material of a detector to produce a charged particle. There are three ways in which γ rays can interact with the electrons of the detector material: photoabsorption, Compton scattering, and pair production. The cross

section for these three interactions in bulk germanium as a function of γ-ray energy is shown in Fig. 2.4.
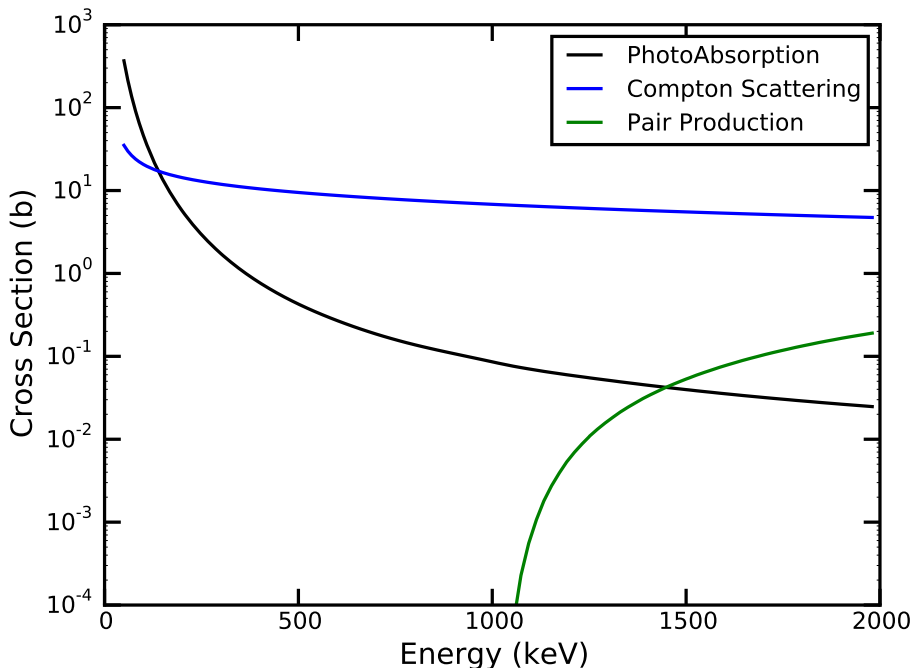
Figure 2.4: Reaction probabilities of each interaction of a photon in a germanium detector. Cross-section values taken from Ref. [41]

First, the photon can undergo photoabsorption, transferring its entire energy to an electron. This results in the full energy of the photon being detected, which is the ideal situation. This is the primary effect for low-energy γ rays.

Second, the photon can scatter off an electron, a process known as Compton scattering. If the photon Compton scatters, then only the energy imparted on the electron is detected. This results in a continuous distribution of energy at less than the full energy of the γ ray. There is a maximum amount of energy that can be transferred in a single scattering, occurring when the γ ray scatters at $180°$, which is less than the full energy of the γ ray. This results in a sharp cutoff, known as the Compton edge. The scattered γ ray may interact with the detector multiple times, losing energy with each scattering event. This brings the energy

21

of the photon down to the region where photoabsorption is dominant, at which point it may be absorbed. In this way, a series of Compton scatters may conclude with a photoabsorption event, contributing ultimately to the full energy peak.

Finally, the photon can undergo pair production, producing an electron/positron pair. In this case, some amount of kinetic energy is transferred to the electron and positron, and is deposited directly into the detector. The positron will later undergo pair annihilation with an electron, producing two γ rays at $511\,\text{keV}$. One or both of these γ rays may escape from the detector, producing the single- and double-escape peaks located at $511\,\text{keV}$ and $1022\,\text{keV}$ below the initial energy of the photon. By conservation of energy, this process is limited to photons with more than $2m_ec^2 = 1022\,\text{keV}$ of energy.

The idealized result of the three interactions is shown in Fig. 2.5 with the example of a $3\,\text{MeV}$ γ ray interacting with a germanium detector.
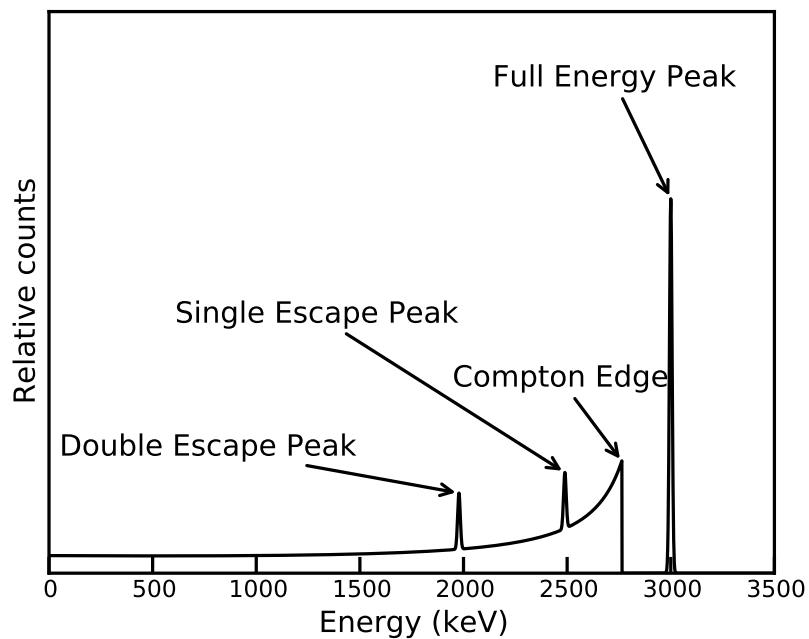
Figure 2.5: Idealized γ-ray energy spectrum of a $3\,\text{MeV}$ γ-ray, showing characteristic features.

2.2.2 Doppler Shift of γ Rays

In experiments using inverse kinematics, the excitation of the beam particle is of interest.

Since the scattered beam particle is moving at a significant fraction of the speed of light, the

γ-ray energies signaling its de-excitation will be Doppler shifted when observed in the lab

frame. That is, while the energy of the γ ray is well-defined in the rest frame of the excited

nucleus, the γ-ray energy as detected in the lab frame depends on the emitter velocity v/c

and the angle between the direction of motion of the nucleus and the direction of the emitted

γ ray, as shown schematically in Fig. 2.6.
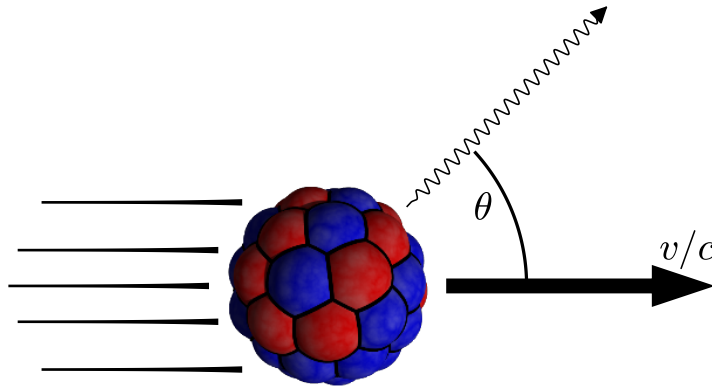
Figure 2.6: Kinematics for the Doppler boost of a γ ray emitted from a nucleus in motion. All vectors shown are in the laboratory frame of reference.

When the direction of the outgoing particle and γ ray are both measured, the energy of

the γ ray in the rest frame of the nucleus can be reconstructed as follows. Here, $\beta = v/c$,

$\gamma = \sqrt{\frac{1}{1-\beta^2}}$, and θ is the relative angle between the outgoing particle and the γ ray, as

measured in the lab frame:

$$E_{\text{rest}} = E_{\text{lab}}\gamma(1 - \beta\cos\theta). \tag{2.4}$$

The uncertainty of the resulting reconstruction depends on the uncertainties of E_{lab}, β, and θ. Each term contributes differently, based on the angle of emission of the γ ray. An uncertainty in β has the smallest effect close to $90°$, while an uncertainty in θ has the smallest effect close to $0°$ and $180°$. The contributions to the uncertainties are shown in Fig. 2.7, for conditions similar to those in the commissioning experiment, and can be derived from Eq. 2.4 by means of finite-difference derivatives, and the result can be found for example in Fig. [11].
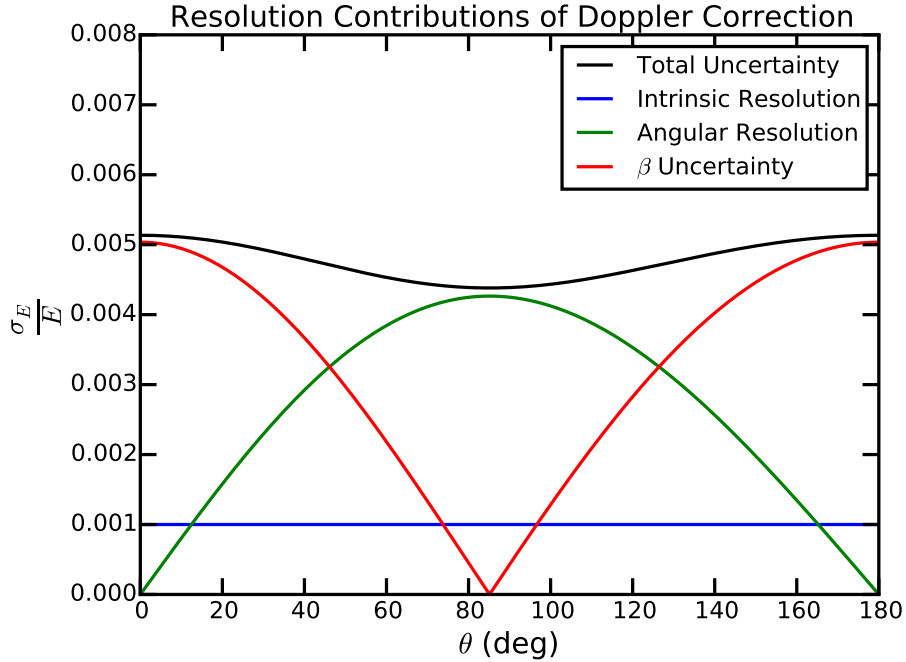
Figure 2.7: The effect of each experimental uncertainty on the Doppler reconstruction, as a function of emission angle, based on equations from [11]. This plot was generated using $\beta = 8.5(5)\%$, $\sigma_\theta = 3°$, and relative intrinsic resolution $\sigma_{E_{\text{lab}}} = 0.1\%$. In this plot, σ_E is used instead of full width at half maximum (FWHM), where $\text{FWHM} = 2.355\sigma_E$

2.2.3 SeGA

The Segmented Germanium Array (SeGA) consists of 16 32-fold segmented high-purity germanium detectors. Each crystal is 80 mm long and 70 mm in diameter. The crystals are segmented into 8 layers laterally, with each layer being divided into 4 quadrants, as shown in Fig. 2.8.
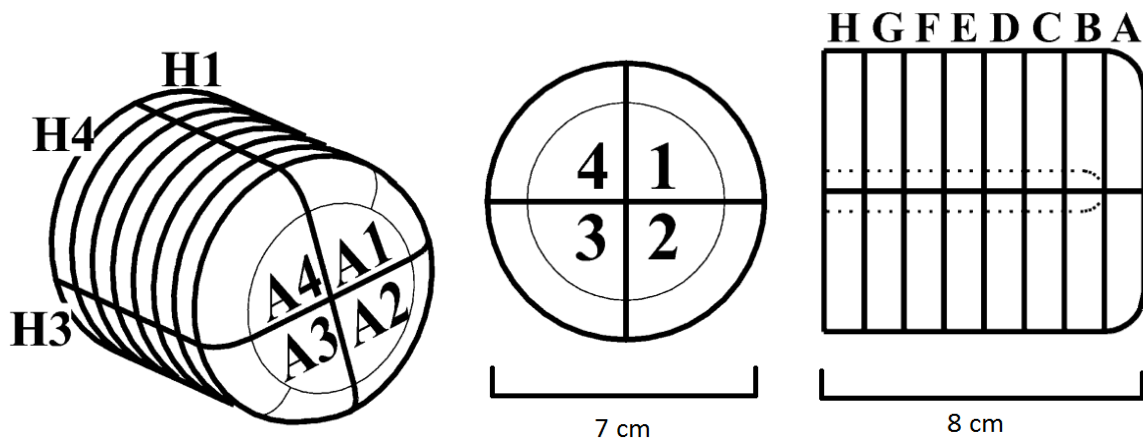
Figure 2.8: The segmentation of a single SeGA crystal, as shown from front, side, and diagonal perspectives. Figure adapted from [34].

While silicon's larger band gap of 1.1 eV allows for operation of silicon detectors at room temperature, the large leakage current that would result from thermal excitations across germanium's smaller band gap of 0.7 eV prevents operation of germanium detectors at room temperature [42]. Liquid nitrogen is used to cool the SeGA detectors to operational temperature of about 100 K, preventing thermal excitations of electrons across the band gap. Each SeGA detector assembly consists of the germanium crystal, preamplifiers, and a liquid nitrogen dewar, as shown in Fig. 2.9. The detectors are arranged around the target position as shown in Fig. 2.10. This setup is known as the barrel configuration, and maximizes the solid angle coverage of SeGA.

Electrons are collected at the single central contact, and holes at the segment contact.

25

Figure 2.9: A single SeGA detector, outside of the experimental setup. The green cylinder is the liquid nitrogen dewar, with the germanium crystal at the bottom of the image. The preamplifiers are contained inside the metal casing.

The central contact therefore delivers the total energy of the γ-ray energy absorbed in the detector, while the segment gives position-sensitive information about where within the detector the γ-ray interactions occurred.

The charges collected on the segment contacts are used for position determination. For Doppler-shift reconstruction, the location of the first interaction of the γ ray is required. For that, the segment with the highest energy deposition is chosen. The detection position is then used to determine the γ-ray emission angle as part of the Doppler correction, as described in Sec. 2.2.1. Each segment is 1 cm long, given an opening angle of $5.8°$. This is approximated in Fig. 2.7 with $\sigma_\theta = 2°$.

Each detector assembly contains charge-sensitive preamplifiers. The preamplified signals were then digitized using 100 MHz PIXIE-16 modules from the manufacturer XIA. Digitizer-based electronics such as the PIXIE-16 system have many benefits over analog electronics
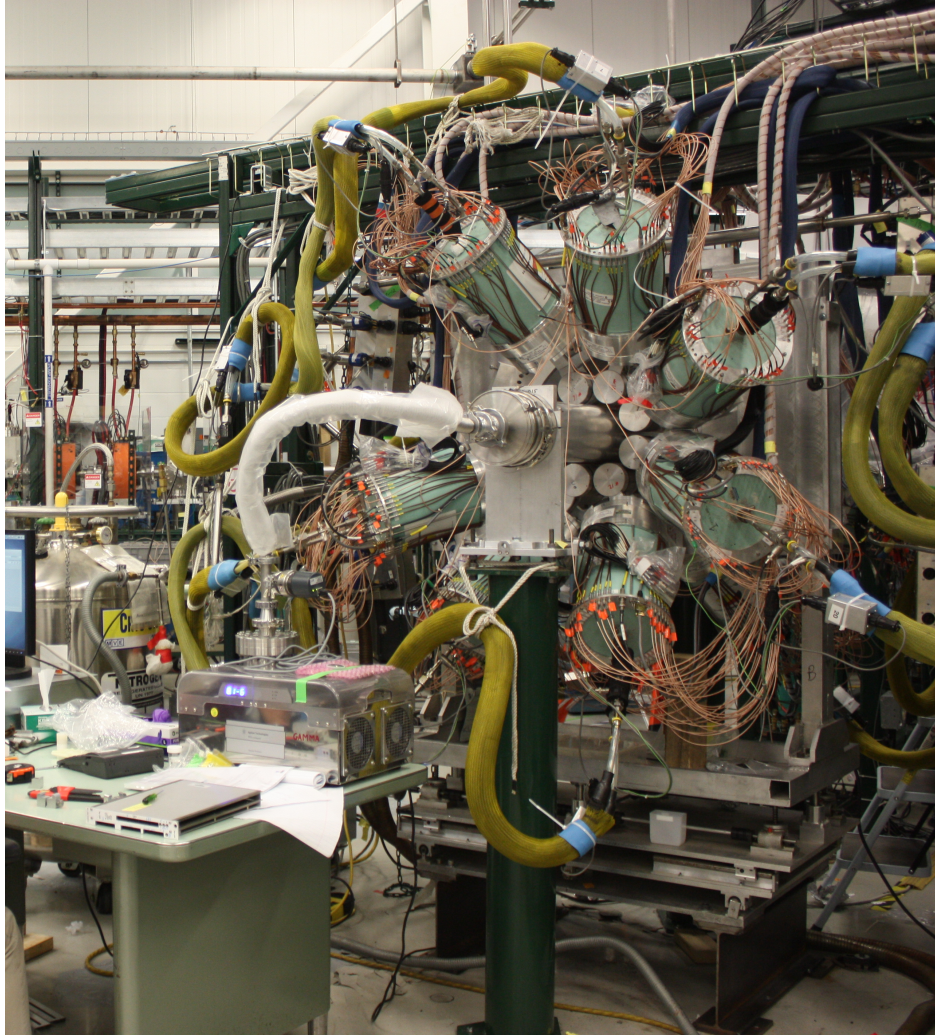
Figure 2.10: The SeGA array positioned around the target chamber. Photograph © 2016 NSCL.

such as shaper modules or discriminators for the processing of detector signals. The overall setup is simpler, as the digitizers take the role of a shaper, discriminator, analog-to-digital converter, and time-to-digital converter in one module. In addition, the PIXIE-16 cards can record the waveform of its input signal as a function of time. The waveforms captured can be used to improve the position resolution of the SeGA detectors, determining the position of the γ-ray interaction within a segment. The radial position can be determined by the shape of the waveform of the central contact, while the axial and azimuthal positions can be

determined by the size of transient signals observed on neighboring segments. The algorithms necessary to determine the interaction location and their applicability to SeGA are discussed in detail in the thesis of S.R. Stroberg [43]. Sub-segment resolution was not required for this study of ^{78}Kr, and was not used in the present work.

Each central contact was allowed to generate a trigger on a leading-edge threshold. When the central contact triggers, all segments in the associated detector are also read out. For each channel, an energy, time, and trace were recorded at a 100 MHz sampling frequency. The trace length for each central contact was 1 μs, and the trace length for each segment was 2.5 μs. The total data collected for each γ ray detected was approximately 16.7 kB.

Each detector contains 32 segments and the central contact, for a total of 33 channels. Using the full array of 16 detectors, a single XIA crate^2 could not contain sufficient PIXIE-16 modules to equip all channels. Three separate XIA crates were used to record all $33*16 = 528$ channels. The data acquisition system was run in a timestamped mode, where each channel was registered along with the time at which it occurred, allowing offline reconstruction of full events. A clock signal generated was distributed to all PIXIE-16 modules, as described in [44]. No drift between the timestamps recorded in each crate was observed.

The system was limited to a γ-ray detection rate of about 1.2 kHz. This limit is imposed primarily by the data throughput, that is the transfer of data from the XIA crates to the computer. At the time of this experiment, the maximum data transfer rate was approximately 6-7 MB/s per crate, or 18-21 MB/s for the entire setup. With a per-event size of 16.7 kB, this corresponds to a system-wide limit of ≈ 1.2 kHz. The observed background rate of 75 Hz per detector already exhausts this limit, before accounting for any beam-induced

---

^{2}The PIXIE-16 cards need a dedicated mainframe provided by the company XIA that are referred to as XIA crates in this work.

γ rays. In order to reduce the background rate, the system was gated on the beam spill of the reaccelerator (see Sec. 3.1.1). A 30 ms gate around the 10 ms beam period allowed for a reduction in the background rate by a factor of 5. The throughput limitation is primarily exhausted due to the acquisition of trace data. If no trace data were recorded, each event would be smaller by a factor of 30, resulting in a factor of 30 increase in the maximum γ-ray event rate.

2.3   Data Acquisition

The data was read out using the NSCLDAQ framework [45]. This framework allows for the operation of multiple independent data acquisition systems, which are then merged into a single output data stream. In this experiment, there were four separate computers, three for the three XIA crates, and one for controlling the CAMAC and VME crates. The NSCLDAQ framework provided a uniform way to start all four data acquisition systems, transfer the recorded data to a single computer, merge all four data streams into a single output, and write the resulting data to disk.

In order to correlate particle detections in JANUS and γ-ray detections in SeGA, all events were timestamped. The SeGA events, being recorded with PIXIE modules, have a timestamp already built into the data structure. The JANUS timestamp was generated from the 50 MHz clock signal, provided by the PIXIE modules, and recorded in a SIS3820 scaler module. Unlike other scaler modules in this setup, which provide periodic diagnostics, this scaler module was read out for each event. In addition, the module was set to the "deep counter" mode, where it registers two 48-bit counters, rather than sixteen 32-bit counters. This was necessary as a 50 MHz counter would overflow a 32-bit counter in 86 seconds,

whereas a 48-bit counter would require 65 days to overflow.

As the clock signal provided by the PIXIE modules starts somewhat before the PIXIE modules themselves start counting, it is necessary to gate the clock signal based on whether the PIXIE modules are in a running state. Otherwise, the JANUS electronics will start counting earlier than the PIXIE modules, resulting in a significant timestamp offset, on the order of hundreds of milliseconds.

Each SeGA central contact needs to be self-triggering, validated on the beam extraction period of the EBIT (see Sec. 3.1.1), with the segments being read out whenever the corresponding central contact triggers. This is done primarily using the front panel diagnostics of the PIXIE modules. To validate the central contact signals, the logical OR of all triggers is taken from the front panel. The logical AND of this signal with the validation signal from the beam spill is produced, with the resulting signal being sent back to the central contact module as an external validation. Simply sending the validation signal directly into the module will result in undesired behavior, as the PIXIE modules recognize transitions in the external validation, rather than the absolute value. On each transition to a high voltage, the PIXIE module opens a validation window, with a configurable length of up to a few μs. For validation with the beam spill, which lasts tens of milliseconds, it is necessary to construct the more elaborate validation signal, which gives a transition on each self-trigger, but only if the beam spill validation is present.

To trigger the segment modules, the central contact self-triggers are first sent to the backplane of the XIA crate, then a custom circuit board sends each central contact trigger to an individual LEMO connector. Using analog logic modules, each trigger signal is gated on the beam spill validation, and is then sent to the corresponding segment modules as an external trigger.

The trigger for JANUS is done entirely through analog logic. Each JANUS detector has 32 sectors and 24 rings, and each PICO Shaper/Discriminator module is set up to process either 16 sectors of a single detector, 16 rings of a single detector, or 8 rings of a single detector. Each PICO module has as an output the logical OR of all of its channels. These are used to generate the raw trigger from ring/sector coincidences for each detector, as shown in Fig. 2.11. This raw trigger is then gated on the current status of the VME crate, and the current run status of the XIA crate, in order to generate the live trigger.
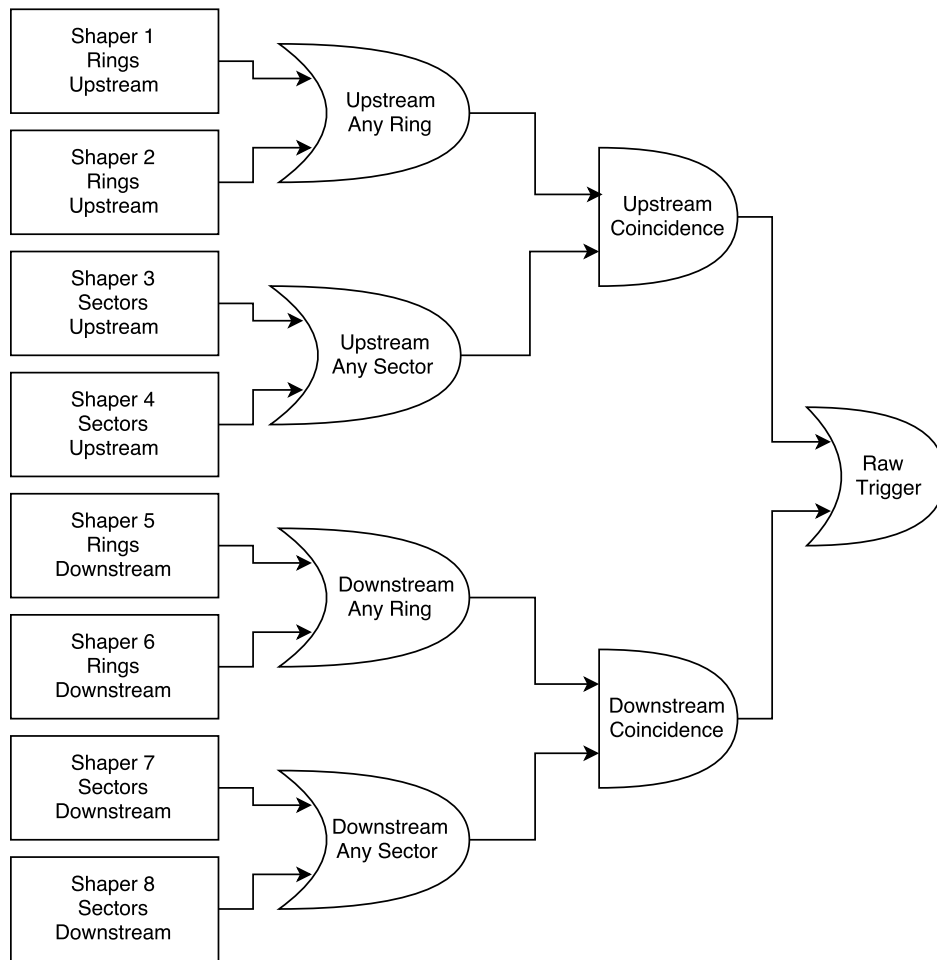
Figure 2.11: The trigger logic for the JANUS setup, generating the raw trigger from the individual channel triggers.

2.4 Testing of SeGA-JANUS with a ^{252}Cf Source

The experimental setup was tested using a thin-walled ^{252}Cf source. ^{252}Cf undergoes spontaneous fission, producing fission fragments that can be in an excited state. These excited fission fragments then deexcite, emitting γ-rays while in-flight, typically at v/c of 3-4%. This produces a Doppler shift based on the relative angle between the fission fragment and the emitted γ-ray.

Since the ^{252}Cf source provides correlated fission fragments and γ rays, it can be used to test the integration of the SeGA and JANUS systems, rather than testing each system in isolation. This test can confirm that the two systems are triggering simultaneously, that the timestamps between the two systems are synchronized, and that the relative position between the two systems is well-known.

When ^{252}Cf undergoes spontaneous fission, it splits into two fragments. These fragments are typically of unequal mass, as shown in Fig. 2.12, and are emitted directly opposite from each other, according to conservation of momentum. This symmetry, along with the symmetry of the upstream and downstream JANUS detectors, causes two fission fragments to be detected simultaneously with a high probability. Since the relative angle between the fission fragment and the γ ray is necessary to perform Doppler reconstruction, one must select which detected fission fragment emitted the γ ray. This is done by selecting either the fragment with higher or lower kinetic energy. In order to select the lower-mass fragments associated with the most intense γ-ray transitions, events with higher energy deposition in the particle detectors are selected.

This selection of fission fragments is an additional complication as compared to the in-beam commissioning, where due to the kinematics and detector layout, when a scattering
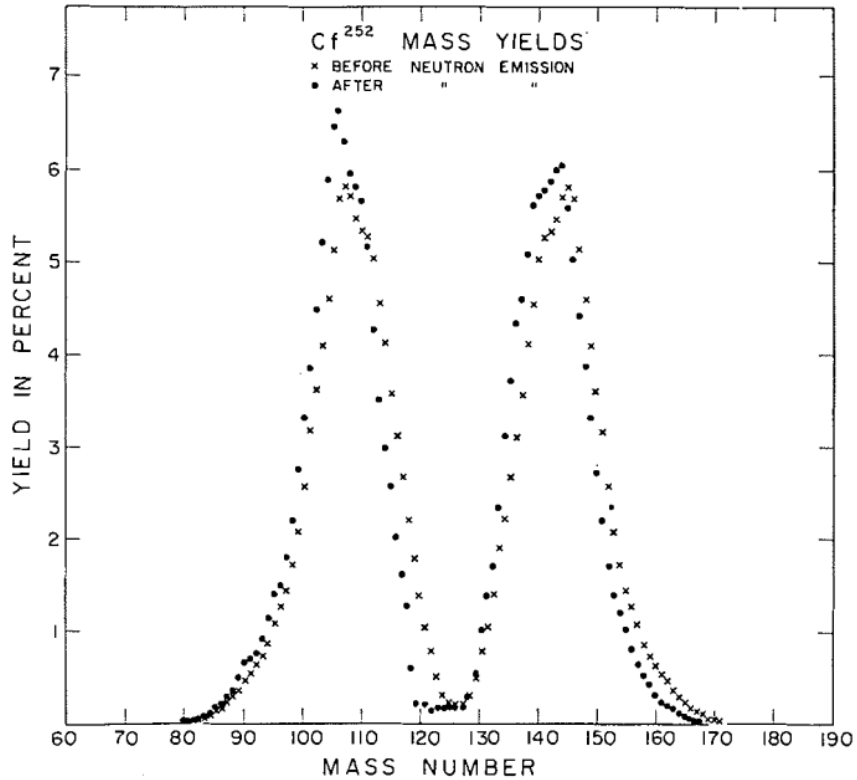
Figure 2.12: The mass distribution of ^{252}Cf fission fragments. (Figure from [46].)

^{78}Kr particle is detected the recoiling ^{208}Pb will be outside the acceptance of the particle detectors, and vice versa.

In this source test, both JANUS detectors were used in conjunction with six SeGA detectors. For logistic reasons, the full setup of 16 detectors was only used during the experiment itself. Shown in Fig. 2.13 is the lab-frame energy of detected γ rays, plotted against the relative angle with the fission fragment. As expected, emissions at low angles, traveling in the same direction as the fragment, are shifted to higher energies, while emissions at high angles, traveling in the opposite direction as the fragment, are shifted to lower energies.

The effect of the Doppler reconstruction is shown in Fig. 2.14. The resolution of the 241 keV transition from ^{110}Ru is 2% FWHM. The achieved FWHM of 2% at 241 keV
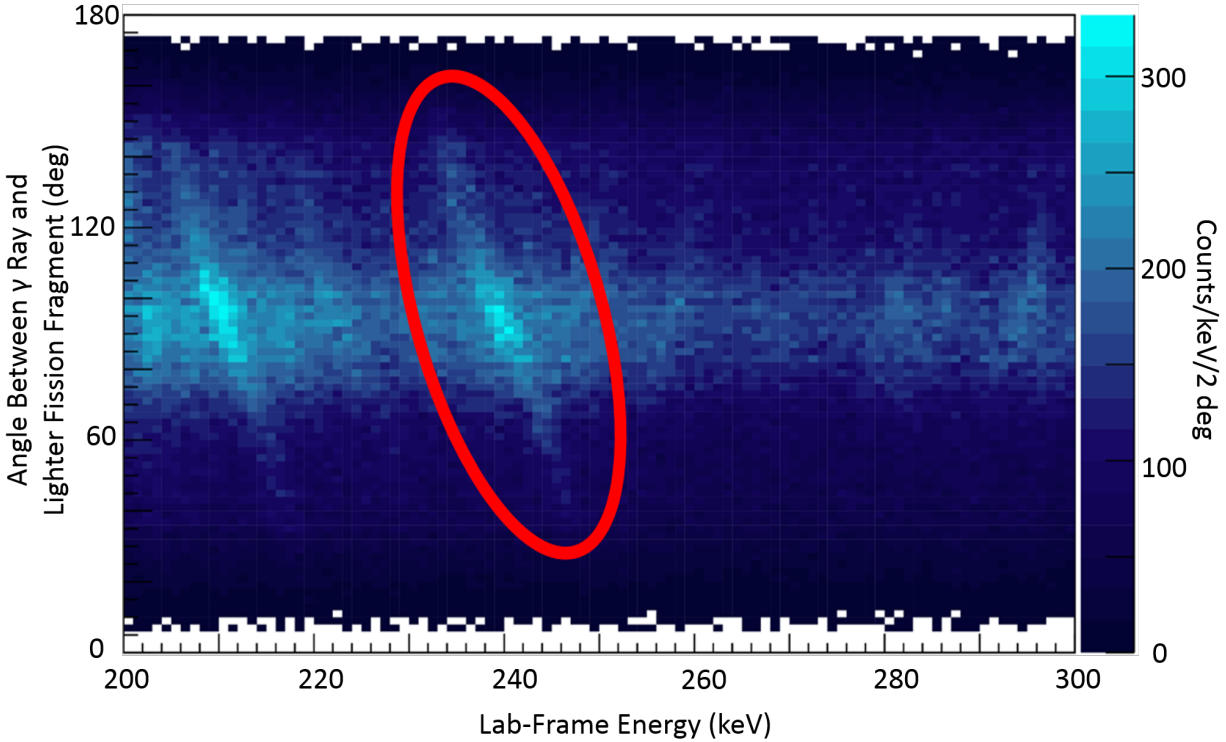
Figure 2.13: The γ-ray energies from fission fragments from ^{252}Cf plotted against the angle between the lighter fission fragment and γ ray. As an example, the 241 keV transition from ^{110}Ru, Doppler-shifted in the laboratory system, is circled in red. Also visible is the 212 keV transition from ^{100}Zr. These transitions are observed strongly, as they are near the peak of the low-mass fragment distribution, as shown in Fig. 2.12. Gamma rays emitted from the heavier fission fragments are observed as well, appearing as faint lines with orientation opposite that of the 212 keV and 241 keV transitions

was benchmarked with a provided, reconstructed ^{252}Cf source spectrum measured at ANL with the GRETINA/CHICO2 setup [30]. With GRETINA and CHICO2 having a superior angular resolution compared with the setup discussed in this thesis, the same reconstructed energy resolution was achieved, suggesting that the measured resolution of the data measured with the SeGA-JANUS setup is entirely limited by the uncertainty of v/c for the Doppler reconstruction. The successful Doppler reconstruction shows that both detectors are being read out correctly, can be time-correlated together, and that their relative positions are well-understood.
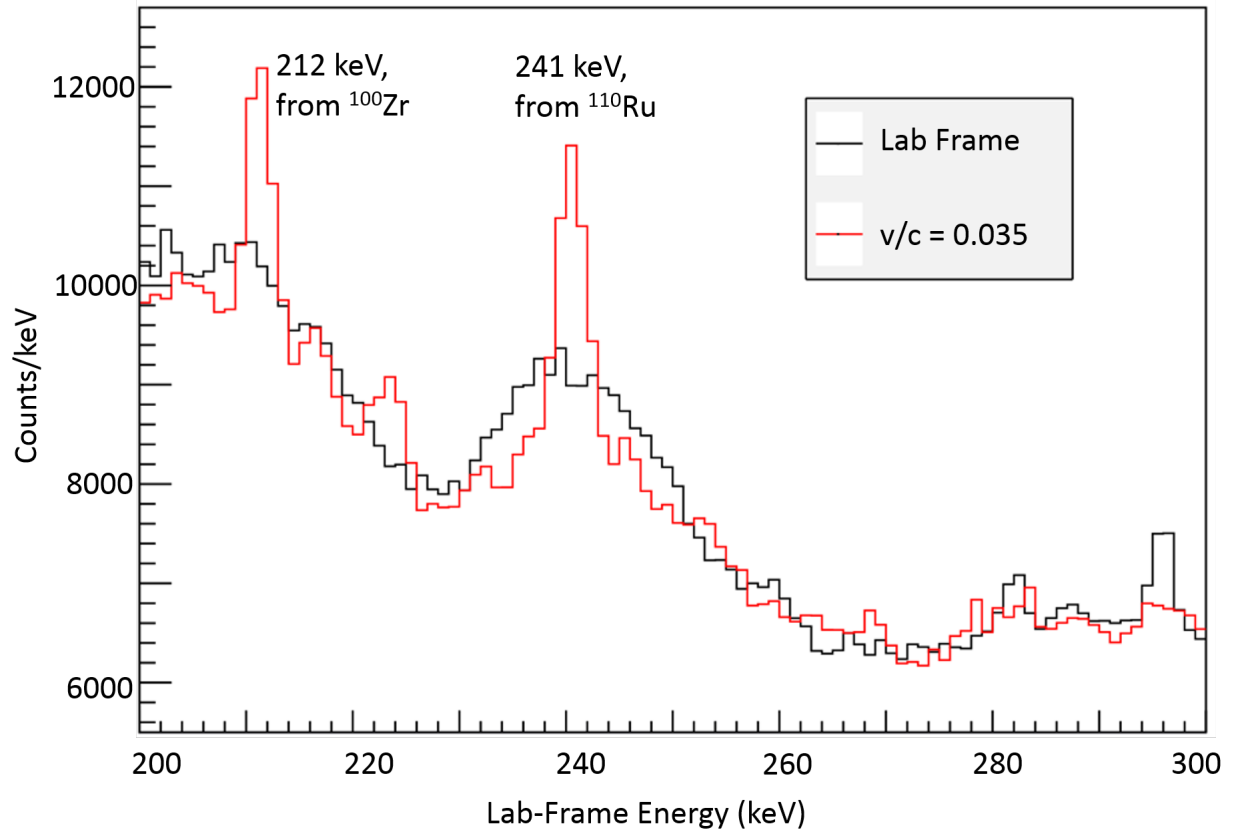
Figure 2.14: The γ-ray energy spectrum, with and without Doppler correction, for fission fragments from ^{252}Cf. The resolution of the Doppler-corrected γ energy resolution is 2% FWHM.

Chapter 3

Sub-barrier Coulomb Excitation of ^{78}Kr

3.1 Experimental Details

The experiment ran from January 27-30, 2017 at the National Superconducting Cyclotron Laboratory, located at Michigan State University, with the experimental setup arranged at the multi-purpose beamline of the ReA3 reaccelerator facility. A total of 55 hours beam on target was run in the production settings.

A beam of $3.9\,\mathrm{MeV/u}$ ^{78}Kr was impinged on a $1.09\,\mathrm{mg/cm^2}$ ^{208}Pb target. Initially, the beam rate was $1.6{\cdot}10^5$ particles per second, which was later increased to $\sim 3 \cdot 10^5$ particles per second as the experiment progressed.

16 SeGA detectors were arranged in the barrel configuration, a close-packed geometry that maximizes solid angle coverage and detection efficiency. During the run, one SeGA detector exhibited a changing energy calibration every few minutes, and was excluded from analysis. Three other detectors exhibited slow drifts in the energy calibration, which could be corrected. Two other detectors exhibited sudden jumps in calibration, which could be corrected.

During the experiment, the target frame was biased to $2\,\mathrm{kV}$ in order to prevent the
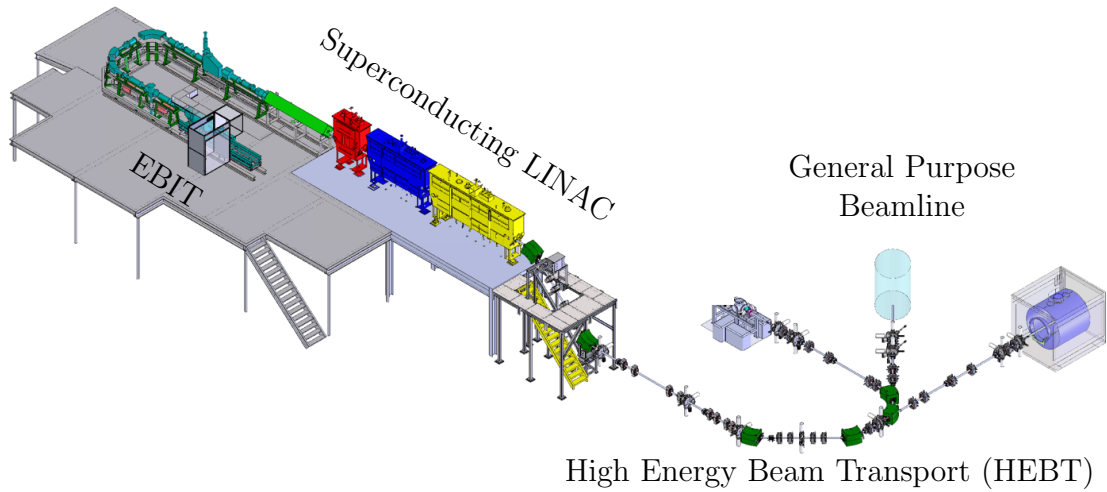
Figure 3.1: Diagram of the reaccelerator (ReA3) at NSCL.

emission of δ electrons from the target.

3.1.1 Beam Production

A beam of $3.9\,\mathrm{MeV/u}$ ^{78}Kr was produced using the reaccelerator (ReA3) [47] at the National Superconducting Cyclotron Laboratory (NSCL). Isotopically pure ^{78}Kr was bled from a gas bottle into the electron-beam ion trap (EBIT) charge breeder [48], and was ionized toward higher charge states. Ions at the 25+ charge state were selected and then accelerated to the desired energy using the ReA3 linear accelerator, and directed at the experimental station, located at the general purpose beamline. The layout of the accelerator is shown in Fig. 3.1.

The EBIT traps ions radially using the electric field of an electron beam, and axially with an applied electric field [49]. While ions are in the trap, collisions with an electron beam remove electrons from the captured ions, increasing the charge state. By removing the external field, axial confinement is removed, allowing the charged ions to escape the trap [48]. During this experiment, the ReA3 charge breeder ran at a frequency of $7\,\mathrm{Hz}$, cycling

between injection of low charge state ions and extraction of high charge state ions. During extraction, ^{78}Kr was released to the accelerator for a period of 10 ms. Outside of that period, no beam was provided to the experimental setup. A logic signal indicating when the beam is present is provided to the experimental area, and was used as part of the trigger condition of the experimental setup, reducing γ-ray events in SeGA stemming from natural background radiation, and therefore staying within the total γ-ray detection rate of the experimental setup (see Sec. 2.3).

After the ions have been released from the EBIT, the desired charge state is selected using a magnetic separation system. The ions selected are then accelerated, first with a room-temperature radio-frequency quadrupole, then a superconducting linear accelerator [33]. The ReA3 accelerator can accelerate $^{U}238$ to an energy of 3 MeV/u, or can accelerate other isotopes to higher energies, with the maximum energy depending on the Q/A of the isotope being accelerated [50].

With a beam of ^{78}Kr impacting a ^{208}Pb target, the Coulomb barrier is 4.2 MeV/u. The selected beam energy of 3.9 MeV/u is therefore sufficient to stay below the Coulomb barrier. This ensures that all excitations of the ^{78}Kr are solely due to electromagnetic interaction with the ^{208}Pb target, rather than nuclear interactions (see Sec. 1.1).

The beam was tuned using a pilot beam of ^{36}Ar. For tuning purposes, the beam current at two apertures aligned with respect to the optical beam axis were available in the setup. The aperture at the target location had a 3 mm diameter, and the other aperture 6.7 cm upstream of the target location had a 5 mm diameter. With the final tune of the pilot beam, it was found that 100% passed through the upstream aperture and 90% through the aperture at the target position, suggesting a beam spot size of approximately 3 mm.

3.1.2 Target Details

The target consisted of $1.09\,\mathrm{mg/cm^2}$ ^{208}Pb deposited onto a carbon backing of $0.05\,\mathrm{mg/cm^2}$. With $Z = 82$, using a ^{208}Pb takes advantage of the increased Coulomb field at high values of Z [20]. In addition, as ^{208}Pb has closed proton and neutron shells, it has reduced $B(\mathrm{E2})$ transition strengths, as discussed in Sec. 1.1. This simplifies the analysis as the γ-ray spectrum only contains events from projectile excitations.

The thickness of the deposited ^{208}Pb was determined by measuring the energy loss of α particles passing through the target. The α particles were produced from a collimated source containing ^{244}Cm, ^{241}Am, and ^{239}Pu, which primarily emits α particles of $5.805\,\mathrm{MeV}$, $5.486\,\mathrm{MeV}$, and $5.157\,\mathrm{MeV}$, respectively. The result of the energy loss measurement is shown in Fig. 3.2.

The thickness was determined by using SRIM [40], varying the thickness of the ^{208}Pb until the energy loss matched the energy loss observed, assuming the nominal thickness of $0.05\,\mathrm{mg/cm^2}$ for the carbon backing layer. When measuring without the target in place, the three energies of the α particles provided the energy calibration.

The measurement was repeated at multiple locations of the target, to determine the variability of the target thickness. Different areas had very similar energy loss, corresponding to an inhomogeneity in target thickness of $\sim 1\%$.
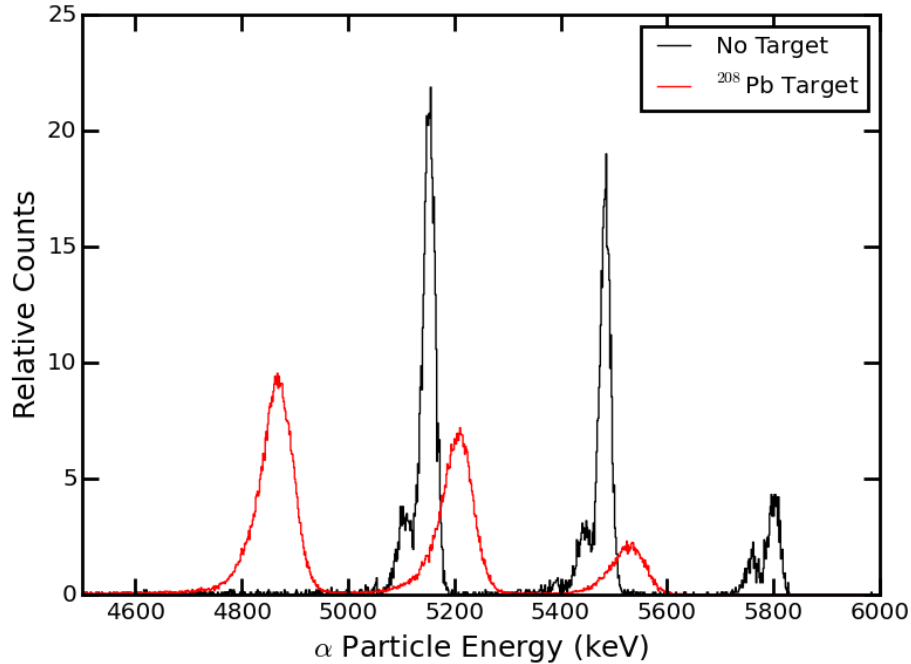
Figure 3.2: In black, the energy spectrum of a radioactive source containing the α emitters ^{244}Cm, ^{241}Am, and ^{239}Pu. In red, the energy spectrum of the same source, with the ^{208}Pb target put between source and detector. The target thickness is deduced from the observed energy loss through the target. In addition to energy loss, the spectrum also becomes wider due to energy straggling through the target [39].

3.2   Data Analysis

3.2.1   Particle Identification and ^{78}Kr Reconstruction

By conservation of momentum, when a beam particle is scattered off of a target nucleus, there is some momentum imparted to the target nucleus. If the recoiling target nucleus hits a silicon detector, it can be detected. It is therefore necessary to distinguish between events caused by scattered ^{78}Kr and events caused by recoiling ^{208}Pb.

The expected energy of the scattered ^{78}Kr and the recoiling ^{208}Pb are shown in Fig. 3.3, based on an assumption of elastic scattering in relativistic kinematics. The angles of the scattered projectile and recoiling target nucleus are shown in Fig. 3.4. As the total kinetic
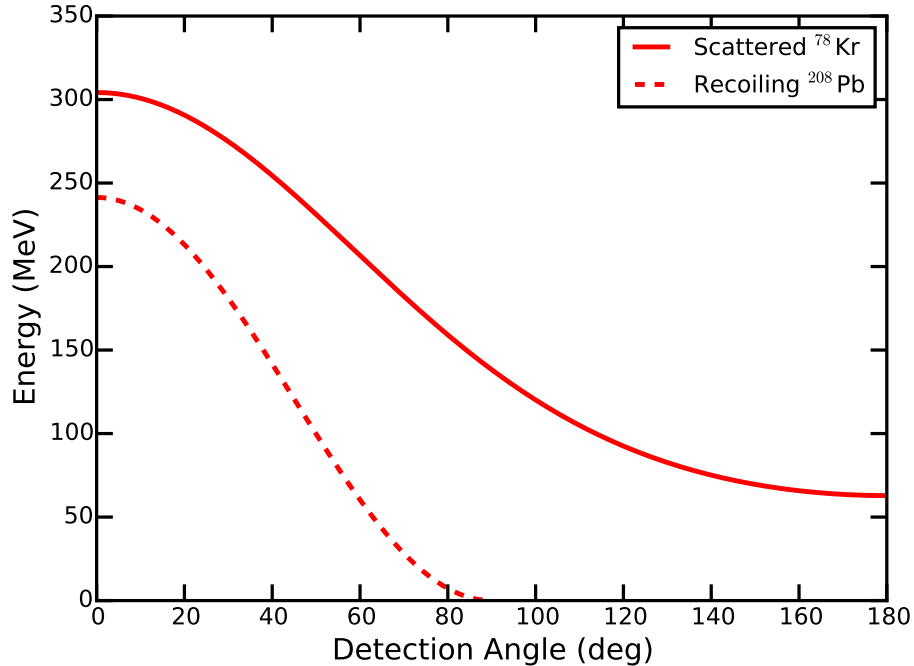
Figure 3.3: The expected energies of scattered ^{78}Kr and recoiling ^{208}Pb, across the full angular range, based on $3.9\,\mathrm{MeV/u}$ incoming beam energy. This calculation assumes that the two particles scatter elastically. As the nuclear excitations are at maximum a few MeV, as compared against the $\sim 300\,\mathrm{MeV}$ beam energy, this is a reasonable assumption.

energy transferred to internal degrees of freedom is on the order of a few MeV, while the beam energy is over $300\,\mathrm{MeV}$, elastic scattering is a valid approximation. Relativistic kinematics were used for availability of existing implementations. At projectile velocities of $v/c < 0.1$, the errors introduced by using classical kinematics are less than the sensitivity of the detectors. The recoiling ^{208}Pb can only scatter at angles less than $90°$ in the lab frame. In the upstream detector, at angles greater than $90°$, no particle identification is necessary to discriminate between recoiling ^{208}Pb and scattered ^{78}Kr. However, in the downstream JANUS detector, located at lower scattering angles, both particles are present, and must be separated. The experimental energies are shown in Fig. 3.5, with the two nuclei being clearly distinguishable.

Using relativistic kinematics, the relationships between center of mass scattering angles,
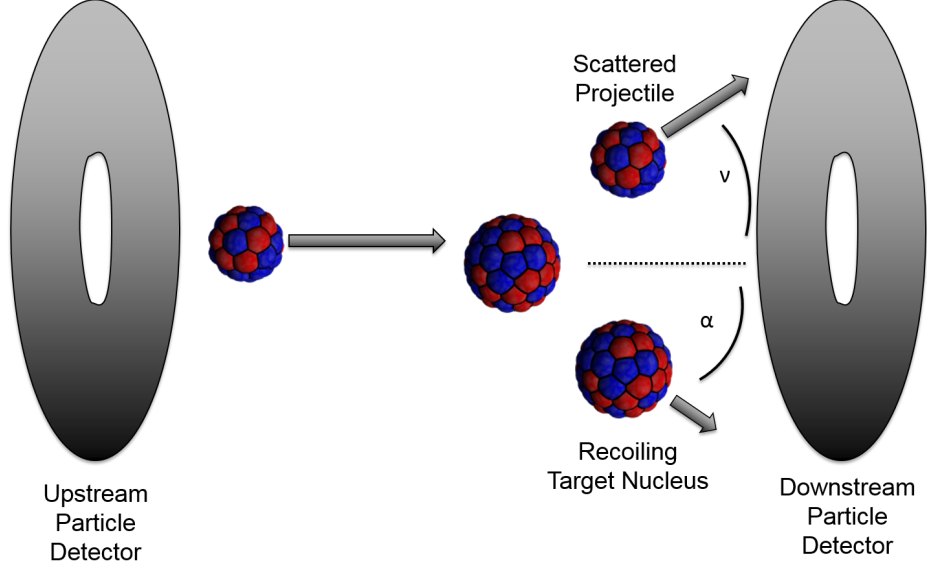
Figure 3.4: The angles of the scattered projectile and recoiling target nucleus, along with relative positions of the two particle detectors.

lab frame scattering angles, and kinetic energies are as follows, where Θ is the scattering angle of the projectile in the center-of-mass frame of reference, ν is the scattering angle of the projectile in the laboratory frame of reference, α is the angle of the recoiling target nucleus, relative to the incoming projectile's trajectory, in the laboratory frame of reference, $\gamma = \frac{1}{\sqrt{1-v^2/c^2}}$ is the Lorentz factor of the center-of-mass frame, relative to the lab frame, m_p and m_t are the rest masses of the projectile and target, respectively, $M = m_p + m_t$ is the total rest mass of the system, $\rho = m_p/m_t$ is the mass ratio, $\varepsilon_p = \frac{T_p}{m_p c^2}$ is the kinetic energy of the projectile in terms of the rest mass of the projectile, and T_p, T_s, and T_r are the kinetic energy of the incoming projectile, scattered projectile, and recoiling target nucleus,
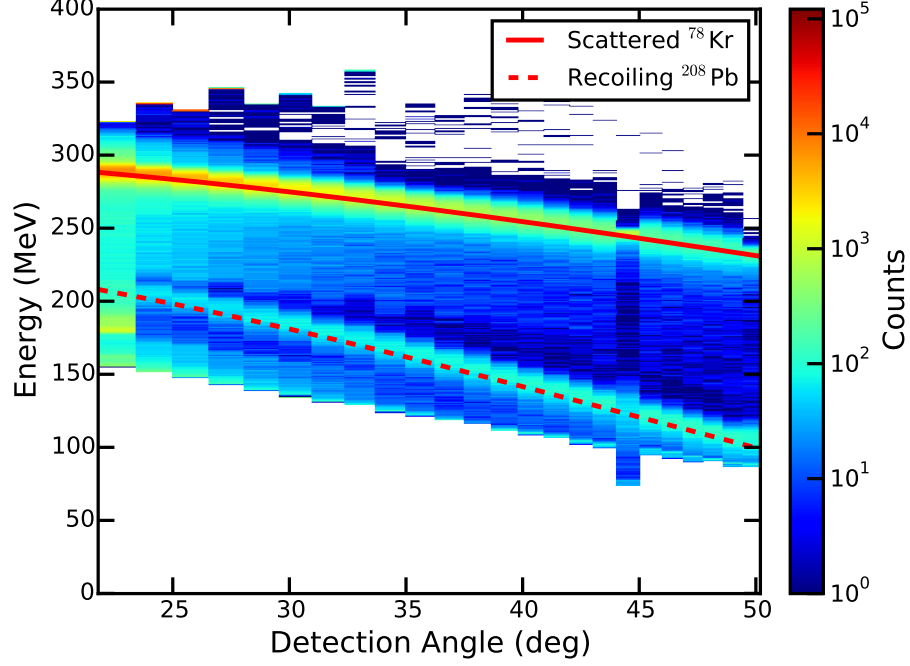
Figure 3.5: Particle identification of scattered ^{78}Kr and recoiling ^{208}Pb in the forward detector of JANUS. Kinematic lines for each particle show the energy when scattering at a given angle. The clear separation between the energies of the two isotopes allows for clear discrimination in analysis. Due to electronics issues, the segment covering scattering angles 44-45° has poorer resolution, but is still sufficient to discriminate between ^{78}Kr and ^{208}Pb.

respectively [51]:

$$\tan \nu = \frac{\sin \Theta}{\gamma(\cos \Theta + \rho g)} \tag{3.1}$$

$$\tan \alpha = \frac{\sin \Theta}{\gamma(1 - \cos \Theta)} \tag{3.2}$$

$$\gamma = \frac{T_p + Mc^2}{Mc^2} \tag{3.3}$$

$$g = \frac{1 + \rho(1 + \varepsilon_p)}{(1 + \varepsilon_p) + \rho} \tag{3.4}$$

$$\frac{T_s}{T_p} = 1 - \frac{2\rho(1 - \varepsilon_p/2)}{(1 + \rho)^2 + 2\rho\varepsilon_p}(1 - \cos \Theta) \tag{3.5}$$

$$T_r = T_p - T_s. \tag{3.6}$$

The upstream detector does have some events occurring at energies higher than those allowed by kinematics. These events are in coincidence with ^{78}Kr γ rays emitted in the laboratory frame without Doppler shift. These events can therefore be understood as ^{78}Kr particles that scattered off an upstream beam element, as for example the 5 mm aperture, and that were then excited while stopping in the JANUS detector. These only compose less than 1 part in one thousand of the total data, and can be easily removed.

A measurement of the recoiling ^{208}Pb still contains useful information due to the two-body kinematics. Even though the ^{78}Kr is not detected, it may still be left in an excited state, producing γ rays that can be observed in SeGA. The observed scattering angle of the detected ^{208}Pb along with an assumed interaction location at the center of the target is sufficient to reconstruct the scattering angle of the excited ^{78}Kr, using Eq. 3.1 and Eq. 3.2, as shown in Fig. 3.6. The angle between the reconstructed ^{78}Kr angle and the emitted γ ray can then be used to Doppler-correct the measured γ-ray energy, as described in Sec. 3.2.3.

As a result of using the reconstructed ^{78}Kr trajectories, the effective solid angle of JANUS is greatly increased. While the physical extent of JANUS covers angles only at 20-49° and at 131-160°, the reconstructed trajectories cover angles at 62-121°. The relationship between the scattering angle of ^{78}Kr with the recoil angle of ^{208}Pb in the laboratory system is plotted in Fig. 3.6, and allows inference of the angle for ^{78}Kr from ^{208}Pb events.

3.2.2   Gamma-Particle Coincidences

In order to remove room background γ-ray events from the analysis, only γ rays that occurred in coincidence with a particle in the silicon detectors are considered. The gate being used is reproduced in Fig. 3.7, which shows the γ-ray energy plotted against the time difference between the γ-ray detection and the particle detection. Particle-γ coincidences are seen as
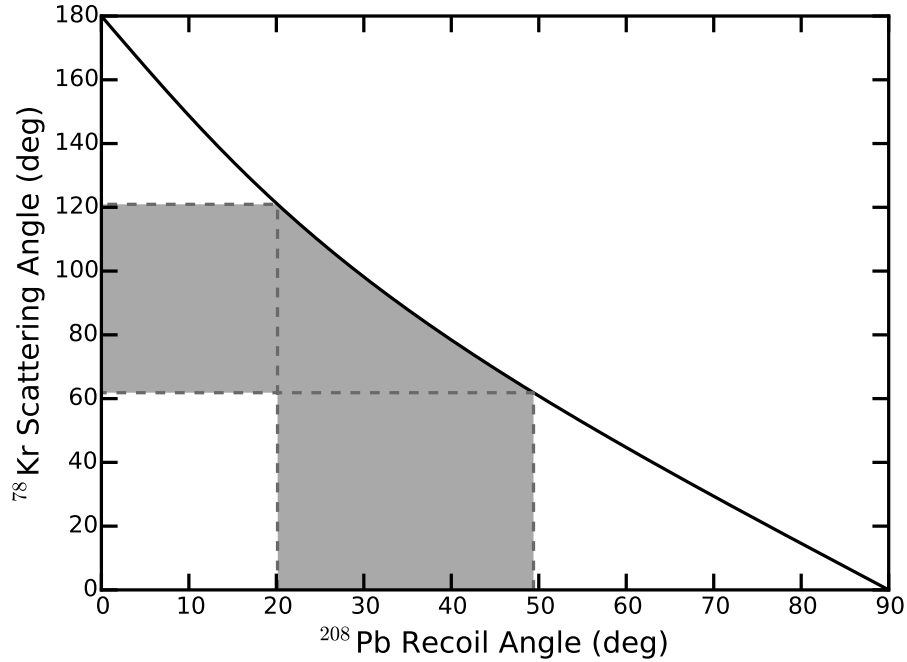
Figure 3.6: Reconstruction of the scattered ^{78}Kr given the angle of the recoiling ^{208}Pb. The gray region indicates the angular acceptance for recoiling ^{208}Pb, and the corresponding angles of the reconstructed ^{78}Kr.

the vertical line in the spectrum. At low γ-ray energies, the time difference changes, due to walk in the γ-ray trigger. Therefore, a two-dimensional gate is used to identify prompt γ-ray emission, with the gate being based both on relative time and γ-ray energy.

Room background γ rays can be observed in Fig. 3.7 as horizontal lines. The $1460\,\mathrm{keV}$ peak from the decay of ^{40}K and the $2614\,\mathrm{keV}$ peak from the decay of ^{208}Tl into ^{208}Pb are clearly visible. These backgrounds are effectively removed with the gate. As there is no significant intensity near the $2614\,\mathrm{keV}$ region after the gate has been applied, it is verified that occurrences of target excitations are minimal.
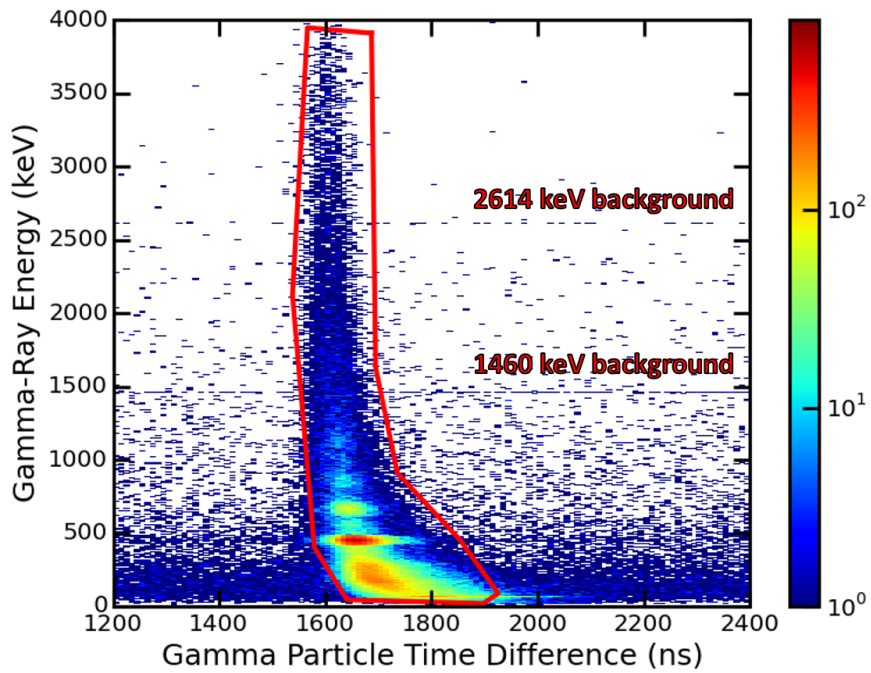
Figure 3.7: The correlation between lab-frame γ-ray energy on the y-axis and the time difference between γ-ray detection and particle detection on the x-axis. The time-energy gate for determining coincidence between particles and γ rays is shown in red. The 1460 keV and 2614 keV room background peaks from the decay of ^{40}K and ^{208}Tl.

3.2.3　Doppler Correction

Photons emitted from a moving source will be Doppler-shifted according to the relative velocity between the source and the observer (see Sec. 2.2.2). As the incoming beam has a velocity on the order of $v/c \approx 10\%$, the measured γ-ray energy in the laboratory frame of reference will be Doppler-shifted relative to the emitted γ-ray energy in the rest frame of the ^{78}Kr. This is described in more detail in Sec. 2.2.1.

The relationship between observed γ-ray energy and emission angle obtained from the particle and γ-ray detection is shown in Fig. 3.8. Gamma rays emitted at angles less than $90°$ are shifted to higher energies and γ rays emitted at angles greater than $90°$ are shifted to lower energies, while γ rays emitted at about $90°$ are unshifted. The effect of the Doppler reconstruction is shown in Fig. 3.10. The resulting Doppler-reconstructed peak has a FWHM of 1.6%. This is better than the resolution obtained using the ^{252}Cf source as described in Sec. 2.4, proving that the resolution in the ^{252}Cf is indeed limited by the velocity uncertainty. For the in-beam data, the limitation in the achievable γ-ray energy resolution is given primarily by the angular resolution of SeGA.

For ^{78}Kr events reconstructed from the measured trajectory of recoiling ^{208}Pb, the ^{78}Kr may have scattered at angles close to $90°$. In these cases, the ^{78}Kr travels a longer distance before leaving the target, losing large amounts of kinetic energy to the target. This results in γ-ray emission at lower velocities, with smaller shifts due to the Doppler effect. This can be seen in Fig. 3.9, which shows the relationship between γ-ray emission angle and lab-frame γ-ray energy for reconstructed ^{78}Kr events. Gamma rays emitted in flight produce a Doppler-shifted energy curve, similar to that in Fig. 3.8, while γ rays emitted at rest form a vertical distribution along the $455\,\mathrm{keV}$ γ-ray energy without a dependence on the measured
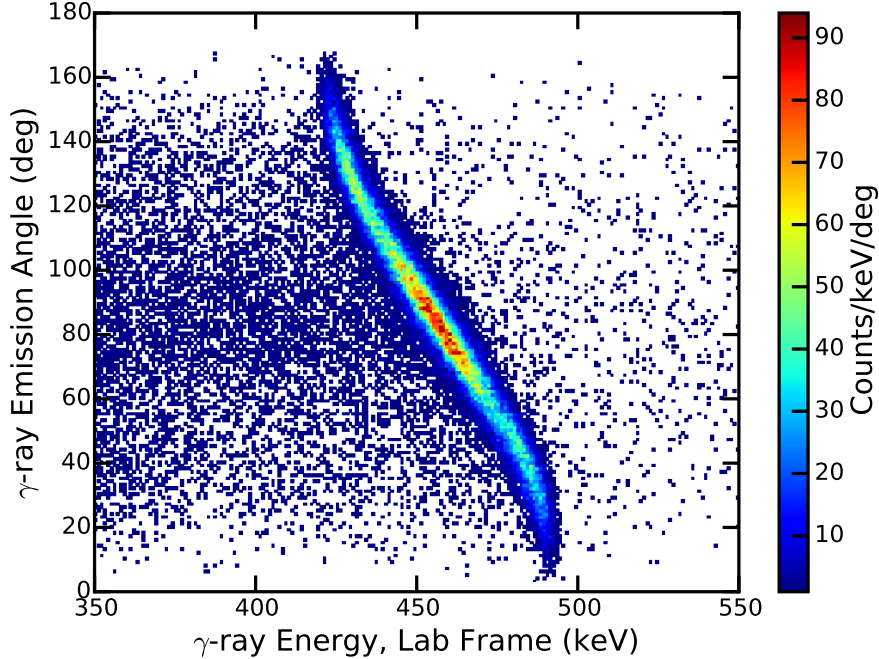
Figure 3.8: The lab-frame γ-ray energy plotted against γ-ray emission angle, for ^{78}Kr detected in the downstream JANUS detector. This spectrum only shows the dominant 455 keV transition in ^{78}Kr.

emission angle. This effect contributes to worse γ-ray energy resolution for reconstructed ^{78}Kr events.

In Coulomb excitation, a significant fraction of the beam's original kinetic energy can be imparted onto the target nucleus. The greater the projectile scattering angle, the more energy has been transferred to the target nucleus. By conservation of energy and momentum in the two-body kinematics, the velocity of the outgoing beam particle can be determined by the scattering angle of the outgoing beam, using Eq. 3.1 and Eq. 3.5, as shown in Fig. 3.11.

In order to account for the angle-dependent value of v/c, the ^{78}Kr events were split into 3 regions of scattering angle coverage, consisting of the downstream detector, the upstream detector, and the ^{78}Kr events reconstructed from measured ^{208}Pb (see Sec. 3.2.1). In each region, the value of v/c used to perform the Doppler reconstruction was varied to minimize
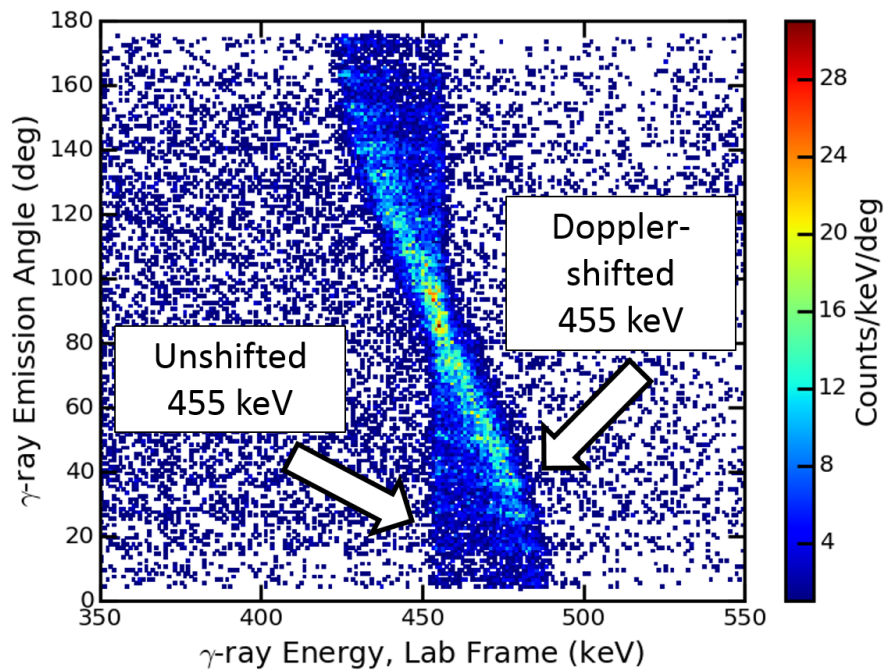
Figure 3.9: The lab-frame γ-ray energy plotted against γ-ray emission angle, for ^{78}Kr events reconstructed from the measured trajectory of recoiling ^{208}Pb. This spectrum only shows the dominant 455 keV transition in ^{78}Kr. Different from Fig. 3.8, an unshifted component of the 455 keV γ-ray energy is visible in addition to the Doppler-shifted component, caused by ^{78}Kr stopped in the target.
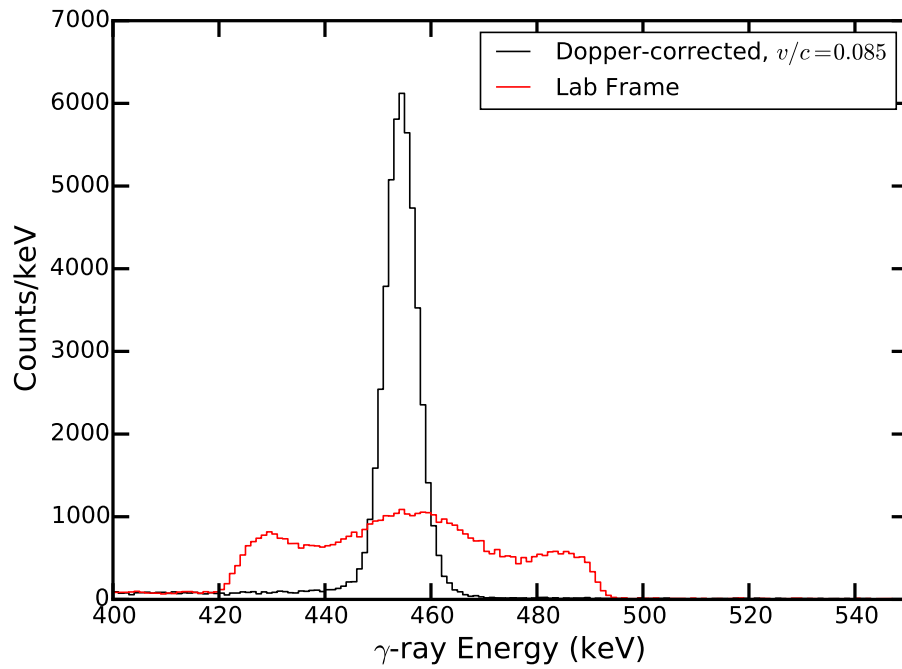
Figure 3.10: The lab-frame energy spectrum, compared against the Doppler-reconstructed energy spectrum, for ^{78}Kr detected in the downstream JANUS detector, using $v/c = 0.085$ in the Doppler reconstruction. This spectrum only shows the dominant 455 keV transition in ^{78}Kr.
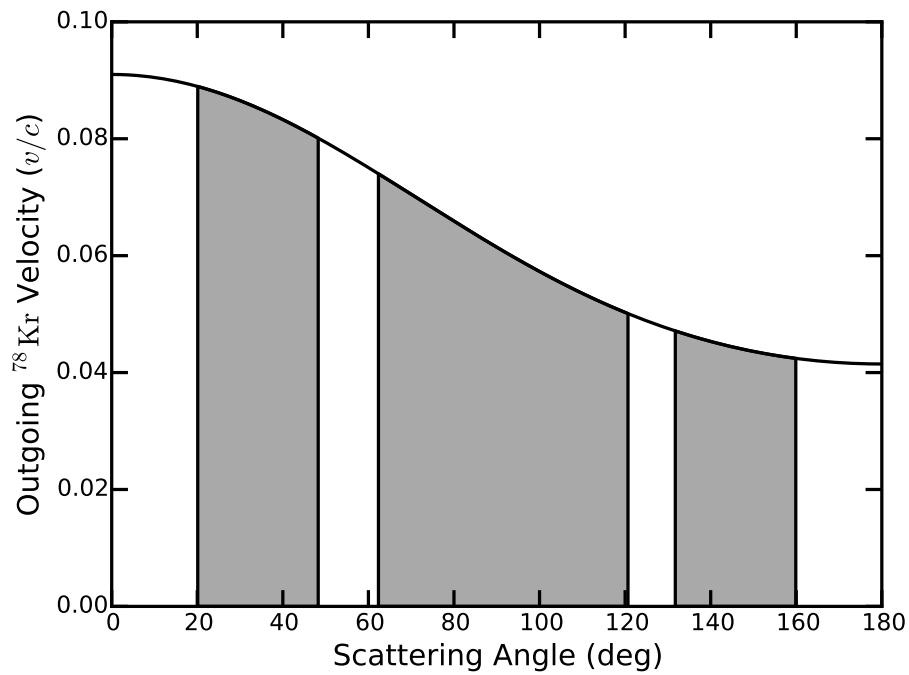
Figure 3.11: The velocity of the scattered ^{78}Kr as a function of scattering angle. The three ranges of scattering angles of ^{78}Kr deduced from the silicon detector coverage are indicated. The variation of v/c within a region is sufficiently small for using a fixed Doppler-reconstruction v/c for each range.

the width of the 455 keV peak in ^{78}Kr. The resulting values of v/c were consistent with those predicted by kinematics for each scattering angle region. The final Doppler-corrected γ-ray spectra are shown in Fig. 3.12. The region from 500 keV to 1000 keV is shown in greater detail in Fig. 3.13, and the region from 1000 keV to 2000 keV is shown in greater detail in Fig. 3.14.

3.2.4 Experimental Yields

The measured γ-ray yields are extracted from the number of counts in the corresponding peak in the γ-ray spectrum, corrected for the detection efficiency of the SeGA array. The energy-dependent detection efficiency was measured using a ^{152}Eu source of known intensity, then interpolated to the energies of the observed ^{78}Kr γ rays. The measured efficiencies and the fit used for interpolation are shown in Fig. 3.15.

The measured yields must be combined into scattering angle ranges. Each region of scattering angle corresponds to a different momentum transfer between the beam and target nuclei. The four angle regions used in this analysis were the inner 12 rings of the downstream detector, covering angles 20-37°, the outer 12 rings of the downstream detector, covering angles 37-49°, the reconstructed ^{78}Kr fragments, covering angles 62-121°, and the upstream detector, covering angles 131-160°. These regions were selected to maximize angular granularity, while still ensuring that low-intensity peaks had a sufficient number of counts for extracting peak intensities.

For the reconstructed ^{78}Kr, the presence of the γ rays emitted at rest, described in Sec. 3.2.3 must be accounted for. These γ rays form a broad component on the sides of each peak in the Doppler-shifted γ-ray energy spectrum, as can be seen for the high statistics 455 keV peak in Fig. 3.12. In peaks with fewer counts, the broad component cannot be
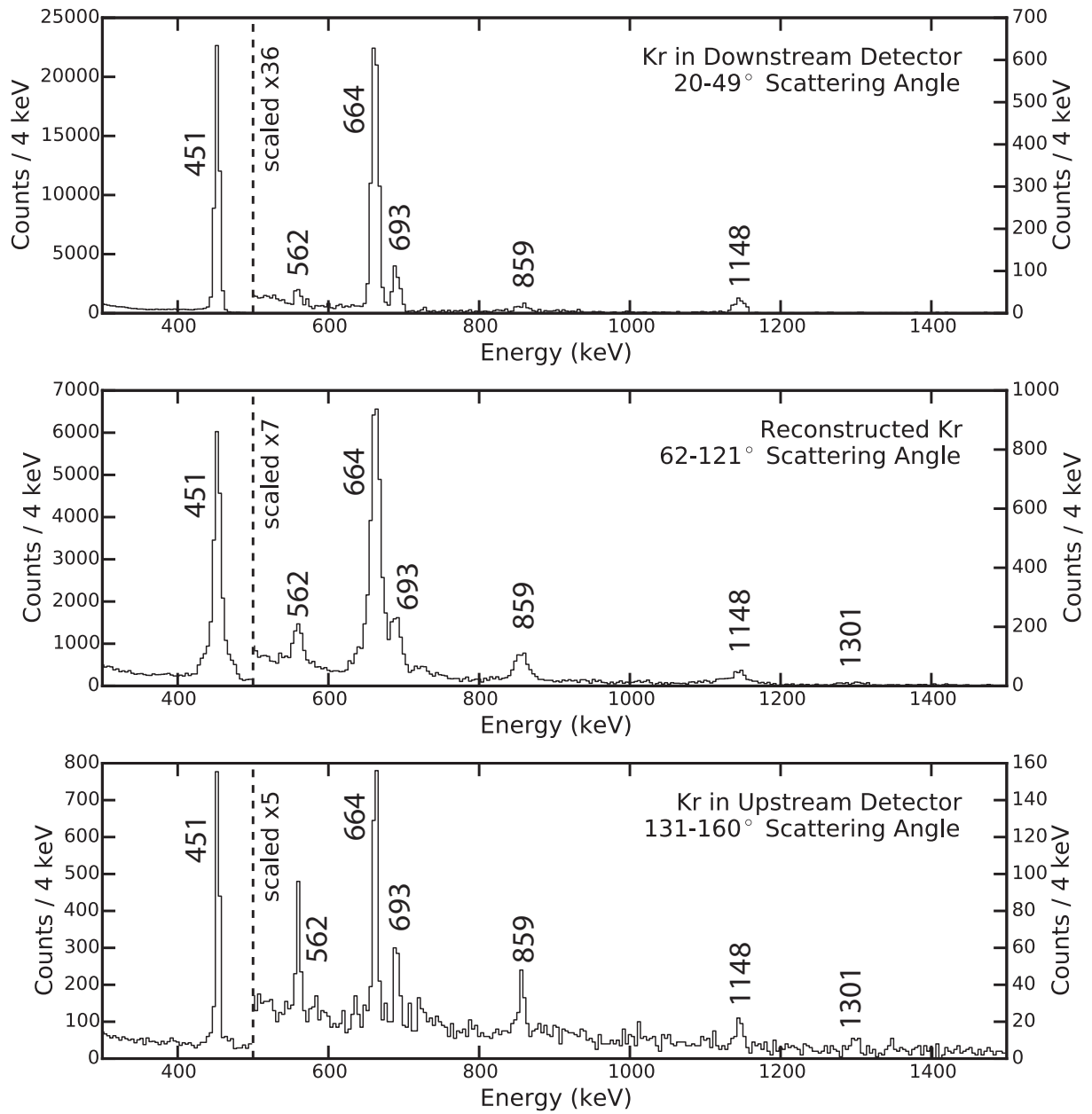
Figure 3.12: The Doppler-corrected energy spectrum for each angular region of the scattering ^{78}Kr. For performing Doppler correction, $v/c = 0.085$ was used for the downstream detector, $v/c = 0.06$ for the reconstructed fragments, and $v/c = 0.04$ for the upstream detector.
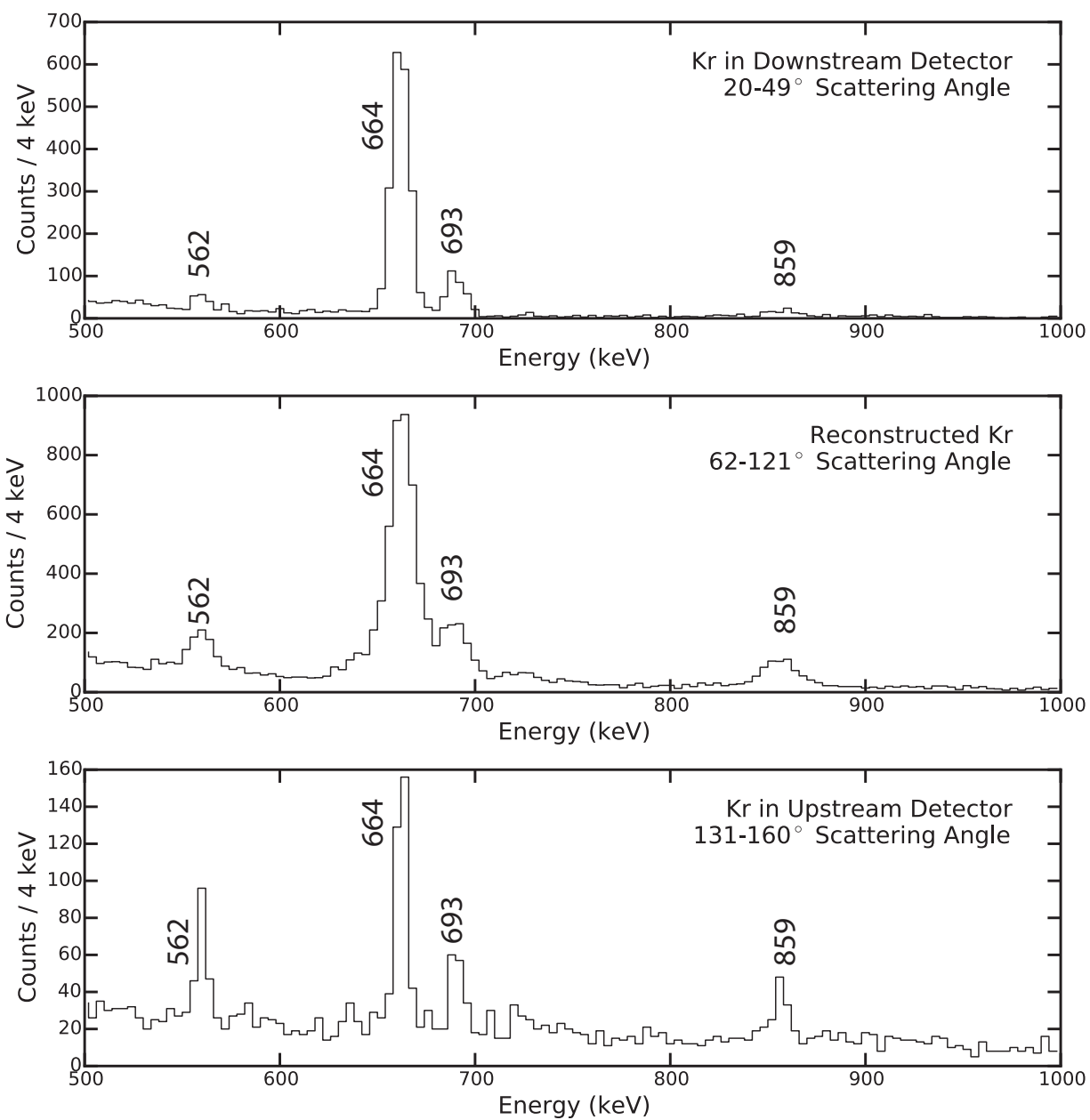
Figure 3.13: The Doppler-corrected energy spectrum for each angular region of the scattering ^{78}Kr, showing the energy region from 500 keV to 1000 keV. For performing Doppler correction, $v/c = 0.085$ was used for the downstream detector, $v/c = 0.06$ for the reconstructed fragments, and $v/c = 0.04$ for the upstream detector.
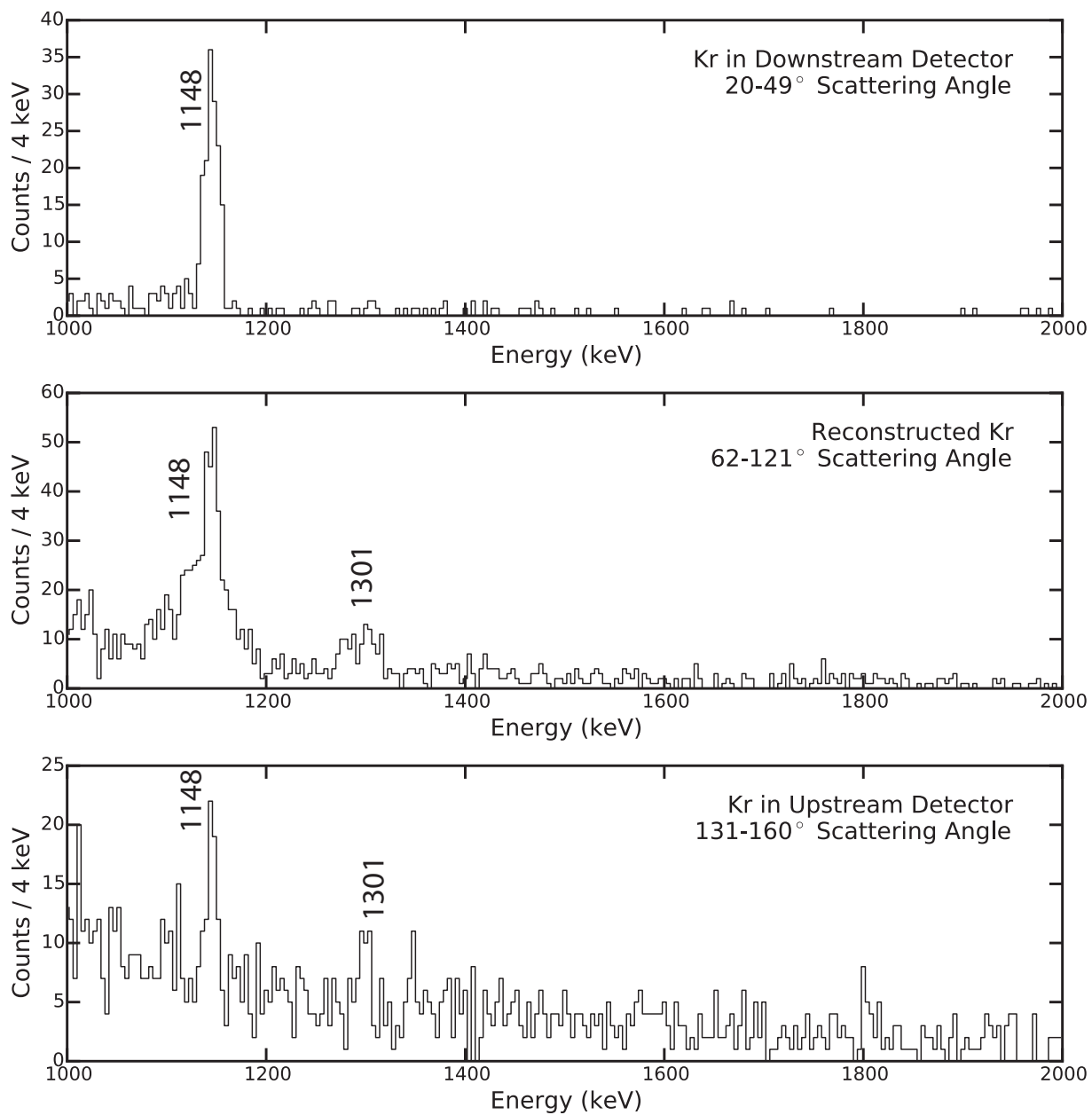
Figure 3.14: The Doppler-corrected energy spectrum for each angular region of the scattering ^{78}Kr, showing the energy region from $1000\,\mathrm{keV}$ to $2000\,\mathrm{keV}$. For performing Doppler correction, $v/c = 0.085$ was used for the downstream detector, $v/c = 0.06$ for the reconstructed fragments, and $v/c = 0.04$ for the upstream detector.
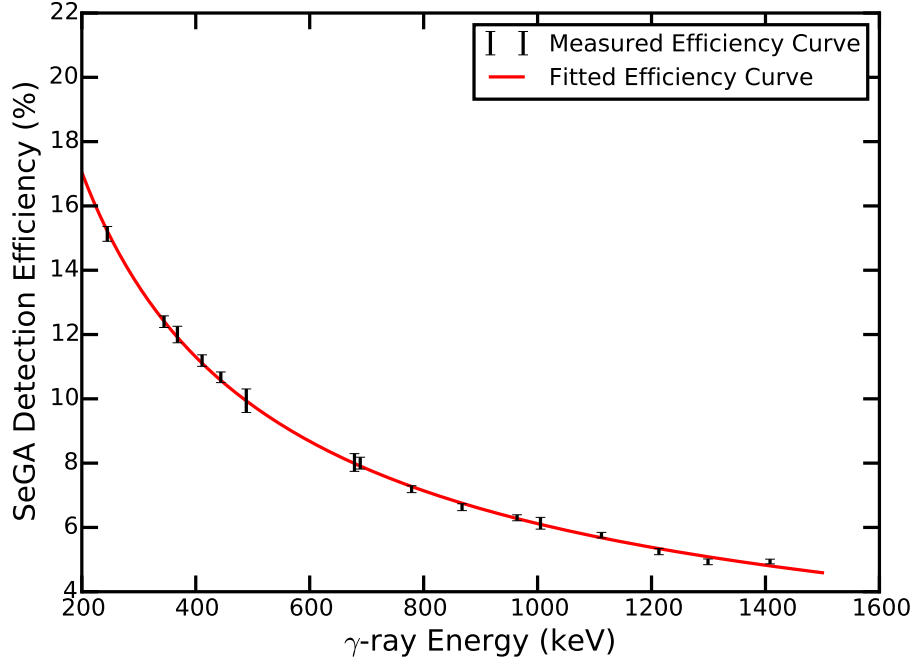
Figure 3.15: Measured SeGA efficiency curve using a ^{152}Eu source. The red line shows a fit to the measured efficiencies, with functional form $1157 \exp(-0.7511 \log(E + 74.6))$, where E is the energy in keV, and the resulting value is in percent.

easily identified. Therefore, to account for the full peak intensity including both in-flight and at-rest γ-ray emission, a narrow integration region is used around each peak, and the resulting integral is scaled by the proportion of total peak area to narrow peak area, as determined from the $455 \, \mathrm{keV}$ peak.

The $1148 \, \mathrm{keV}$ peak in the reconstructed ^{78}Kr presents additional difficulties, as the choice of background region has a very strong influence on the extracted peak area. Here, the known branching ratio of $\frac{2_2^+ \rightarrow 2_1^+}{2_2^+ \rightarrow 0_1^+} = 0.624(12)$ [52] was used to inform the choice of background regions to reproduce the known value.

The measured γ-ray peak areas for all scattering angle region are shown in Table 3.1. Transitions not observed in a given scattering angle region are left blank. When determining the experimental yield for each transition, a 3% systematic uncertainty was included.

| Transition | Energy (keV) | Scattering Angle Region |
		20-37°	37-49°	62-121°	131-160°
$2_1^+ \to 0_1^+$	455	28510(170)	17826(136)	21146(154)	1344(40)
$0_2^+ \to 2_1^+$	562		55(11)	541(64)	106(14)
$4_1^+ \to 2_1^+$	664	686(27)	1227(36)	4125(90)	292(20)
$2_2^+ \to 2_1^+$	693	124(12)	171(14)	935(60)	100(15)
$6_1^+ \to 4_1^+$	859	31(7)	43(10)	550(63)	100(17)
$2_2^+ \to 0_1^+$	1148	57(8)	92(10)	410(30)	39(12)
$2_3^+ \to 2_1^+$	1301			80(15)	17(9)

Table 3.1: The experimental peak areas for each scattering angle region. Transitions not observed in a given scattering angle region are left blank.

3.3 Matrix Element Extraction

In low-energy Coulomb excitation, multi-step excitations can occur, and so the population of an excited state may result from direct excitation, excitation through an intermediate state, or feeding from higher-lying states. In order to extract all transition matrix elements, the coupled-channel Coulomb excitation analysis code GOSIA [38] was used, a high-level description of which is present in the Introduction of this work.

GOSIA takes as input the measured γ-ray yields, the angular coverage of particle and γ-ray detectors, the spins, parities, and energies of the nuclear energy levels, transition and diagonal matrix elements to be varied, incoming beam energy and energy loss through the target, and internal conversion coefficients. The exact form of the inputs provided to GOSIA and their interpretation are described more fully in App. B. GOSIA performs a χ^2 minimization, varying the matrix elements of the nucleus being studied, in order to reproduce the measured yields. In addition, values for lifetimes, multipole mixing ratios, branching ratios, and matrix elements can be added as additional data points, contributing to the χ^2 value. GOSIA allows the absolute normalization of experimental yields to vary, accounting for absolute detector efficiency, target thickness, and integrated beam on target.

The level scheme supplied to the GOSIA input is shown in Fig. 3.16. Levels and transitions beyond those observed are included in the calculation as buffer states [36], described in Ch. 4. As no experimental yields are present for these transitions, the predicted yields of these transitions do not contribute to the total χ^2. Should the matrix elements extracted predict a yield for these unobserved transitions that is above a user-defined threshold, GOSIA will issue a warning, indicating that either the calculation should be rerun, or the data should be re-examined for the transition. For all transitions included in the fit, E2 matrix elements are included. In transitions with $\Delta J \leq 1$, M1 matrix elements are also included. As only positive parity states are observed in the measurement, E1 and E3 matrix elements are not relevant.

For the initial fit parameters, estimations of matrix elements were made assuming an asymmetric rigid rotor model [53], which predicts the relative values of transition and diagonal matrix elements within a deformed nucleus. The asymmetry parameter γ of the rigid rotor determines both the energy levels and matrix elements of the nucleus being described. The γ deformation parameter was chosen as $22.5°$, because at that value, the asymmetric rigid rotor model predicts that the energies of the 4_1^+ and 2_2^+ states will be nearly equal [53], as is the case in ^{78}Kr. The absolute value of initial parameters was determined by scaling these relative values from the asymmetric rigid rotor model to match a previous measurement of the E2 matrix element of the $2_1^+ \to 0_1^+$ transition.

During initial fits, while determining the minimum number of degrees of freedom necessary to describe the data, most matrix elements were constrained to stay at the same value relative to the $2_1^+ \to 0_1^+$ transition. As ^{78}Kr is not very well-described by either an asymmetric rigid rotor or a vibrator [54], it was necessary to relax these constraints as the fit settled into a local minimum. In order to avoid having many ill-constrained matrix elements,
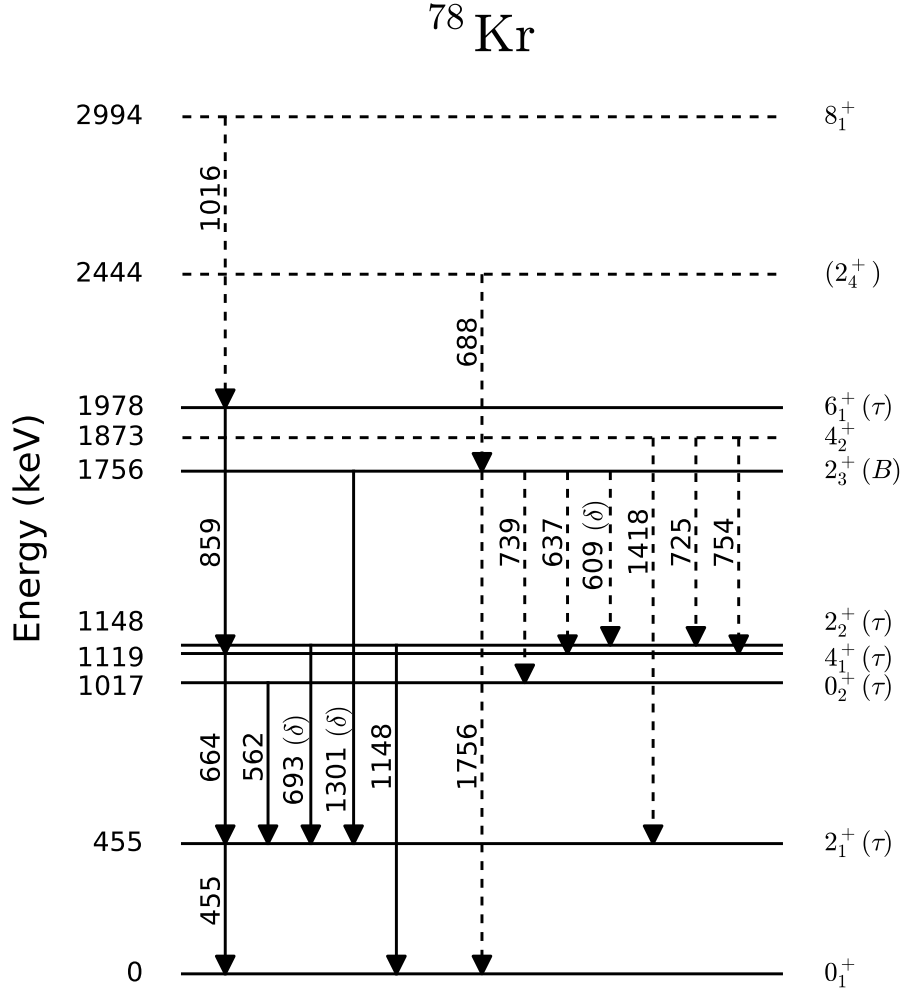
Figure 3.16: The level scheme of ^{78}Kr, as used for fitting matrix elements to the observed data, with indications to show the use of literature values, contributing to the χ^2 value. Levels and transitions in solid lines were directly observed in this experiment. Levels and transitions in dashed lines are included in the coupled channels calculation, but do not have experimental yields contributing to the χ^2 calculation. States marked with a τ had their lifetimes used as components of the χ^2. States marked with a B had branching ratios between all de-excitation γ rays used as components of the χ^2. Transitions marked with a δ had their E2/M1 mixing ratio used as a component of the χ^2.

Level	Mean Lifetime [ps]
2^+_1	31.2(10)
0^+_2	13.0(36)
4^+_1	3.63(17)
2^+_2	4.8(9)
6^+_1	0.94(10)

Table 3.2: The lifetimes used as data points in the GOSIA χ^2 minimization [52].

Transitions	Branching ratio
$2^+_3 \to 0^+_1 / 2^+_3 \to 2^+_1$	0.254(8)
$2^+_3 \to 0^+_2 / 2^+_3 \to 2^+_1$	0.518(8)
$2^+_3 \to 4^+_1 / 2^+_3 \to 2^+_1$	0.119(4)
$2^+_3 \to 2^+_2 / 2^+_3 \to 2^+_1$	0.047(10)

Table 3.3: The branching ratios used as data points in the GOSIA χ^2 minimization [52].

additional data from previous measurements were included in the χ^2 fit. Additional values used for the lifetimes, branching ratios, and mixing ratios are listed in Tables 3.2, 3.3, and 3.4, respectively, and were taken from NNDC [52]. In addition, higher-lying matrix elements from [55] shown in Table 3.5, where these are ill-constrained from experimental yields in the current work.

Transition	E2/M1 mixing ratio
$2^+_2 \to 2^+_1$	0.45(10)
$2^+_3 \to 2^+_2$	4.0(35)
$2^+_3 \to 2^+_1$	-1.32(55)

Table 3.4: The mixing ratios used as data points in the GOSIA χ^2 minimization [52]. Signs of mixing ratios use the Krane sign convention [56].

Matrix Element	Value
$\langle 8_1^+ \| E2 \| 6_1^+ \rangle$	0.19(3)
$\langle 4_2^+ \| E2 \| 2_2^+ \rangle$	0.093(12)
$\langle 4_2^+ \| E2 \| 4_1^+ \rangle$	0.040(5)
$\langle 4_2^+ \| E2 \| 2_1^+ \rangle$	0.006(1)

Table 3.5: The matrix elements from [55] used as data points in the GOSIA χ^2 minimization. Use of these transition matrix elements to so-called buffer states is described in Ch. 4.

Chapter 4

Results

Using GOSIA, matrix elements were successfully extracted. The reproduction of the measured yields is shown in Fig. 4.1. The left column of Fig. 4.1 shows how the fitted yield for each observed γ-ray transition compares to the measurements for the four scattering angle groups. It is noted that the yields in Coulomb excitation vary by orders of magnitude depending on the transition and the scattering angle region, underlining the sensitivity of the approach. The right column of Fig. 4.1 shows the number of standard deviations between measured and fitted yields. With only a few exceptions, the fitted and measured yields agree within 2 standard deviations or better, which is reasonable for quantities that vary over orders of magnitude.

The fit contained 26 matrix elements and 4 normalization constants (see Sec. 3.3), being fit to 25 γ-ray yields and 16 values from previous measurements. The reduced χ^2 reported from GOSIA resulting from this fit was 1.6. The 16 values from previous experiments are listed in Tables 3.2, 3.3, 3.4, and 3.5. These values are incorporated into the calculation of the χ^2, attempting to drive the multidimensional minimization towards a viable minimum. Four of the 16 values, listed in Table 3.5, provide a χ^2 contribution for so-called buffer states. These are the 8_1^+ and 4_2^+, the first nonobserved states in the yrast and yrare bands, respectively. In such Coulomb excitation calculations, these states account for possible high-lying states that were unobserved [57]. For the third of such buffer states, the 2_4^+, no input
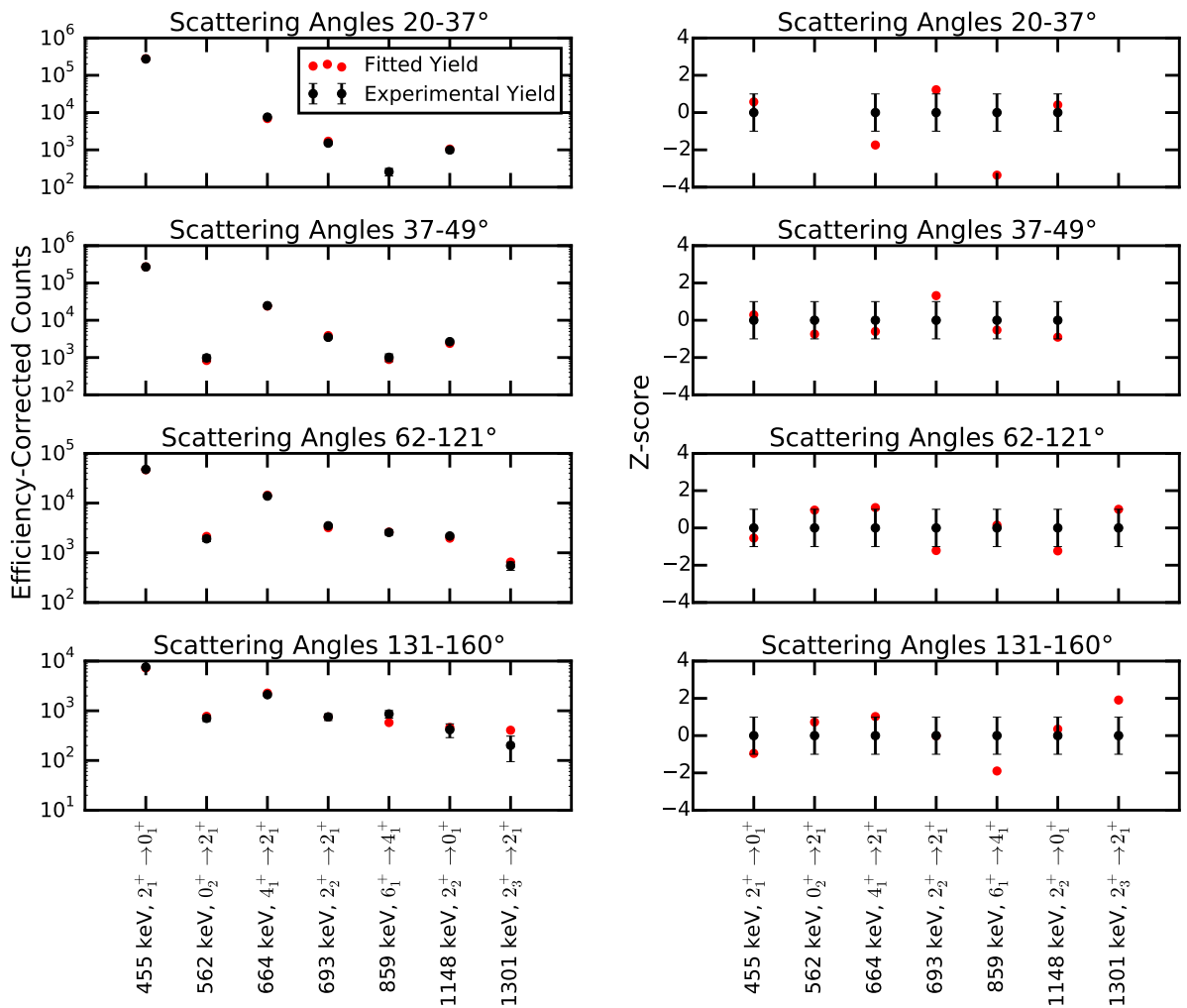
Figure 4.1: The fitted experimental yields for each observed γ ray transition. In black are the experimental values, and in red are the fitted values. The experimental yield was extracted from the peak areas corrected by the γ-ray detection efficiency. On the left are the fits to each peak area, in efficiency-corrected counts. On the right are the z-scores of the comparison, the number of standard deviations between the experimental values and the fitted values, for each data point. Missing points for certain angle groups indicate that a peak was not observed for that particular transition.

was provided to GOSIA. The uniqueness and robustness of this result was tested by providing randomized matrix elements as the initial parameters to the GOSIA minimization routine [36], then examining the resulting minimized χ^2, to identify if a better minimum could be found. Of 350 such minimizations, none of the random initial parameter sets resulted in a better χ^2 than the fit presented here.

In Tables 4.1, 4.2, and 4.3 are shown the transition E2 matrix elements, M1 matrix elements, and diagonal quadrupole matrix elements, respectively. It is noted that sensitivity to M1 transition matrix elements in low-energy Coulomb excitation is encoded in the γ-ray angular distributions of the de-exciting transitions with mixed E2/M1 multipolarity. The present setup and level of statistics did not lend itself to a detailed study of γ-ray angular distributions and, therefore, the extracted M1 matrix elements are based on the literature multipole mixing ratios that were part of the GOSIA minimization. For the same value of an M1 and E2 matrix element, the cross section for the excitation of an M1 mode is suppressed by $(v/c)^2$ and so any M1 information in the measured cross sections is negligibly small [35].

Transitions included in the Coulomb excitation calculation but constrained according to the asymmetric rigid rotor model (see Sec.3.3) are not included in the table. Measured results are compared with values taken from the 2009 NNDC evaluated data set [52], and with a low-energy Coulomb excitation measurement performed by Becker *et al.* [55], which used a beam of ^{78}Kr impinged on targets of ^{208}Pb, ^{48}Ti, and ^{26}Mg at various energies below the Coulomb barrier, in effect providing a data set that results from 6 different measurements. Most matrix elements agree with the literature values, as shown in Fig. 4.2. The results for each observed state and its transitions are discussed in detail below.

The 2_1^+ state at $455 \, \mathrm{keV}$, the first excited state of ^{78}Kr, decays by emitting a single γ ray, transitioning to the ground state. This $455 \, \mathrm{keV}$ transition has an extracted E2 matrix

I_i	I_f	$\langle I_f||E2||I_i\rangle$ [eb]	NNDC $\langle I_f||E2||I_i\rangle$ [eb]	Becker *et al.* $\langle I_f||E2||I_i\rangle$ [eb]
2_1^+	0_1^+	$0.81^{+0.01}_{-0.01}$	$0.82^{+0.01}_{-0.01}$	$0.82^{+0.02}_{-0.02}$
2_2^+	0_1^+	$0.159^{+0.005}_{-0.005}$	$0.13^{+0.01}_{-0.01}$	$0.157^{+0.003}_{-0.004}$
0_2^+	2_1^+	$0.243^{+0.016}_{-0.007}$	$0.31^{+0.01}_{-0.01}$	$0.30^{+0.01}_{-0.01}$
4_1^+	2_1^+	$1.30^{+0.02}_{-0.02}$	$1.25^{+0.04}_{-0.04}$	$1.27^{+0.05}_{-0.02}$
2_2^+	2_1^+	$0.43^{+0.02}_{-0.03}$	$0.24^{+0.05}_{-0.05}$	$0.26^{+0.06}_{-0.05}$
6_1^+	4_1^+	$1.63^{+0.07}_{-0.07}$	$1.56^{+0.09}_{-0.09}$	$1.61^{+0.06}_{-0.08}$
2_3^+	2_1^+	$0.084^{+0.004}_{-0.005}$	$0.068^{+0.004}_{-0.004}$	$0.50^{+0.02}_{-0.05}$
2_3^+	0_1^+	$0.0384^{+0.0007}_{-0.0007}$	$0.020^{+0.001}_{-0.001}$	$0.180^{+0.007}_{-0.008}$
4_2^+	2_1^+	$0.074^{+0.005}_{-0.006}$	$0.069^{+0.005}_{-0.005}$	$0.073^{+0.002}_{-0.005}$
2_3^+	0_2^+	$0.48^{+0.01}_{-0.01}$	$0.25^{+0.01}_{-0.01}$	$0.26^{+0.010}_{-0.01}$
2_3^+	4_1^+	$0.330^{+0.006}_{-0.006}$	$0.178^{+0.008}_{-0.008}$	$0.22^{+0.20}_{-0.05}$
2_3^+	2_2^+	$0.15^{+0.02}_{-0.37}$	$0.12^{+0.02}_{-0.02}$	$0.19^{+0.32}_{-0.05}$
4_2^+	2_2^+	$0.89^{+0.05}_{-0.07}$	$0.95^{+0.06}_{-0.06}$	$0.91^{+0.06}_{-0.04}$

Table 4.1: The E2 matrix elements and uncertainties as extracted by GOSIA, compared with values from NNDC [52] and Becker *et al.* [55]. Transitions below the horizontal divider were not directly observed in this experiment, but were included in the GOSIA minimization. Not shown are 3 ill-constrained matrix elements, including transitions from the 8_1^+ and 2_4^+ buffer states.

I_i	I_f	$\langle I_f||M1||I_i\rangle$ [μ_N]	NNDC $\langle I_f||M1||I_i\rangle$ [μ_N]	Becker $et\ al.$ $\langle I_f||M1||I_i\rangle$ [μ_N]
2_2^+	2_1^+	$0.33^{+0.02}_{-0.02}$	$0.30^{+0.03}_{-0.03}$	$0.38^{+0.01}_{-0.03}$
2_3^+	2_1^+	$-0.149^{+0.003}_{-0.002}$	$0.057^{+0.004}_{-0.004}$	$-0.41^{+0.12}_{-0.04}$
2_3^+	2_2^+	$0.09^{+0.02}_{-0.02}$	$0.016^{+0.014}_{-0.008}$	

Table 4.2: The M1 matrix elements and uncertainties as extracted by GOSIA, compared with values from NNDC [52] and Becker $et\ al.$ [55]. (See text for a discussion of the sensitivity to M1 transitions.)

I	$\langle I||E2||I\rangle$ [eb]	Becker $et\ al.$ $\langle I||E2||I\rangle$ [eb]	Q [eb]	Becker $et\ al.$ Q [eb]
2_1^+	$-0.96^{+0.11}_{-0.47}$	$-0.80^{+0.04}_{-0.04}$	$-0.73^{+0.08}_{-0.36}$	$-0.61^{+0.03}_{-0.03}$
4_1^+	$-1.2^{+2.4}_{-1.0}$	$-0.73^{+0.15}_{-0.14}$	$-0.9^{+1.8}_{-0.7}$	$-0.55^{+0.11}_{-0.10}$
2_2^+	$1.0^{+0.3}_{-0.7}$	$0.58^{+0.04}_{-0.08}$	$0.7^{+0.2}_{-0.6}$	$0.44^{+0.03}_{-0.06}$
2_3^+	$1.6^{+1.8}_{-0.5}$	$-0.22^{+0.09}_{-0.14}$	$1.2^{+1.4}_{-0.4}$	$-0.17^{+0.07}_{-0.10}$
6_1^+	$-0.8^{+2.2}_{-1.3}$	$-0.87^{+0.16}_{-0.12}$	$-0.6^{+1.5}_{-0.9}$	$-0.61^{+0.11}_{-0.08}$

Table 4.3: The diagonal matrix elements and uncertainties as extracted by GOSIA, compared with values from Becker $et\ al.$ [55]. Results are quoted both as diagonal matrix elements and as quadrupole moments. Not shown are 2 ill-constrained matrix elements.
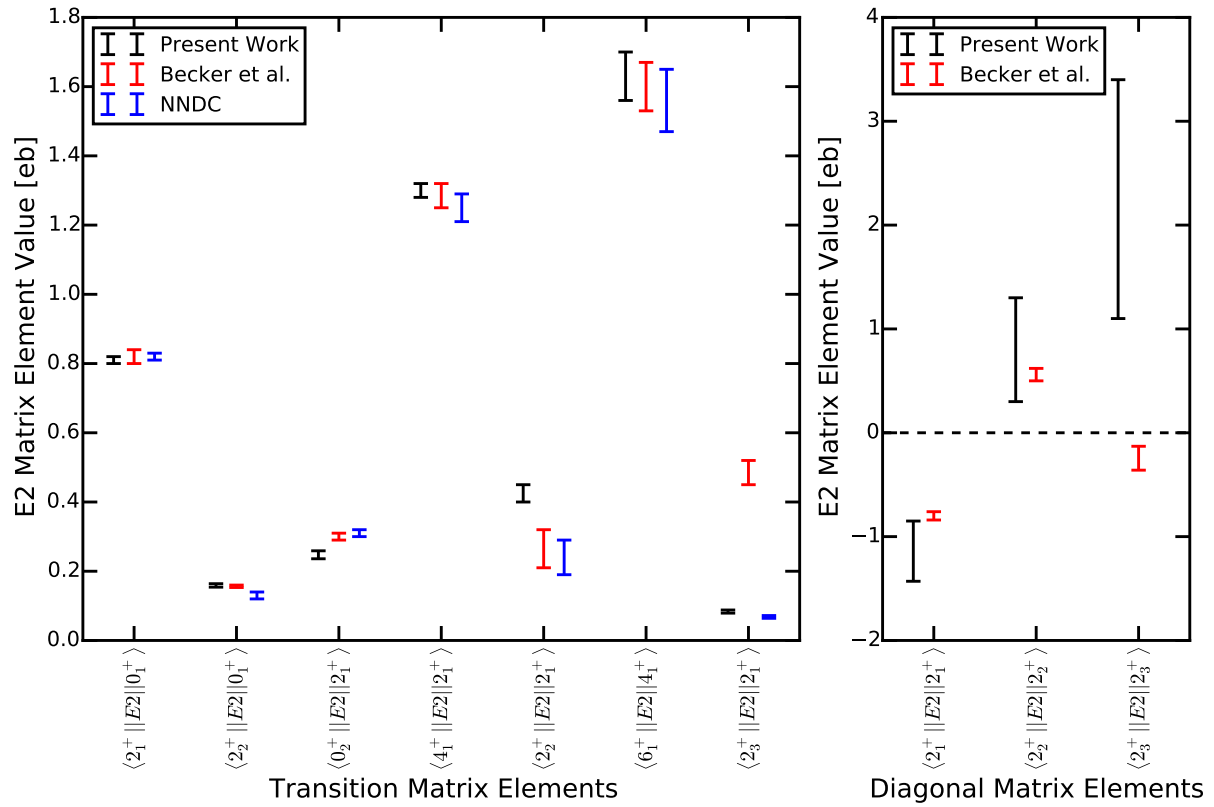
Figure 4.2: A comparison between transition and diagonal matrix elements measured in the present work, from Becker *et al.* [55], and from NNDC [52]. The comparisons are discussed in the text.

element that agrees within uncertainty both with the value reported in NNDC, and the value from [55]. The lifetime of the 2^+_1 state has been deduced before from various recoil-distance Doppler shift measurements [58, 59, 60, 61, 62, 63], Doppler-shift attenuation measurements [64, 65], and from the B(E2) value extracted in the earlier Coulomb excitation measurement [55]. As typical in these massive minimizations with GOSIA [66], the lifetime of the 2^+_1 state was used as an input to the χ^2 search in gosia.

The diagonal E2 matrix element of the 2^+_1 state was also extracted as $-0.96^{+0.11}_{-0.47}$ eb corresponding to a quadrupole moment of $-0.73^{+0.08}_{-0.36}$ eb, 1.4σ away from the value measured by Becker et $al.$ [55], but clearly indicating prolate deformation from its sign.

The second excited state, 0^+_2, at $1017\,\mathrm{keV}$ decays to the 2^+_1 by emitting a $561\,\mathrm{keV}$ γ ray. This transition is weak and not observed in the forwardmost 20-37° scattering angle region. The extracted matrix element for this transition is similar to previously measured values, though outside of the uncertainties of the measurements by 3.5σ. Previous measurements of the lifetime of this state compiled in NNDC [52], derived from Doppler-shift attention measurements [67] and Coulomb excitation [55], are used in the χ^2 minimization. When no previous measurements are used in the GOSIA minimization, the $\langle 2^+_1 ||E2|| 0^+_2 \rangle$ extracted matrix element does not change within the uncertainty reported here.

The 4^+_1 state at $1119\,\mathrm{keV}$ is part of the yrast band, and only decays to the 2^+_1 state by emitting a $664\,\mathrm{keV}$ γ ray. The literature value of the lifetime of the 4^+_1 state compiled in NNDC [52] and derived from [58, 59, 60, 61, 62, 63, 68, 64, 65, 55] was used as an input to the GOSIA minimization. The E2 matrix element reproduces previous measurements, both from NNDC and from Becker et $al.$. The quadrupole moment is also reproduced, though with a large uncertainty. In fact, the uncertainty is so large that the measurement carries no sensitivity to the value or the sign.

The 2^+_2 state at 1148 keV can decay either to the 2^+_1 state by emitting a 691 keV γ ray, or to the ground state by emitting a 1148 keV γ ray. The previously measured lifetime of the 2^+_2 was included in the GOSIA χ^2 minimization from NNDC [52], derived from [55, 59, 62, 64]. The measured value of $\langle 0^+_1 ||\text{E2}|| 2^+_2 \rangle$ agrees with the value obtained by Becker *et al.* to within 0.3σ, though both measurements disagree with the value reported in NNDC [52]. The $\langle 2^+_1 ||\text{E2}|| 2^+_2 \rangle$ matrix element of $0.43^{+0.02}_{-0.03}$ eb is larger than either previous value by 2.5σ. It is reminded that there is no sensitivity to the known M1 component in the decay, and so the multipole mixing ratio of the 691 keV transition was input as $\delta = -0.45(10)$ [52]. The resulting M1 matrix element of $0.33^{+0.02}_{-0.02} \mu_N$ agrees with the literature value from NNDC [52]. The measurement of this M1 matrix element by Becker *et al.* as $0.38^{+0.01}_{-0.03} \mu_N$ is outside of the uncertainty both of the literature value from NNDC and the value in the present work. Attempts were made to fit the experimental yields while keeping $\langle 2^+_1 ||\text{E2}|| 2^+_2 \rangle$ fixed at the previously measured value of $0.26^{+0.06}_{-0.05}$ eb. This constraint increases the reduced χ^2 from 1.6 to 2.5, while also increasing the values of the $\langle 2^+_2 ||\text{E2}|| 0^+_1 \rangle$ to $1.71^{+0.06}_{-0.01}$ eb and $\langle 2^+_3 ||\text{E2}|| 2^+_1 \rangle$ $0.12^{+0.01}_{-0.01}$ eb, outside of the range of agreement with previous measurements.

The 2^+_3 state at 1752 keV can de-excite to any of the 0^+_1, 2^+_1, 0^+_2, 4^+_1, or 2^+_2 states. Of these transitions, only the strongest transition to the 2^+_1 state was directly observed here. Other transition matrix elements are included in the Coulomb excitation calculation, but do not correspond to observed γ-ray transitions, and are therefore poorly constrained in the GOSIA χ^2 minimization. Branching ratios from the evaluated NNDC database [52], themselves derived from [69, 59, 70], of all transitions from the 2^+_3 state are therefore included as additional inputs the GOSIA (Table 3.3). These branching ratios and the observed $2^+_3 \rightarrow 2^+_1$ transition are the primary source of the corresponding matrix elements. The remarkably low uncertainty for the matrix elements extracted for such unobserved transitions is solely based
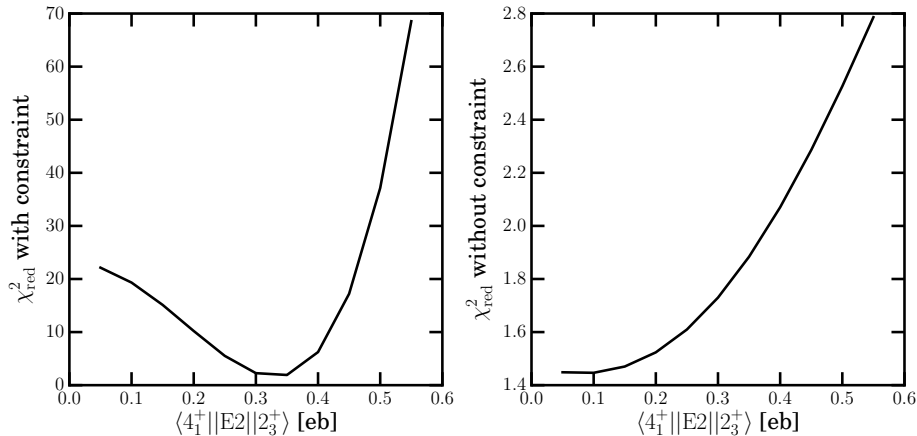
Figure 4.3: The χ^2 curve of the $\langle 4_1^+ || E2 || 2_3^+ \rangle$ matrix element, with and without the branching ratio constraint in the GOSIA fit.

on the branching ratios and their uncertainties. An extraction of such values is therefore questionable. The agreement with Becker *et al.* is poor. One can explore the disagreement and check for inconsistencies of the present data and literature values. For example, a comparison of the χ^2 curve when varying the $\langle 4_1^+ || E2 || 2_3^+ \rangle$ matrix element, with and without the branching ratio constraint, is shown in Fig. 4.3. The large discrepancy between them may be an indication of an inconsistency between previous measurements of the matrix element and previous measurements of the branching ratio as they cannot be consolidated in the present data set. The literature values of the E2/M1 multipole mixing ratios for the $2_3^+ \rightarrow 2_2^+$ and $2_3^+ \rightarrow 2_1^+$ transitions (Table 3.4) were included as additional inputs to the GOSIA χ^2.

The quadrupole moment of the 2_3^+ state is significantly different than the previous measurement by [55]. Though the uncertainty in the current measurement is large, it does exclude all negative values, suggesting that this state is oblate, rather than prolate, from this work. Attempts to fit the measured yields here using the $\langle 2_3^+ || E2 || 2_3^+ \rangle$ value of -0.22 eb, allowing all other parameters to vary, resulted in a reduced χ^2 of 1.8, as opposed to the mini-

mum reduced χ^2 found of 1.6. Most matrix elements in the modified fit change only slightly, with the exception of the $\langle 2_3^+ ||\mathrm{E2}|| 2_1^+ \rangle$ matrix element, which changes to $0.131^{+0.003}_{-0.004}$ eb, far from previously measured values. This change, along with the increased χ^2, shows that there is no obvious variation of parameters that can explain the measured yields using the value of $\langle 2_3^+ ||\mathrm{E2}|| 2_3^+ \rangle$ from [55].

The highest state observed was the 6_1^+ state at 1977 keV, which decays to the 4_1^+ state by emitting a 857 keV γ ray. The known lifetime of this state was included in the χ^2 calculation (Table 3.2). The extracted transition matrix element agrees with [55] and NNDC.

In total, the agreement between the matrix elements extracted here and the literature values is satisfactory, given that the 2-day measurement reported here was performed at a single beam energy on a single target, whereas Becker *et al.* [55] used in effect 6 measurements to extract their results. The inconsistences uncovered for some matrix elements of the 2_2^+ and 2_3^+ states require complementary data for a resolution. In particular, sensitivity to the sign of the quadrupole moments is demonstrated for all 2^+ states in this analysis.

Chapter 5

Summary and Outlook

The SeGA-JANUS experimental setup was successfully commissioned, and is ready to be used for inverse-kinematics low-energy Coulomb excitation experiments with rare isotope beams. The existing SeGA detectors were transitioned to a digital data acquisition system, and coupled to an analog data acquisition system for the silicon detectors. The two systems were read out using the NSCLDAQ framework, and analyzed using GRUTINIZER. The experimental setup was tested using a ^{252}Cf fission source, and was commissioned in-beam, performing low-energy Coulomb excitation of ^{78}Kr. From this experience and work from other low-energy facilities, it is concluded that rates of 10^4-10^5 particles per second will be sufficient for performing rare-isotope experiments, depending of course on the degree of collectivity of the nucleus of interest and the length of the run.

Since the commissioning run, the silicon detectors used in JANUS were transitioned from the analog data acquisition system described in this work to a digitizer-based system similar to that used for SeGA. This greatly simplifies the electronics part of the experimental setup data acquisition, and asynchronous reading of the processed events from the digitizer modules allows for a near-zero deadtime of the particle detectors [44]. The modified data acquisition system was successfully tested with a ^{252}Cf source, identical to the earlier test described in Sec. 2.4.

The JANUS setup will be used to study collectivity in rare isotope beams at NSCL now,

and at FRIB in the future. Unlike for ISOL facilities, which have chemistry-dependent restrictions on beam production based on which elements can be efficiently extracted from a thick production target, NSCL's unique technique of beam production by in-beam fragmentation, gas stopping, and reacceleration allows for low-energy rare-isotope beams not limited by chemical properties. As FRIB comes online, the variety of available beams and their intensity will increase, enabling studies of collectivity far from the valley of β stability.

Of particular interest are nuclei not available at ISOL facilities, for example, the neutron-rich sulfur isotopes, leading up to the $N = 28$ magic number. $^{44}_{16}S_{28}$ has previously been found to have low-lying quadrupole collectivity [71, 72], and configuration [73, 74, 75, 76] and shape coexistence [77, 78, 79], indicating that the $N = 28$ magic number breaks down in this region and elucidating the mechanism behind this breakdown. Low-energy Coulomb excitations of $^{42-44}$S would enable — for the first time — to prove and quantify shape coexistence from measurements of the sign and magnitude of the quadrupole moment, while also tracking the collective structures to higher spin.

Preparatory research in this region is presented in Appendix C, which reports the detailed γ-ray spectroscopy of the neutron-rich sulfur isotopes up to $A = 42$ using the γ-ray detector array GRETINA and the S800 spectrograph with NSCL's fast beams. At present, the beam rates available in this region are insufficient to perform low-energy Coulomb excitation. As the beam availability and intensity increases in the S chain and other regions of shape coexistence, low-energy Coulomb excitation experiments will provide measurements of collectivity beyond the first 2^+ state and information on nuclear shapes, which will help further the understanding of nuclear structure in exotic nuclei.

APPENDICES

Appendix A

GRUTinizer Development

GRUTINIZER is a new analysis package designed to be configurable for use in many experiments, handle multiple input formats, and allow custom user-configurations for analysis of any detector system. The project was developed in conjunction with the current work. GRUTINIZER is multi-threaded to best take advantage of modern multi-core computer architectures, allowing for quick sorting of raw data, either read from disk or streamed live during an experiment. While the underlying sorting framework is original, many of the user friendly analysis and display features included are based on the ROOT framework[80].

Pipeline

The primary goal of GRUTINIZER is to transform raw binary data into human-readable structures while minimizing the amount of programming knowledge required by the experimenter. on the part of the experimenter. GRUTINIZER presents the user with an analysis pipeline, each section of which performs a single step in the analysis process. These steps represent high-level actions, such as reading raw binary data from a file or time-correlating events, and can be customized according to one's individual needs.

The overall analysis pipeline consists of many steps, with each physics event being processed by all steps, one at a time. In the most basic setting, raw data read from a source undergoes four basic steps. First, the individual raw data packets are sorted by timestamp
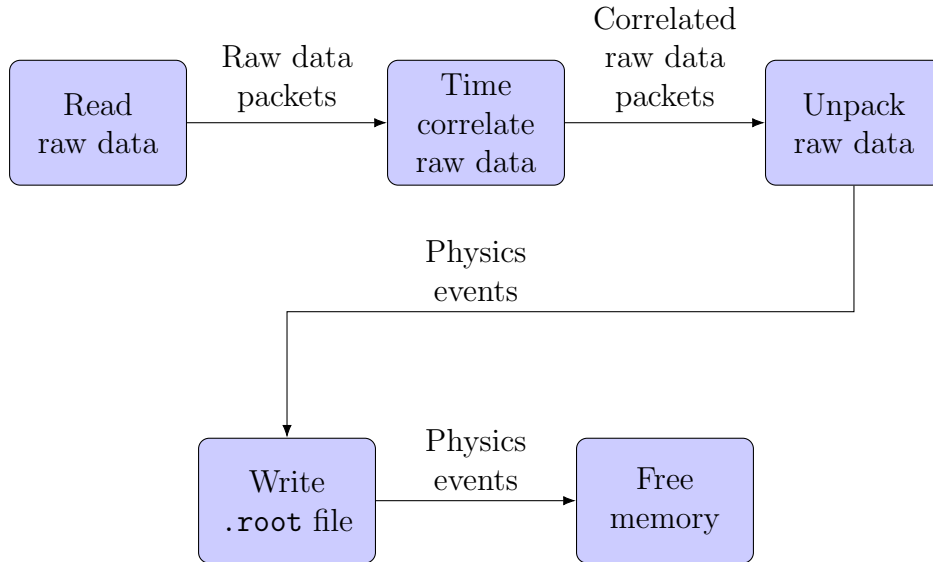
Figure A.1: The analysis pipeline of the simplest use of GRUTINIZER

and grouped into time-correlated event packets. These event packets may contain raw data
from multiple independent detector systems. Next, each raw data packet within an event is
sent to the appropriate unpacker for the detector system that produced it. The job of each
unpacker is to convert the raw data, as packed by its corresponding data acquisition(DAQ)
systems, into a readable structure usable for representing the specific detector system. These
unpacked data structures then have the option to either be written directly to disk in the
form of a ROOT tree or to have desired information extracted and histogrammed, discussed
in more detail in App. A. Finally, the in-memory representation of the data is freed. This
flow of data through the analysis pipeline is shown in Fig. A.1.

Each computation step described above is independent, and is performed on a different
thread. This allows, for example, the reading of data from disk to occur simultaneously
with unpacking, rather than each step being performed sequentially by one processor. In
addition, each processing step is interchangeable, requiring only that the appropriate inputs
be provided, and the outputs be consumed. This allows additional computational steps to
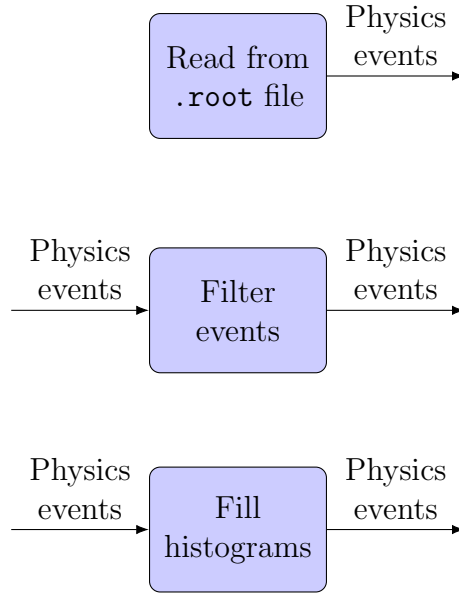
Figure A.2: Additional components that can be added to the GRUTINIZER analysis pipeline.

be added to the pipeline, so long as they provide the appropriate outputs for later processing steps.. Rather than reading from a raw data file, for example, GRUTINIZER can read from a previously generated `.root` file, reading the unpacked data structure directly from the stored tree to further process the data. Additional computational steps commonly added to an analysis pipeline are shown figuratively in Fig. A.2.

This flexibility allows for a wide variety to the analysis pipeline. For example, one could read from a `.root` file, filter the values, histogram the results, then write the filtered events to a `.root` file.

The read loop is capable of reading from multiple different file formats, containing binary data packets. The raw data may be read from a raw file, from a compressed file, or directly from an NSCL ringbuffer. The data format can be either the NSCL's internal EVT format, the output of the Global Event Builder (GEB) used by GRETINA, or a ROOT tree. GRUTINIZER handles the unpacking of these data formats, presenting a uniform interface

for all unpacking steps, allowing for a large amount of code reuse. For example, S800 data written either through the NSCL data packer or through the GRETINA data packer can be unpacked with the same code.

While being read out, a timestamp is extracted for each data packet. These data packets are sorted according to their timestamps, and are grouped into packets similar in time. Correlated data packages originating from multiple detector systems, referred to earlier as event packets,are then processed together throughout all subsequent pipeline steps. The correlation is done using a FIFO-like queue with a user-definable depth and time window, and alerts the user if the depth is insufficient to sort the data.

Unpacking is largely done with user-defined code specific to an individual detector. This code takes a group of raw data packets and converts it into a user-friendly data structure representing an entire detector system. These systems are usually composed of detectors containing many individual hits, each of which is derived from a single raw data packet. Implementation of additional unpackers is described in App. A.

After the unpacking step, many options are available for use. The user-friendly data structures can be written to disk in the form of a ROOT tree. Alternatively, these data structures can be re-packed into raw data and written to disk. This is particularly useful, as the flexibility of the pipeline allows a filter to be applied before writing, pruning unwanted from the data, for example from another reaction channel. In such a way, one can perform future steps in the analysis including only the events most important to the overall physics goal. Additionally, events can be histogrammed, then either saved to a ROOT data structure or displayed on screen.

The ability to unpack, filter, histogram, and store sorted data allows for powerful analysis using GRUTINIZER. Some of the common usage will be explained in the following section,

which can be expanded on a case-by-case basis.

Having a common sorting framework and analysis tools has proven to be extremely useful. This framework has allowed many detector systems to be analyzed in a common manner. GRUTinizer handles the reading of input files, the parsing of timestamps, the grouping of events that happen nearby in time, and the writing of the output file in a semi-automatic fashion. These are steps that are common to all analyses, and need not be recreated for each analysis. Such an approach has had the added side effect of providing a large user base, which in turn helps gather all user contributions into a common code.

Usage

Please be aware, usage and implementation details may change in the future.

Installation

GRUTinizer requires a current installation of `ROOT`, version 6, along with Python2.7. Once these are installed, to compile GRUTinizer, first clone the current version from github, then compile using `make`.

```
git clone https://github.com/pcbend/grutinizer
cd grutinizer
make
```

In order to load environment variables which allow path independent user-code compilation and running GRUTinizer, the included `thisgrut.sh` file can be sourced. The primary effect of this file is adding the `bin` directory of GRUTinizer to the user's `PATH` variable.

```
source /my/path/to/grutinizer/thisgrut.sh
```

Class Structure

Detector systems in the GRUTinizer frame work derive from two main classes, `TDetector` and `TDetectorHit`. `TDetector` is intended as a full description of a detector system's output in a single event. `TSega` and `TJanus` are two examples of `TDetector` subclasses, representing the γ-ray and particle detections in the SeGA-JANUS setup. Each subclass must provide a `BuildHits()` method, which unpacks raw binary data from the detector into the class structure. This is required for any new system that is added to the GRUTinizer framework.

The `TDetectorHit` class is not required, but provides features that make it easier to implement a new detector. It is intended to represent a single channel, or detecting element, on a detector. Each `TDetectorHit` is intended to hold the uncalibrated time and energy collected in a single event for a single channel. These are calibrated using the `TChannel` tool, described in App. A as needed. Additional information specific to each detector can be included by creating a subclass of `TDetectorHit`, such as the channels individual position.

Once a user has created their new subclass of `TDetector`, it needs to be integrated into the unpacker, so that GRUTinizer can identify data originating from that detector system. This is done by editing the `GRUTinizer/include/TGRUTTypes.h` file to include a new entry in the `kDetectorSystems` enum, then editing the `GRUTinizer/libraries/` `TGRUTint/TGRUTTypes.cxx` file to include references to the new system. `TGRUTTypes.cxx` contains two maps that are used by the GRUTinizer unpacker. The first maps from strings to enums, and must have a new entry made corresponding to the new entry in `kDetectorSystems`. This is used in the parsing of the `.env` file described in App. A. The

second maps from enums to classes, and is used when determining which class needs to be constructed. In both cases, edit the map to have a new entry for the new detector, following the format of the existing entries.

Additional details on this process can be found at the GRUTINIZER wiki, located at `https://github.com/pcbend/GRUTinizer/wiki`.

Configuration Files

GRUTINIZER is designed to handle many different data formats and detector systems. While much of the configuration need to sort the data is assumed by the program, sometimes additional input is needed. For GRETINA data, the event type of each data packet is used to determine to which detector the data packet belongs. These event types correspond to a static list maintained by the GRETINA project. For NSCL data, the source id plays a similar role. However, the source id may change from experiment to experiment. For this reason, a configuration file is used to specify which source ids correspond to which detectors. The default configuration file is located at `GRUTinizer/config/DetectorEnvironment.env`, and can be overridden by passing a replacement file to GRUTINIZER on the command line. For example, in the SeGA-JANUS commissioning experiment, source ids 1, 2, and 3 corresponded to SeGA data, while source id 4 corresponded to JANUS data. The following configuration file was therefore used.

```
Sega: 1 2 3

Janus: 4
```

While histogramming or filtering objects, it may be desirable to have some user-configurable settings. In order to handle such variables, GRUTINIZER has the concept of `GValues`, which

can be passed in from the command line and accessed from within the histogram or filtering libraries. Additionally these parameters help in real-time analysis; for example, in making Doppler reconstructed histograms with SeGA and JANUS systems, the value of β, was a `GValue` to allow it to be determined at run time. The values are intended to be configuration parameters relating to a detector system as a whole, such as relative positioning between detector systems. These configuration parameters are globally available, and can easily be loaded from a configuration file, or modified at runtime through the GRUTINIZER GUI. Additionally, the values are written in plain-text files with the file extension `.val`. An example of such a file is shown below. In a histogram or filter library, these values can be accessed by calling `GValue::Value("beta")`, where the argument is the name of the value being requested.

```
beta {
  Value: 0.085
}
```

While the `GValue`s are good for handling of high-level parameters, detectors can also require a large number of calibration parameters. In this case, it would become unwieldy to have an independent `GValue` for the slope and offset of each channel. For this purpose, GRUTINIZER has the concept of `TChannel`s, which provide a few common uses. For example, below is the channel specifying that the SeGA detector located at address `0x01010201` has calibration `energy = 0.086637*channel + 0.017`.

```
SEG02AP00 {
  Address: 0x01010201
  EnergyCoeff: 0.017 0.086637
```

```
    }
```

On its own, the `TChannel` provides a useful parser, and functions to apply channel-specific corrections, such as time and energy calibrations. This utility is coupled with the GRUTinizer data structures, in order to provide ease of use to users.

Histogramming and Filtering

Throughout an experiment, different histograms may be needed for diagnostic and analysis purposes. These histograms depend on the detectors present in the given experiment, and may change rapidly as the needs of analysis change. To accommodate this, GRUTinizer makes it easy to create a histogram definition file detailing the histograms that should be produced. These definition files consist of compiled C/C++ code, allowing full flexibility for any calculations that need to be run. While the definition file fills the histograms, all memory management and output files are managed by GRUTinizer, simplifying the process significantly. Additionally, these histograms can be viewed and manipulated as they are being filled, giving real-time feedback to the experiment.

In order to histogram data, a histogram library must be generated. Samples of these are included in the `histos` subdirectory of the GRUTinizer source directory. Additional histogram files created in this directory will be automatically compiled by the GRUTinizer makefile into a shared library. A simple example of such a file is shown below.

```
#include "TRuntimeObjects.h"


extern "C"
void MakeHistograms(TRuntimeObjects& obj) {
```

```
    TSega* sega = obj.GetDetector<TSega>();

    TJanus* janus = obj.GetDetector<TJanus>();


    if(sega && janus) {

        obj.FillHistogram("tdiff",

                          400, -2000, 2000,

                          sega->Timestamp() - janus->Timestamp());

    }

}
```

The entrance point is the `MakeHistograms` function. This will be called once for every time-correlated event in the input file. The single argument, `TRuntimeObjects& obj`, is the entrance point both for accessing data about the event, and for specifying histograms to be generated.

In order to access data from the event, use the `obj.GetDetector` method. This is a templated method that will return a pointer to that detector object if the current event contains that detector type, or will return a null pointer if the current event does not contain that detector.

To make a histogram, use the `obj.FillHistogram` method. This accepts the name of the histogram to be filled, the number of bins, the low end of the histogram range, the high end of the histogram range, and finally the value that should be filled into the histogram. By combining these parameters into a single function call, it is possible to add new histograms by editing only a single location in code.

Filters to remove unwanted data are generated in a similar manner. The main difference

is that the entrance function is named `FilterCondition` rather than `MakeHistograms`. The `FilterCondition` function should return true if the event is to be kept, and false if the event should not be kept. Below is an example filter that will keep only events in which both SeGA and JANUS data are present.

```
#include "TRuntimeObjects.h"


extern "C"
bool FilterCondition(TRuntimeObjects& obj) {
  TSega* sega = obj.GetDetector<TSega>();
  TJanus* janus = obj.GetDetector<TJanus>();


  if(sega && janus) {
    return true;
  } else {
    return false;
  }
}
```

In both histogram libraries and filter conditions, it may be advantageous to use two-dimensional gates defined previously. These gates can be saved using the `TCutG` class provided by ROOT or the reimplemented `GCutG` class, provided by the GRUTINIZER to ease S800 analysis. If `TCutG` objects are saved to a ROOT file with the file extension `.cut` and passed to GRUTINIZER, they will be available for use inside histogram and filter libraries. They can be accessed by calling `obj.GetCut("MyCutName");`.

Program Usage

The simplest usage of GRUTinizer is as an interpreter, based on the default ROOT interpreter. To start the GRUTinizer interpreter, simply run the program without any arguments.

```
grutinizer
```

Options accepted by GRUTinizer are listed by passing the `--help` option, the output of which is shown below.

```
GRUT_RELEASE: 1.02.00

        Release the Chipper Chartreuse Chipmunk!
Options:

  arg                         Input file(s)

 -o [ --output ] arg          Root output file

 -f [ --filter-output ] arg   Output file for raw filtered data

 --hist-output arg            Output file for histograms

 -r [ --ring ] arg            Input ring source (host/ringname).
      Requires --format to be specified.

 -l [ --no-logo ]             Inhibit the startup logo

 -H [ --histos ]              attempt to run events through
    MakeHisto lib.

 -n [ --no-sort ]             Load raw data files without
      sorting

 -m [ --sort-multiple ]       If passed multiple raw data files,
      treat them as one file.
```

```
-s [ --sort ]                  Attempt to loop through root files

   .

-t [ --time-sort ]             Reorder raw events by time

--time-sort-depth arg          Number of events to hold when time

     sorting; default value 100000

--build-window arg             Build window, timestamp units

--long-file-description        Show full path to file in status

   messages

--format arg                   File format of raw data.  Allowed

   options are "EVT" and "GEB".If unspecified, will be

   guessed from the filename.

-g [ --start-gui ]             Start the GUI

-w [ --gretina-waves ]         Extract wave forms to data class

   when available.

-q [ --quit ]                  Run in batch mode

-h -? [ --help ]               Show this help message

-v [ --version ]               Show version information
```

These are described in more detail below.

- `--output` allows the user to specify the name of the ROOT file to contain the unpacked

  data in a ROOT tree. If a filter condition has been passed, this output will be filtered. If

  GRUTINIZER is sorting over raw data and no output file has been explicitly specified,

  a name will be automatically generated. To disable output of the ROOT tree, pass

  `/dev/null` as the output file.

- `--filter-output` enables output of raw data to the specified file, with only events that have passed the filter condition being written.

- `--hist-output` allows the user to specify the name of the output ROOT file to contain generated histograms. If GRUTinizer is histogramming data and no output file has been explicitly specified, a name will be automatically generated. To disable output of the ROOT tree, pass `/dev/null` as the output file.

- `--ring` specifies a NSCL ringbuffer[45] from which to read data. If this option is specified, the `--format` option must also be given.

- `--no-logo` suppresses the display of the GRUTinizer logo on program start.

- `--histos` enables histogram generation.

- `--no-sort` will disable sorting over raw data files. This is used to examine raw data files manually.

- `--sort-multiple` causes multiple raw files passed in to be sorted concurrently. This is intended for data acquisition systems that write to multiple files simultaneously. In this mode, events from multiple files are read in, and are sorted in order in increasing timestamp, regardless of which raw file contains each individual event. Without this option, multiple raw files will be sorted sequentially, in the order they are passed in on the command line.

- `--sort` will enable sorting over ROOT trees.

- `--time-sort` enables sorting of events by increasing timestamp.

- `--time-sort-depth` gives the maximum number of events to be kept in memory simultaneously when sorting events by timestamp. Should this number be insufficient, a diagnostic will be issued to the user.

- `--build-window` gives the maximum separation between two raw data packets in a time-correlated event packet. This value is in the same units as the timestamps in the raw data file.

- `--long-file-description` enables a long description of the file in status messages.

- `--format` explicitly states the file format of the raw data source, and must be either "GEB" or "EVT". If unspecified, it is assumed that files ending with the extension `.evt` are NSCL data files and files ending with the extension `.dat` are GRETINA data files. When reading from a ring with the `--ring` option, the `--format` option is mandatory.

- `--start-gui` initializes the GRUTinizer graphical user interface on program start.

- `--gretina-waves` enables the extraction of waveforms when reading GRETINA data that contains waveforms. Otherwise, the waveforms are skipped.

- `--quit` quits GRUTinizer after handling all arguments. If not specified, GRUTinizer will instead display an interactive C++ prompt.

- `--help` will display the help message, then quit.

- `--version` will display the version information, then quit.

In addition, input files are recognized by their file extension. Known file extensions are as follows.

- `.evt`: NSCL data files.

- `.dat`: GRETINA data files.

- `.cal`: Calibration files containing `TChannel` definitions.

- `.val`: Calibration files containing `GValue` definitions.

- `.root`: ROOT files. These are automatically opened on startup.

- `.c`, `.C`, `.c+`, `.C+`, `.c++`, or `.C++`: ROOT macro files. These are executed after opening all ROOT files.

- `.env`: The detector environment file, which provides a mapping from source id to detector system, as described in App. A.

- `.so`: A shared object library containing either histogram definitions or a filter condition. If the function `MakeHistograms` is present, the library is recognized as a histogram library. If the function `FilterCondition` is present, the library is recognized as a filter condition.

- `.inv`: An inverse map, used for the S800 spectrograph[81].

- `.cuts`: A ROOT file containing 2-dimensional gates, saved as `TCutG` objects. These are available for use in filter and histogram libraries, as described in App. A.

In order to sort data, pass the data file in as an argument. GRUTINIZER will recognize file extensions `.evt` as the NSCL data format, and `.dat` as GRETINA data files. In addition, if the file extension is `.evt.gz` or `.dat.gz`, it will be interpreted as a gzipped file in NSCL format or GRETINA format, respectively, and will be unzipped accordingly. An output file

can be manually specified with the `-o` option, as shown below. If no such option is given, the output root file's name will be automatically generated, based on the run number in the filename.

```
grutinizer run -1234-00.evt -o run -1234-00.root -q
```

In order to signal to grutinizer that it should generate histograms, the histogram shared library must be passed in, and an output histogram file specified. The output filename can be explicitly specified using the `--hist-output` argument, or can be automatically generated using the `-H` argument. Examples of these two methods are shown below.

```
grutinizer run -1234-00.evt hist_lib.so \
                --hist -output=hist -1234-00.root -q
grutinizer run -1234-00.evt hist_lib.so -H -q
```

When generating histograms from a raw file, it may be desirable to suppress the writing of the root tree itself. While useful for analysis, writing a root tree is the slowest part of the analysis pipeline. In order to prevent a root tree from being created, specify the output file as `-o /dev/null`.

Graphical User Interface

As it's most visible aspect, GRUTinizer contains a graphical user interface (GUI) for interacting with ROOT objects, as well as giving the user a convenient way to interact with many of the internal pieces of the GRUTinizer framework.

The graphical user interface can be started from the command line. This contains a browser for displaying histograms, along with access to internal variables used by GRUTinizer. The GUI can be opened by passing the `-g` option, as shown below, or by running

the `StartGUI()` function in the interpreter. A screenshot of the GUI is shown in Fig. A.3.

```
grutinizer -g merged.root
```

Additional Tools

This framework contains many tools built on top of the capabilities already provided by ROOT. These are intended to make analysis steps easier by automating many common tasks in γ-ray spectroscopy, while being integrated into the standard ROOT user interface wherever possible. A few such tools are described here, with further described available on the GRUTinizer wiki, located at `https://github.com/pcbend/GRUTinizer/wiki`.

- By clicking on a one-dimensional histogram, one can define a region. With a keyboard shortcut, the area within the region is then fit with a Gaussian distribution.

- The `TCalibrator` tool is designed to automatically perform calibration of a germanium γ-ray detector, given the known energies of a radioactive source and a measured spectrum. This automation in particular has saved a large amount of time in calibration of the many channels present in segmented germanium detectors.

- Automatic shortcuts for performing projection and background subtraction of a two-dimensional γ-γ matrix.

- A shortcut to perform an integral of a histogram within a marked region.

As with most software, GRUTinizer is still in development, and improvements continue to be made. Modifications are welcome, and can be submitted at `https://github.com/pcbend/GRUTinizer`.
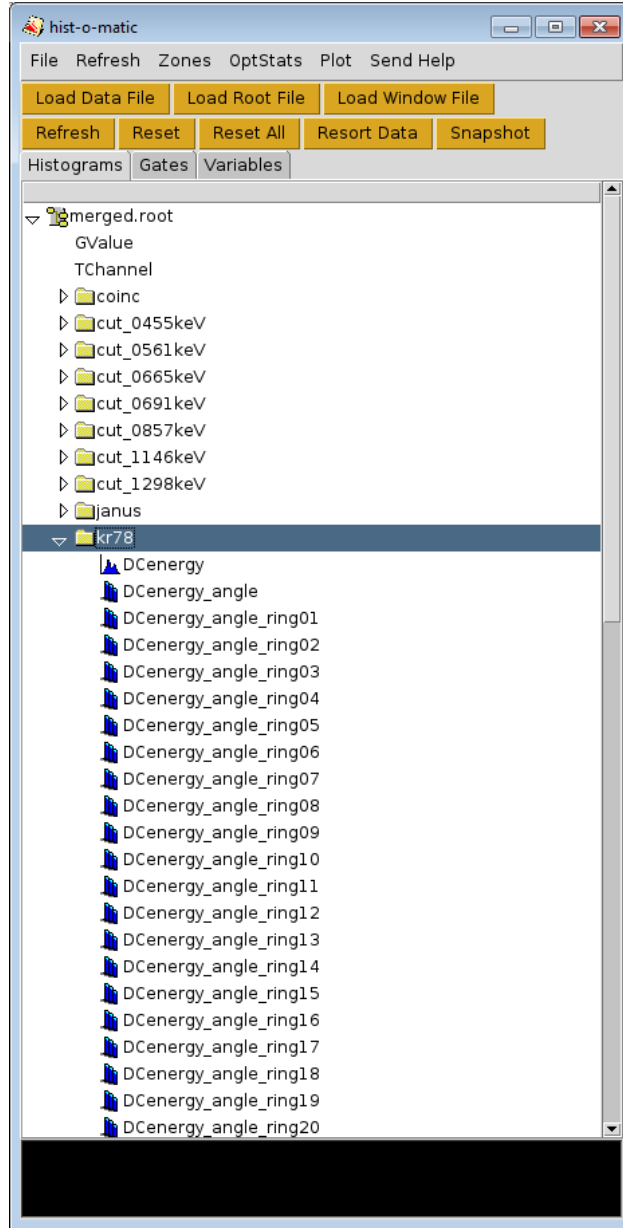
Figure A.3: A screenshot of the GRUTinizer graphical user interface, exploring a `.root` file containing histograms.

Appendix B

Gosia Analysis Procedure in More Detail

GOSIA [38] is a program designed to analyze Coulomb excitation experiments, extracting transition strengths and moments. It takes as input a description of the level scheme, along with allowed E1 through E6, M1, and M2 transitions between levels, as shown in Fig. 3.16. Experimental data are given as intensities and uncertainties for observed γ-ray transitions, gating on different regions in scattering angles, as shown in App. B.

The general process of running GOSIA involves four main steps. First, the experimental yields are corrected for finite angular range of the particle detectors and finite projectile energy range due to energy loss in the target. Use of these corrected yields allows subsequent processing done by GOSIA to calculate the yield at a single value of scattering angle and projectile energy, rather than integrating over a range of each, saving computation time [36].

Second, the matrix elements are varied to best reproduce the experimental yields, minimizing the χ^2. This χ^2 is computed based on the difference between the calculated yields and the experimental yields. In addition, differences between calculated and experimental values of any additional information provided to the fit, such as lifetimes, multipole mixing ratios, and branching ratios, contribute to the χ^2 being minimized.

Finally, the uncertainties of the extracted matrix elements are calculated. For reasons

expressed in detail in [36], this is not done through the traditional method of finding the matrix elements that result in a χ^2 value equal to $\chi^2_{\min} + 1$, where $\chi^2_{\min}$ is the minimum value of χ^2. Instead, an integral is performed over the likelihood of observing the data, relative to the integral over all values of the parameter. This is done in two steps, first finding the uncertainty of the matrix elements while keeping all other matrix fixed, known as the diagonal errors. The second step performs a full error estimation, determining the uncertainties of each parameter including corrections for correlations between matrix elements.

Performing each step requires making modifications to the input file, then re-running GOSIA. The exact modifications needed are described after the example input file. This section is concerned with when each step should be run, rather than how they are performed.

The minimization step is the most frequent step performed, and so it is the mode described with the unmodified input file below. In order to correct for finite detector size and target thickness, see the section on lines 126-150, describing the `OP,CORR` option. In order to compute diagonal errors, see lines 152-155, describing the `OP,ERRO` option. For the final correlated error calculation, see lines 162-165, also using the `OP,ERRO` option.

When performing the minimization, one adjusts the initial parameters, potentially adding values from previous measurements. These values can include matrix elements themselves, but can also include other measurements such as lifetimes, mixing ratios, and branching ratios. These are used as additional values contributing to the total χ^2.

Since the matrix elements themselves affect the corrections for finite detector size and target thickness, these corrections should be re-run whenever the fitted matrix elements change significantly during a minimization step. Afterwards, the minimization is repeated again.

When performing the correlated uncertainty calculation, the diagonal uncertainty calcula-

tion must have been performed immediately prior. This is because the correlated uncertainty calculation relies on intermediate files generated by the diagonal uncertainty calculation.

GOSIA calculations run very quickly on modern hardware. As GOSIA was originally written in the early 1980s, many options described in the manual enable optimizations in order to speed up computation, but these are rarely necessary anymore.

Gosia Input File

Shown below is an example file. GOSIA is run using the command `gosia < input_file`. After the input file is a description of each line of the input file. The line numbers on the left of the input file are for reference only, and are not part of the input file itself. After the input file, a line-by-line explanation will be given.

The input file listed below is configured to run the minimization step of GOSIA. From this input file, removing lines 122-125, from `OP,MAP` to `OP,EXIT`, and editing line 101 from 4 to 3, runs the corrections for finite angle range and target thickness. Copying lines 152-155 to line 123, just above `OP,MINI`, runs the diagonal uncertainty calculation, and copying lines 162-165 to line 123, just above `OP,MINI`, runs the correlated uncertainty calculation.

```
1  OP,FILE
2  22,3,1
3  Kr78.out
4  9,1,1
5  chico97.gdt
6  3,1,1
7  Kr78.yld
```

```
 8  4,3,1

 9  Kr78.cor

10  7,3,1

11  Kr78.map

12  2,3,1

13  Kr78.bst

14  15,3,1

15  Kr78.err

16  0,0,0

17  OP,TITL

18       Coulomb excitation of 78Kr by 208Pb targets

19  OP,GOSI

20  LEVE

21  1,1,0.0,0.

22  2,1,2.0,0.455

23  3,1,0.0,1.017

24  4,1,4.0,1.119

25  5,1,2.0,1.148

26  7,1,2.0,1.756

27  8,1,4.0,1.873

28  9,1,6.0,1.978

29  10,1,8.0,2.994

30  12,1,2.0,2.444
```

```
31  0,0,0,0

32  ME

33  2,0,0,0,0

34  1,2,0.832,0.6,1.0

35  1,5,0.165,0.1,0.3

36  1,7,0.045,0.01,0.1

37  2,2,-0.905,-4.0,+0.5

38  2,3,0.265,0.2,0.8

39  2,4,1.285,1.0,2.0

40  2,5,0.440,0.1,1.0

41  2,7,0.135,0.05,3.0

42  2,8,0.073,-0.5,1.0

43  3,7,0.560,0.01,1.0

44  4,4,-1.2,-4.0,+4.0

45  4,7,0.390,0.01,1.0

46  4,8,-0.6,-2,2

47  4,9,1.660,0.5,3.0

48  5,5,0.977,-2.0,4.0

49  5,7,0.218,-1.0,1.0

50  5,8,0.910,-4.0,4.0

51  7,7,1.541,-4.0,8.0

52  7,12,0.1,1,2

53  8,-8,-0.832,1,2
```

```
54  9,9,-0.821,-8.0,8.0

55  9,10,1.8,0.05,2.0

56  10,-10,-0.853,1,2

57  7,0,0,0,0

58  2,5,0.337,0.1,0.5

59  2,7,-0.144,-0.2,-0.02

60  5,7,0.023,-0.5,0.5

61  0,0,0,0,0

62  EXPT

63  4,36,78

64  -82,208,295,29,4,0,0,0,360,0,1

65  -82,208,295,44,4,0,0,0,360,0,2

66  -82,208,295,92,4,0,0,0,360,0,3

67  -82,208,295,145,4,0,0,0,360,0,4

68  CONT

69  PRT,0.

70  1,-1

71  2,0

72  4,-2

73  5,1

74  7,0

75  11,0

76  12,0
```

```
77  14,0

78  16,0

79  0,0

80  END,

81

82  OP,YIEL

83  0

84  15,2

85  0.10,0.12,0.15,0.18,0.22,0.26,0.32,0.38,0.46,

86  0.56,0.68,0.82,1.00,1.20,1.50

87  2

88  0.925,0.471,0.207,0.106,0.051,0.0281,0.0136,0.0076,

89  0.0041,0.0023,0.0013,0.0008,0.0005,0.0003,0.0003

90  7

91  0.129,0.078,0.043,0.027,0.016,0.010,0.0062,0.0041,

92  0.0026,0.0016,0.0011,0.0007,0.0005,0.0003,0.0003

93  1,-1,-1,-1

94  1

95  0

96  0

97  2,1

98  1

99  0.05
```

```
100  1
101  4 ! which file gets used as input for the yields
102  4 ,1.0
103  7 ,1 ,7 ,2 ,0.254 ,0.008
104  7 ,3 ,7 ,2 ,0.518 ,0.008
105  7 ,4 ,7 ,2 ,0.119 ,0.004
106  7 ,5 ,7 ,2 ,0.047 ,0.010
107  5 ,1.0
108  2, 31.2, 1.0
109  3, 13.0, 3.6
110  4, 3.63, 0.17
111  5, 4.8, 0.9
112  9, 0.94, 0.10
113  3 ,1.0
114  5 ,2 ,0.45 ,0.10
115  7 ,5 ,4.0 ,3.5
116  7 ,2 ,-1.32 ,0.55
117  4 ,1.0
118  2 ,9 ,10 ,1.80 ,0.15
119  2 ,5 ,8 ,0.91 ,0.06
120  2 ,4 ,8 ,-0.60 ,0.03
121  2 ,2 ,8 ,0.073 ,0.005
122  OP ,MAP
```

```
123  OP,MINI
124  2100, 1000, 0.000001, 0.000001, 1, 0, 0, 1, 0, 0.0001
125  OP,EXIT
126  OP,INTG
127  6,8,286,304,20,38
128  270,280,290,300,310,320
129  15,18,23,28,33,38,43,48
130  6,7,286,304,38,49
131  270,280,290,300,310,320
132  34,37,40,43,47,50,53
133  6,16,286,304,62,121
134  270,280,290,300,310,320
135  55,60,65,70,75,80,85,90,95,100,105,110,115,120,125,130
136  6,10,286,304,131,160
137  270,280,290,300,310,320
138  125,130,135,140,145,150,155,160,165,170
139  6
140  270,280,290,300,310,320
141  18,18,18,18,18,18
142  10,50
143  0
144  10,10
145  0
```

```
146  10 ,100

147  0

148  10 ,100

149  OP ,CORR

150  OP ,EXIT

151  ! Diagonal error minimization

152  OP ,RE ,A

153  OP ,ERRO

154  0 ,0 ,0 ,0 ,0 ,1000000000000

155  OP ,EXIT

156  ! Full error calculation (only important correlations)

157  OP ,RE ,A

158  OP ,ERRO

159  1 ,0 ,0 ,1 ,0 ,1000000000000

160  OP ,EXIT

161  ! Full error calculation (all correlations)

162  OP ,RE ,A

163  OP ,ERRO

164  1 ,0 ,0 ,1 ,1 ,1000000000000

165  OP ,EXIT
```

1-16. File listings. This section starts with `OP,FILE` and continues until it reaches a line with `0,0,0`. This section specifies the names of all input and output files. These entries are not necessary, but provide human-readable names for files, rather than the default

`fort.15` and similar. For a full description of all input and output files used by GOSIA, and their assigned numbers, please refer to the "File assignments" chapter of the GOSIA manual [36].

The first parameter is the number identifying which file is being given a name. That is, an identifier of 3 indicates the output that would be written to `fort.3`. These are referred to as "file number" and "tape number" in the GOSIA manual.

The second parameter is the current state of the file. 1 indicates that it is solely an input file. 2 indicates that the file does not currently exist, and is an output file. 3 indicates that the file may or may not exist, and can be used either as an input or an output file, according to the options given later in the file.

The third parameter will be 1 for all of the files listed. This indicates that it is formatted text input, not binary input.

For example, the first entry in this section, `22,3,1`, indicates that the tape 22 may be opened either as an input or an output, and should be read as formatted text input. The following line, `Kr78.out`, gives the name of the output file.

17-18. A title. Something human readable that will be printed to the output file.

19-81. The section containing setup for many different options describing the experiment and the structure of the nucleus being investigated. Each is described in more detail below.

20-31. The levels in the nucleus being analyzed. The starts with the `LEVE` option, and ends with a single line containing `0,0,0,0`.

Each line has four values. The first is an index which will be used to refer to the level from now on. The second is the parity, either +1 for positive or -1 for

104

negative. The third parameter is the spin. The fourth parameter is the energy of the state, in MeV.

32-61. The matrix elements present in the calculation. Each line can take a number of different forms. All uses of an integer to refer to a matrix element refer to the order they appear in this list, with the first element having index 1.

Each line has five values `A,B,C,D,E`.

If `B` is 0, then this line gives the multipolarity of the matrix elements to follow. `A` is the multipolarity, where values 1-6 correspond to E1-E6 transitions, 7 corresponds to M1, and 8 corresponds to M2. In the example, `2,0,1,0,0` indicates that the next set of matrix elements are E2 matrix elements. `7,0,0,0,0` indicates that the next set of matrix elements are M1 matrix elements.

If `B` is a positive value, indicates a free parameter in the fit. This is a matrix element connected states `A` and `B`. It has initial value `C`, and is allowed to vary from `D` to `E`.

`A,-B,C,D,E`, where there is a negative sign before `B`, indicates a matrix element that is present in the simulation, but has a value coupled to an earlier defined matrix element. That is, if the free parameter increases by 10%, then this parameter also increases by 10%. This helps to keep the dimensionality of the problem low. This matrix element connects states `A` and `B`. It has initial value `C`. It is coupled to the transition that connects states `D` and `E`.

If the value `E` is greater than 100, then it means that the matrix element is coupled to an element with a different multipolarity. The hundreds place of `E` indicates which multipolarity contains the independent matrix element is in. For

example, the line `1,-2, 0.5, 1, 203` would couple the (1,2) transition in the current section to the (1,3) E2 transition.

The line `0,0,0,0,0` indicates that all matrix elements have been input.

62-67. The experiment section. This describes some of the experimental details. The first line is the number of "experiments", Z of the nucleus of interest, then the A of the nucleus of interest. In GOSIA, "experiments" refers to the number of different angle bins being used.

Each experiment line contains 11 values, `A, B, C, D, E, F, G, H, I, J, K`. `-82, 208, 295, 29, 4, 0, 0, 0, 360, 0, 1` is an example line. `A,B` gives the charge and mass of the particle not being investigated. Here, `-82,208` specifies ^{208}Pb. The negative sign of `A` indicates that the nucleus of interest is the projectile. `C` is the mid-target kinetic energy of the projectile, in MeV. `D` is the central angle of the scattering angle region being used. `E,F` as `4,0` are the number of magnetic substates used in the full and approximate calculations. Giving `G` as `0` indicates that the particle detector is axially symmetric. `H,I` as `0,360` gives the azimuthal coverage of the particle detector in degrees. The value of `J` selects which scattering angle solution to use if the conversion from laboratory angles to center of mass angles allows for two solutions. Using `0` as `J` selects the backward angle, while using `1` selects the forward angle. Finally, the values of `K` gives an index of a normalization constant to be used, adjusting the absolute value of the fitted yields for this experiment. These normalization constants account for the absolute detector efficiency, target thickness, amount of beam on target.

68-79. The control block. The main element here is the `PRT` block, controlling which

106

parameters are written as output. This section is described in detail in the GOSIA manual [36].

80-81. The end of the `OP,GOSI` block. Two things of note here. First, the comma in `END,` is necessary. Second, the line after `END,` is not entirely blank, but must contain an empty space.

82-121. The `OP,YIEL` section contains additional experimental details, along with values measured from previous measurements. As there are many values in this section, each will be mentioned in detail.

83. Whether to use a correction for finite distance traveled by the excited nucleus before de-excitation. `0` indicates that this correction is disabled, and `1` indicates that this correction is disabled.

84-92. The internal conversion coefficients. These can be acquired from BrIcc [82] on NNDC. First, the number of points, and the number of multipolarities that will be present. In this case, 15 points will be entered, for 2 different multipolarities. On lines 85-86 are the x-values, in MeV, of the internal conversion coefficients. Line 87 identifies which multipolarity is to follow (E2), with its coefficients next. Similarly, line 90 identifies M1 as the next, with coefficients on lines 90-91.

93. The number of gamma ray detectors in each experiment. A negative sign indicates that it has the same parameters as the previous set. The line `1,-1,-1,-1` indicates that there is a single γ-ray integration region being used for all four scattering angle regions, and they all of the same parameters.

94-96. Number of detectors, theta angles, and phi angles. The experimental yields given here to GOSIA treat the SeGA array as a single integration region. The abso-

107

lute coverage does not matter, as the total efficiency is included in an overall normalization constant used by GOSIA.

97. Which transition is used for normalization between different experiments when displaying predicted yields. Here 2,1 is given as the normalizing transition, indicating that the $2_1^+ \rightarrow 0_1^+$ transition in ^{78}Kr should be be normalized to 1. This option is only applicable when predicting experimental yields using the OP,POIN option, which is not used in this example.

98. Number of data sets for each experiment. This experiment has one γ-ray integration region, so this is 1.

99. Upper limit for intensity of unobserved γ-ray yields. Any transitions that are above this threshold, but not reported, will be warned about. This value is relative to the intensity of the normalizing transition, given on line 97.

100. Relative normalization constant for γ-ray yields detected in each γ-ray integration regions of a single experiment. Since this analysis used only a single γ-ray summing region, no changes to the normalization constants are needed, and so the value 1 is given.

101. The input file to be used for reading in experimental γ-ray yields. This value will change frequently while performing a GOSIA calculation. While performing corrections for finite detector size and target thickness, this needs to be 3, indicating that the uncorrected yields are used as input. While performing any other calculation, this should be 4, indicating that the corrected yields are used as an input.

102-106. Branching ratios used as an input. First is the number of branching ratios to be

given, and the relative weight that they should be given in the fit. 6 numbers are given for each branching ratio, `A,B,C,D,E,F`, where `A`, `B`, `C`, and `D` are indices of states. This gives the branching ratio $\frac{A \to B}{C \to D}$ as $E \pm F$.

107-112. Lifetimes used as an input. First is the number of lifetimes to be given, and the relative weight that they should be given in the fit. 3 numbers are given for each lifetime, `A,B,C`. This gives the lifetime of state `A` as $B \pm C$ ps.

113-116. The mixing ratios between E2 and M1 transitions. Line 113 has the number of mixing ratios given, along with their weight in the fit. Each line has four values, `A,B,C,D`, which gives the δ mixing ratio from `A` to `B` as $C \pm D$.

117-121. Known matrix elements as input. Line 117 has the number of matrix elements given, along with their weight in the fit. Each line has five values, `A,B,C,D,E`, which specify that the matrix element with multipolarity `A` between states `B` and `C` is $D \pm E$. Values of `A` from 1-6 correspond to E1-E6 multipolarity, and values of 7 and 8 correspond to M1 and M2, respectively.

122. The `OP,MAP` command generates temporary files necessary for minimization and error calculation.

123-125. The command to perform the minimization, varying the matrix elements to best fit the data given. The values on line 124 mainly describe the convergence criteria. For example, the `1000` is the number of iterations to try before bailing out. The parameters here should be good for general use, and are described more fully in the manual.

The `OP,EXIT` command on line 125 causes GOSIA to exit before finishing the file. Running GOSIA occurs in several steps, each requiring edits to the input file. All GOSIA calculations require the same or similar input up to line 121, the end of the `OP,YIEL`

section, but have different requirements after that. Having the `OP,EXIT` command is the documented way to comment out part of the file by having GOSIA exit early.

126-150. Options to correct the gamma ray yields for finite target thickness and finite angular bin size. These depend on the matrix elements themselves, and so this must be re-run if matrix elements change significantly during. It depends only on the initial values, listed in the `ME` section. In order to correct based on the minimized values, the minimized values must be copied into the `ME` section.

When performing corrections lines 122-125 are removed, so that the `OP,MAP`, `OP,MINI` and `OP,EXIT` commands are not present.

127-138. There are three lines for each experiment. The first line is `A,B,C,D,E,F`. The energy in the target varies from `C` to `D`, with `A` spline points. The angular bin coverage for the experiment varies from `E` to `F`, with `B` points.

The second line is the `A` points used for interpolating the energy, and the third line is the `B` points used for interpolating the energy. Due to the interpolation method used, two points both above and below the endpoints of the region should be given.

139-142. The energy loss through the target, as a function of energy. The number of points is on the first line, with the incoming energy in MeV on the second, and the energy loss in MeV on the third line. The fourth line contains the number of angle and energy integration points to use.

143-148. Entries for experiments 2-4, in the same format as are in lines 139-142. Each consists of only two lines. The 0 on the first line indicates that the explicit

listing of energies and energy losses will be omitted, using the same values as were specified for the previous experiment.

149. `OP,CORR` indicates that the yields are to be corrected for finite target thickness and angular coverage. This outputs on file 4. File 4 is named `fort.4` by default, and can be renamed in the `OP,FILE` section described earlier. While performing corrections, line 101 must be equal to 3, so that GOSIA reads from the uncorrected yields.

152-155. Calculation of diagonal errors. This varies each parameter independently until the χ^2 increases. To use this, copy-paste this section above line 123, just above the `OP,MINI` section.

`OP,RE,A` releases the coupling of parameters, so that each parameter can be varied independently. `OP,ERRO` then performs the uncertainty calculation. Full description of the parameters to `OP,ERRO`, given on the following line, are in the GOSIA manual [36].

157-160. Calculation of correlated errors, using only the largest of the correlations. This option is rarely necessary, because the availability of modern processing power enables fast use of the complete calculation as described in lines 162-165. If this optimization is needed, the following steps can be performed.

1. The line `SEL,` is added to the `CONT` block. Make sure that you have `4,-2` in the `PRT` block. GOSIA is then run, performing the χ^2 minimization, and producing `fort.18` as a side effect.

2. The `SEL,` is then removed, and `OP,SELECT`, then `OP,EXIT` is added just above the `OP,MINI` line. GOSIA is run, which produces `fort.10` using `fort.18`. This file is

renamed to `fort.18`, overwriting what was there.

3. The `OP,SELECT` and `OP,EXIT` lines are then replaced with the contents of this section (lines 157-160), after which GOSIA is run a third time, which produces the correlated errors in the output file.

On a computer using an Intel Celeron Processor 2955U, this procedure reduced the calculation time from 6 sec to 3 sec, as compared to the next section. This optimization may be necessary for future analyses of Coulomb excitation experiments, but was not used in the present work.

162-165. Calculation of correlated errors, using correlations between all matrix elements. This section is active when copy-pasted above the `OP,MINI` command.

Gosia Yield File

Below is shown an example yield file. There is a section for each experiment. Within each experiment, the experimental yields for each transition observed are given, along with their uncertainty. In GOSIA, each "experiment" refers to the an different angle cut in the scattering angle of the projectile.

```
1   1   36   78   304.2   5   1.0

2   1   273900   8400

4   2   8470   420

5   2   1570   160

9   4   460   100

5   1   1030   150

2   1   36   78   304.2   6   1.0

2   1   171200   5300

3   2   610   120

4   2   15150   640

5   2   2170   190

9   4   630   150

5   1   1660   190

3   1   36   78   304.2   7   1.0

2   1   203100   6300

3   2   5960   730

4   2   50900   1900

5   2   11850   840
```

```
9   4   8080   960

5   1   7380   580

7   2   1570   300

4   1   36   78   304.2   7   1.0

2   1   12910   550

3   2   1170   160

4   2   3600   270

5   2   1270   190

9   4   1470   250

5   1   700   220

7   2   330   180
```

The first line in each section has 7 values, `A,B,C,D,E,F,G`. `A` is the number of the experiment, and should increment 1-N. These values must correspond with the same experiment index in the main input file. `B` should be 1. `C` and `D` are the charge and mass of the nucleus of interest, respectively. `E` is the bombarding energy, in MeV. `F` is the number of γ rays to follow. `G` is the weighting factor for the experiment, usually 1.0.

After the header line, there will be `F` lines, each for a single γ ray observed. Each line consists of four values, `A,B,C,D`. This indicates that the transition from state `A` to state `B` has $C \pm D$ counts.

This file must be attached as file 3 when running GOSIA. By default, file 3 is named `fort.3`, but a different filename can be specified in the `OP,FILE` section of the input file.

Gosia Output File

During each stage of running GOSIA, the relevant information for that step will be saved to file. By default, this is saved as `fort.22`. However, it can be renamed to something more descriptive by editing the appropriate line in the `OP,FILE` section of the input file, as described in App. B. These output files are fairly self-explanatory, with human-readable output.

Shown below is a portion of the output file when running the correlated uncertainties, created during the analysis of the SeGA-JANUS commissioning run. First are shown the matrix elements, in units of eb. The `INDEX` column gives the index of the matrix element, in the order that they are listed in the input file, as described in App. B. The `NI` and `NF` columns list the initial and final state indices, in the order in which they appear in the input file.

```
                        OVERALL

                    ESTIMATED ERRORS


  INDEX       NI       NF       ME AND ERRORS



     1         1        2         0.81441  ( -0.01172 ,   0.01392)

         ......   -1.4  ,      1.7 PC

     2         1        5         0.15940  ( -0.00467 ,   0.00463)

         ......   -2.9  ,      2.9 PC

     3         1        7         0.03845  ( -0.00073 ,   0.00067)
```

115

```
          ......    -1.9 ,     1.7 PC
  4       2       2       -0.95705 ( -0.46895 ,  0.10638)

          ......    -49.0 ,    11.1 PC
  5       2       3        0.24314 ( -0.00726 ,  0.01616)

          ......    -3.0 ,     6.6 PC
  6       2       4        1.30478 ( -0.02092 ,  0.02073)

          ......    -1.6 ,     1.6 PC
  7       2       5        0.42944 ( -0.03488 ,  0.01622)

          ......    -8.1 ,     3.8 PC
  8       2       7        0.08398 ( -0.00502 ,  0.00406)

          ......    -6.0 ,     4.8 PC
  9       2       8        0.07362 ( -0.00557 ,  0.00520)

          ......    -7.6 ,     7.1 PC
 10       3       7        0.47660 ( -0.00972 ,  0.00776)

          ......    -2.0 ,     1.6 PC
 11       4       4       -1.20537 ( -0.96916 ,  2.40116)

          ......   -80.4 ,   199.2 PC
 12       4       7        0.33050 ( -0.00622 ,  0.00631)

          ......    -1.9 ,     1.9 PC
 13       4       8       -0.60618 ( -0.03198 ,  0.02861)

          ......    -5.3 ,     4.7 PC
 14       4       9        1.63204 ( -0.07236 ,  0.07143)

          ......    -4.4 ,     4.4 PC
```

```
15      5       5       0.97168 ( -0.72857 ,  0.26494)

...... -75.0 ,    27.3 PC

16      5       7       0.15204 ( -0.37226 ,  0.02178)

...... -244.8 ,    14.3 PC

17      5       8       0.89297 ( -0.07003 ,  0.04637)

......   -7.8 ,     5.2 PC

18      7       7       1.56100 ( -0.53161 ,  1.80646)

...... -34.1 ,   115.7 PC

19      7      12       1.00000 ( -1.95478 ,  0.97488)

...... -195.5 ,    97.5 PC

20      8       8      -0.81441 ( -0.17921 ,  0.43589)

...... -22.0 ,    53.5 PC

21      9       9      -0.81893 ( -1.33887 ,  2.17384)

...... -163.5 ,   265.4 PC

22      9      10       1.75631 ( -0.29264 ,  0.09578)

...... -16.7 ,     5.5 PC

23     10      10      -0.83497 ( -0.17111 ,  1.43445)

...... -20.5 ,   171.8 PC

24      2       5       0.33257 ( -0.01803 ,  0.01799)

......   -5.4 ,     5.4 PC

25      2       7      -0.14939 ( -0.00205 ,  0.00267)

......   -1.4 ,     1.8 PC

26      5       7       0.08830 ( -0.02221 ,  0.01760)
```

```
......   -25.2 ,   19.9 PC
```

Also included in this output are shown the matrix elements converted to $B(E\lambda)$, $B(M\lambda)$, or to the quadrupole moment, depending on what is appropriate for the matrix element being displayed.

```
                                OVERALL

                            ESTIMATED ERRORS


   INDEX      NI      NF      B(E,ML)(OR QUADRUPOLE MOMENT) AND

      ERRORS



     1        2       1          0.13265  (   -0.00379 ,

        0.00457)

     2        5       1          0.00508  (   -0.00029 ,

        0.00030)

     3        7       1          0.00030  (   -0.00001 ,

        0.00001)

     4        2       2         -0.72538  (   -0.35544 ,

        0.08063)

     5        3       2          0.05912  (   -0.00348 ,

        0.00812)

     6        4       2          0.18916  (   -0.00602 ,

        0.00606)
```

7	5	2	0.03688	(	-0.00575	,
					0.00284)	
8	7	2	0.00141	(	-0.00016	,
					0.00014)	
9	8	2	0.00060	(	-0.00009	,
					0.00009)	
10	7	3	0.04543	(	-0.00183	,
					0.00149)	
11	4	4	-0.90897	(	-0.73084	,
					1.81071)	
12	7	4	0.02185	(	-0.00081	,
					0.00084)	
13	8	4	0.04083	(	0.00442	,
					0.00442)	
14	9	4	0.20489	(	-0.01777	,
					0.01833)	
15	5	5	0.73647	(	-0.55221	,
					0.20081)	
16	7	5	0.00462	(	-0.00462	,
					0.00508)	
17	8	5	0.08860	(	-0.01335	,
					0.00944)	
18	7	7	1.18314	(	-0.40293	,

1.36917)

19	12	7	0.20000	(	-0.20000	,

0.58003)

20	8	8	-0.61415	(	-0.13514	,

0.32870)

21	9	9	-0.57095	(	-0.93346	,

1.51559)

22	10	9	0.18145	(	-0.05543	,

0.02033)

23	10	10	-0.53788	(	-0.11023	,

0.92407)

24	5	2	0.02212	(	-0.00233	,

0.00246)

25	7	2	0.00446	(	0.00012	,

0.00012)

26	7	5	0.00156	(	-0.00069	,

0.00068)

The extracted matrix elements are discussed in detail in Ch. 4.

Appendix C

Spectroscopy of Neutron-Rich Sulfur Isotopes

In addition to my work with SeGA and JANUS, and in preparation for possible future work on ^{44}S with the SeGA-JANUS setup, I also analyzed and published experimental data from GRETINA and the S800 spectrograph, performing γ-ray spectroscopy of $^{38-42}$S. Results of this work have already motivated follow-up research on the even-even sulfur isotopes, with a proposal accepted to perform intermediate-energy Coulomb excitation of ^{38,40,42,43,44}S at the NSCL (part of the PhD thesis of B. Longfellow).

The material as follows has previously been published in Ref. [83], ©2016 American Physical Society, used with permission.

Abstract

The low-energy excitation level schemes of the neutron-rich $^{38-42}$S isotopes are investigated via in-beam γ-ray spectroscopy following the fragmentation of ^{48}Ca and ^{46}Ar projectiles on a ^{12}C target at intermediate beam energies. Information on $\gamma\gamma$ coincidences complemented by comparisons to shell-model calculations were used to construct level schemes for these neutron-rich nuclei. The experimental data are discussed in the context of large-scale shell-model calculations with the SDPF-MU effective interaction in the sd-pf shell. For the

even-mass S isotopes, the evolution of the yrast sequence is explored as well as a peculiar change in decay pattern of the second 2^+ states at $N = 26$. For the odd-mass ^{41}S, a level scheme is presented that seems complete below 2.2 MeV and consistent with the predictions by the SDPF-MU shell-model Hamiltonian; this is a remarkable benchmark given the rapid shell and shape evolution at play in the S isotopes as the broken-down $N = 28$ magic number is approached. Furthermore, the population of excited final states in projectile fragmentation is discussed.

Introduction

Neutron-rich $N = 28$ isotones – comprising ^{48}Ca, ^{46}Ar, ^{44}S, and ^{42}Si – have provided much insight into the changes of the structure of nuclei encountered in the regime of large isospin. Evidence for a breakdown of the traditional $N = 28$ magic number resulted from the pioneering observation of low-lying quadrupole collectivity in ^{44}S [71, 72] and fueled the field of rare-isotope science in the quest to unravel the origin of shell and shape evolution in exotic nuclei with experimental programs worldwide.

The structure of the neutron-rich sulfur isotopes displays a variety of phenomena that are closely tied to shell evolution in exotic nuclei [84], with shape [77, 78, 79] and configuration coexistence [73, 74, 75] driving the properties of ^{44}S ($N = 28$) at low excitation energy. It is interesting to explore the evolution of the low-lying states as $N = 28$ is approached. It was pointed out by Utsuno $et\ al.$ [84] that tensor-driven shell evolution plays a critical role in the rapid shape transitions that occur in the S and Si isotopic chains towards $N = 28$. These effects are included in the SDPF-MU effective shell-model interaction introduced in [84] and the resulting predictions for the ^{40,41,42}S level schemes will be tested in the present

work. The sulfur isotopes between $N = 20$ and $N = 28$ have been studied with a variety of experimental techniques [85, 86, 87, 88, 89, 90, 91, 92, 93, 94, 95], however, information on the level schemes even at low excitation energy is still scarce. Beyond $N = 28$, very few excited states have been reported in the S isotopic chain [96, 97].

Gamma-ray spectroscopy following, for example, β decay [94], intermediate-energy Coulomb excitation [90], multinucleon transfer reactions [95, 93, 86], and projectile fragmentation [91, 92] provided a first, limited glimpse of the level structure of the neutron-rich S isotopes approaching $N = 28$ [98]. Here, we report on the in-beam γ-ray spectroscopy of $^{38-42}$S following the fragmentation of ^{46}Ar and ^{48}Ca intermediate-energy projectile beams on a C target in the center of the GRETINA γ-ray spectrometer [99]. Complementing the comparisons by Wang *et al.* [93] of S level schemes to shell-model calculations with the SDPF-U effective interaction [100], we compare our measurements with similar calculations based on the SDPF-MU Hamiltonian, which was constructed to describe the shell and shape evolution in the S and Si isotopic chains as $N = 28$ is approached [84].

Experiment

The measurements were performed at the Coupled Cyclotron Facility at the National Superconducting Cyclotron Laboratory [33] at Michigan State University.

The ^{46}Ar projectile beam was produced from a ^{48}Ca primary beam impinging upon a 1363 mg/cm^2 ^{9}Be production target and separated with a 240 mg/cm^2 Al degrader in the A1900 fragment separator [101]. The same production target was used to energy-degrade the ^{48}Ca primary beam in a separate setting. The total momentum acceptance of the separator was limited to $\Delta p/p = 0.25\%$ for both projectile beams. In two separate runs, the projectile

beams impinged upon a 149 mg/cm^2 glassy ^{12}C reaction target located at the pivot point of the S800 spectrograph [81]. The ^{46}Ar and ^{48}Ca beams had mid-target energies of 67.0 MeV/u and 66.7 MeV/u, respectively. The projectile-like reaction residues formed in the collision with the target were identified event-by-event with the focal-plane detection system of the S800 spectrograph and time-of-flight information involving plastic scintillators in the beam lines upstream of the reaction target. The magnetic rigidity of the S800 spectrograph was set to center the one-neutron pickup residues, ^{47}Ar [97] and ^{49}Ca [102], respectively. In the same settings, due to the large acceptance of the spectrograph, $^{40-43}$S and $^{38-40}$S, respectively, entered the S800 focal plane. The particle identification spectra correlating the energy loss of the reaction residues measured in the S800 ionization chamber and their time of flight are shown in Fig. C.1; the various S isotopes can be cleanly separated. The statistics for ^{43}S were not sufficient to construct a level scheme and thus will not be discussed here. Most transitions observed in ^{43}S can be associated with γ rays previously reported in Ref. [88].

The reaction target was surrounded by the Gamma Ray Energy Tracking In-beam Nuclear Array (GRETINA) [99], consisting of seven detector modules, each containing four high-purity, 36-fold segmented, Germanium crystals. The GRETINA detectors were arranged to cover forward angles, with four detector modules located at 58° and three at 90° with respect to the beam axis. The 3-dimensional coordinates of the γ-ray interaction points within the GRETINA crystals were determined from the signal decomposition of the digitized traces read out from each segment. The first interaction point, assumed to correspond to the coordinate with the largest energy deposition, was used to deduce the γ-ray emission angle that is used in the event-by-event Doppler reconstruction of the γ rays emitted by the reaction products in flight. The spectra shown in this work employ addback, a procedure recovering the γ-ray energy of events scattered from one crystal into a neighbor [103].
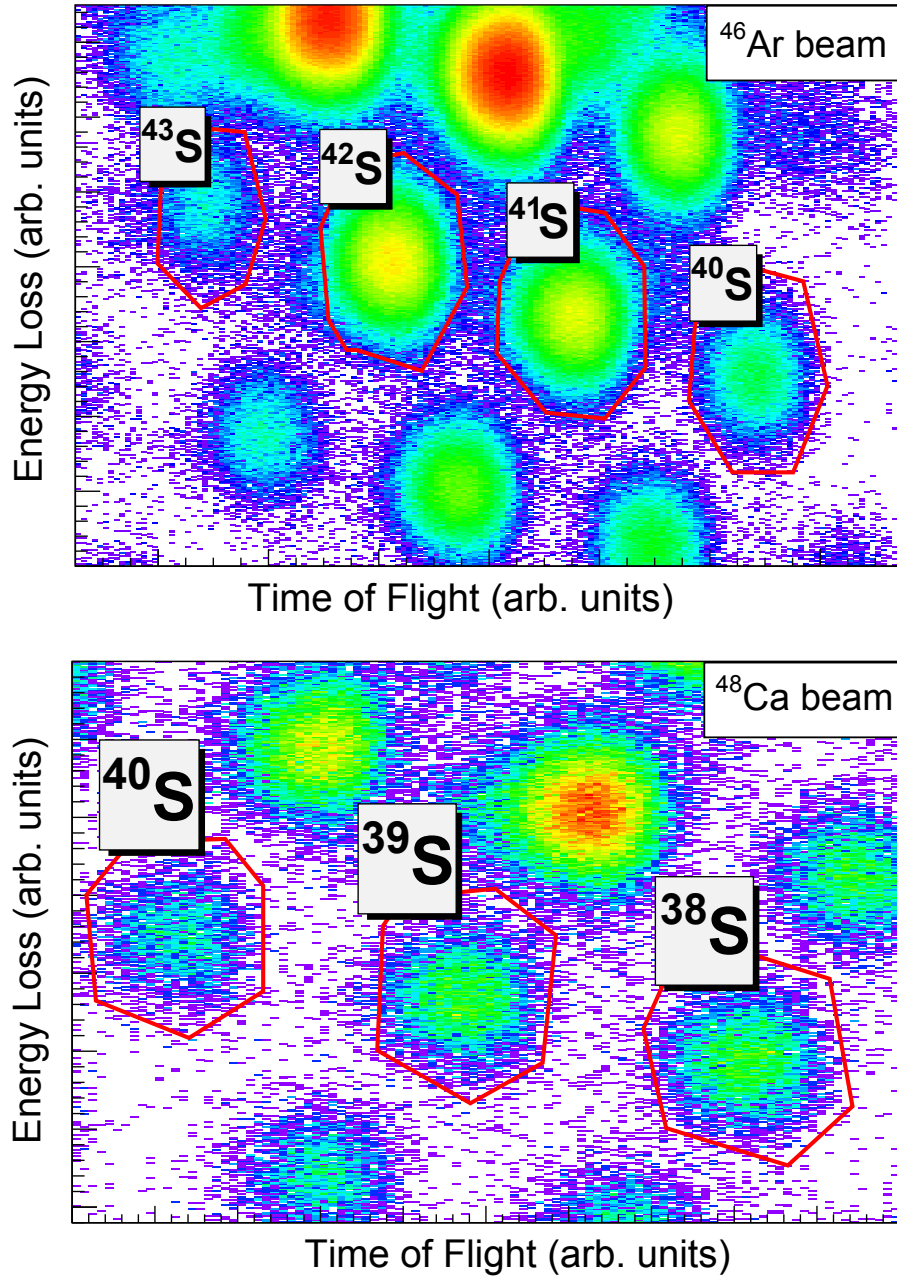
Figure C.1: Particle identification spectra for the reaction residues produced in $^{12}C(^{46}Ar,X)Y$ (upper panel) and $^{12}C(^{48}Ca,X)Y$ (lower panel). The energy loss was measured with the ionization chamber of the S800 focal plane. The time-of-flight was taken between plastic scintillators in the beam line and in the back of the S800 focal plane. The S isotopes of interest are unambiguously identified and separated.

In-beam detection efficiencies, taking into account the Lorentz boost, were determined with a GEANT4 simulation [104], with parameters adjusted to reproduce GRETINA's response to standard calibration sources at rest. These in-beam efficiencies were used to obtain the relative γ-ray intensities from recorded peak areas, as given in the tables in the next section. To determine $\gamma\gamma$ coincidence relationships for placement of transitions in level schemes, software cuts with appropriate background subtraction on γ-ray transitions in $\gamma\gamma$ coincidence matrices were used.

Results

In the following, we present our results for each isotope separately. The proposed level schemes are compared to large-scale shell-model calculations using the SDPF-MU [84] effective interaction for the sd-pf shell. The calculations adopted the full sd and fp model space for protons and neutrons, respectively, and used effective proton and neutron charges of $e_\pi = 1.35e$ and $e_\nu = 0.35e$ [84] and standard spin and orbital proton and neutron g factors. The calculations were carried out with the code NuShellX [105].

^{38}S

Figure C.2 shows the Doppler-reconstructed γ-ray spectrum taken in coincidence with ^{38}S reaction residues as produced in the fragmentation of the ^{48}Ca degraded primary beam. Several γ-ray transitions are present that will be discussed below.

We observe strong transitions at 1292(4), 1515(6), and 1534(5) keV that can be identified with the previously reported $2_1^+ \rightarrow 0_1^+$, $(2_2^+) \rightarrow 2_1^+$ and $4_1^+ \rightarrow 2_1^+$ transitions, respectively [106, 107, 95, 93, 108]. This is consistent with the coincidence spectra shown in
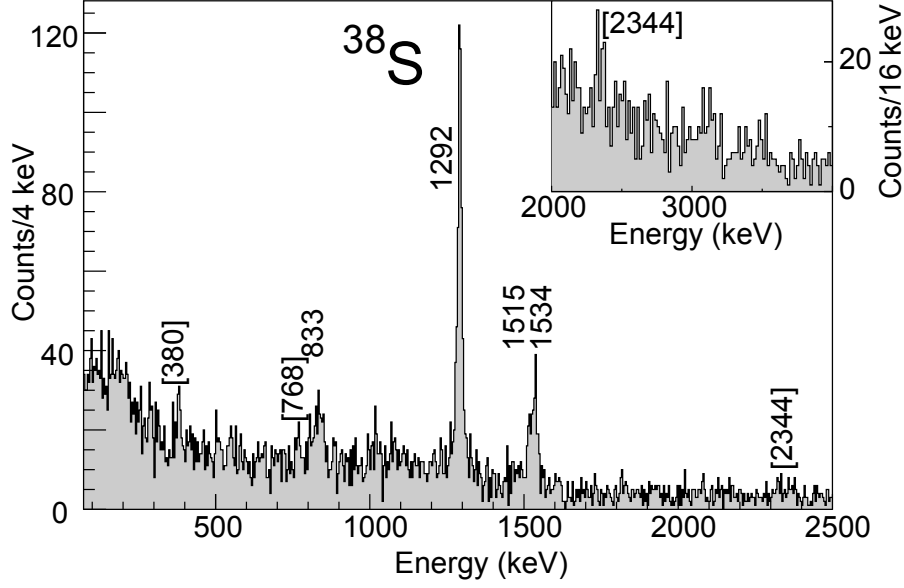
Figure C.2: Doppler-corrected ($v/c = 0.357$) γ-ray spectrum taken with GRETINA in coincidence with ^{38}S as identified with the S800 spectrograph. The inset expands the energy range from 2 to 4 MeV.

Fig. C.3, where the small number of counts observed agrees with expectations based on the statistics in the singles spectrum and the detection efficiencies at the respective energies. Within our limited statistics, the 1515/1534 keV doublet is coincident with the 1292 keV $2_1^+ \rightarrow 0_1^+$ transition. No coincidence relationships could be established for the new, weaker γ-ray transitions.

The 833(5) keV transition in our spectrum is 16 keV lower than the $(6_1^+) \rightarrow 4_1^+$ transition previously reported at 849 keV [95, 93]. Given the velocity of the S reaction residues, $v/c \sim 0.35$, and the C target thickness of 149 mg/cm^2, excited states with lifetimes of the order of several tens to hundreds of picoseconds will predominantly decay downstream of the target, signaled by a lowered peak energy and a left-tail in the Doppler-reconstructed γ-ray spectrum. The peak shape of the transition at 833 keV indeed seems to exhibit a left-tail in addition to the down shift in energy. GEANT simulations for different lifetime values reveal
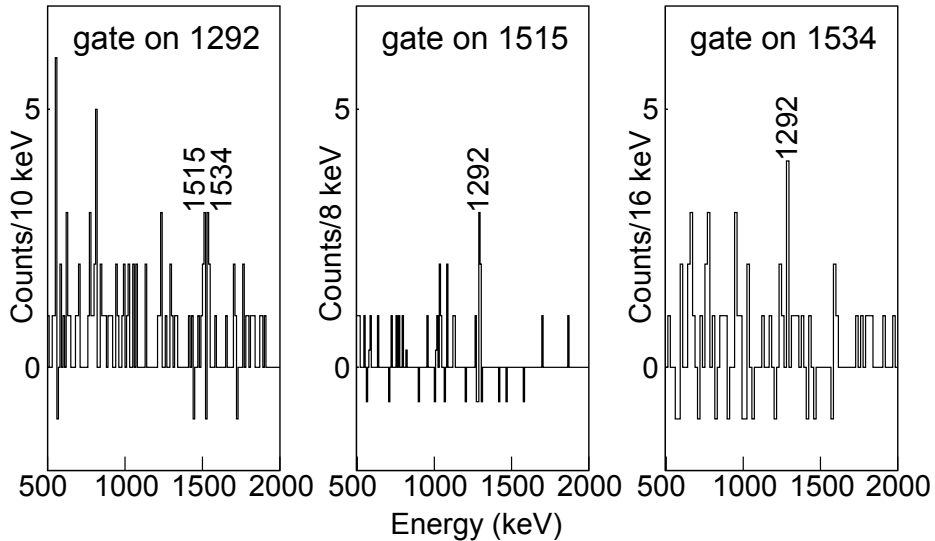
Figure C.3: Background-subtracted $\gamma\gamma$ coincidence spectra for ^{38}S. Coincidence spectra for the 1282, 1515, and 1534 keV transitions are shown. The small number of counts observed agrees with expectations based on the statistics of the measurement.

that the position and shape of the 833 keV transition is consistent with the emission of a 849 keV γ ray from a state that has a mean lifetime, τ, between 100 and 200 ps. Shell-model calculations with the SDPF-MU effective interaction, in fact, predict a lifetime for the 6_1^+ state of $\sim$40 ps, which is an order of magnitude longer than the lifetime of the 2_1^+ state [108] but a factor of about 4 shorter than our estimate[1]. The association of the 833 keV transition reported here with the known 849 keV $(6_1^+) \rightarrow 4_1^+$ transition is plausible but would benefit from more statistics for conclusive $\gamma\gamma$ coincidence and line-shape analyses.

Table C.1 lists the observed ^{38}S γ-ray energies together with their relative intensities and coincidence relationships. For the new weaker transitions reported here, coincidences could not be established due to low statistics.

Figure C.4 compares the ^{38}S level scheme with the SDPF-MU shell-model calculations.

---

[1]Using the measured transition energy instead of the one from the shell model only increases the lifetime to 54 ps at constant $B(E2)$ strength.

E_γ [keV]	Rel. Intensities (%)	Coinc.
[380(5)]	5(1)	
[768(5)]	7(1)	
833(5)	25(3)	
1292(4)	100(10)	1515, 1534
1515(6)	10(2)	1292
1534(5)	29(4)	1292
[2344(9)]	10(2)	

Table C.1: Energies, intensities and coincidence relationships for γ-ray decays observed in ^{38}S. The 833(5) keV peak is significantly below the literature value of 849 keV, and has a peak shape indicative of a left tail. In comparison to simulations, both may be explained by a lifetime of 100 ps $< \tau <$ 200 ps. Transition energies placed in brackets indicate tentative identifications of γ-ray peaks.

The experimental scheme only contains the previously known transitions since the new γ rays reported here are too weak to be placed in the level scheme based on coincidence relationships. The weak transition at 380 keV may correspond to the 383 keV transition visible in the ^{38}S spectrum of Wang $et\ al.$ [93]. In their work as well as here, this γ ray remains unplaced. We note that the association of the 2807 keV level with the 2_2^+ state from the shell model is supported by the decay branching ratio. It is predicted within the SDPF-MU shell-model calculations that the $2_2^+ \rightarrow 2_1^+$ transition is the dominant decay branch with an intensity exceeding 96% of the total yield out of the 2_2^+ state. No evidence for a 2807 keV transition has been reported in any of the previous γ-ray spectroscopy measurements that observed the 1515 keV transition [106, 95] and there is no evidence for such a transition in the present work (see Fig. C.2).

Consistent with previous studies, transitions from yrast states are the most prominent in the γ-ray spectra of reaction residues from secondary fragmentation reactions with several nucleons removed from the projectile [109]. In the following, we will continue to explore this population pattern and use it to argue possible level schemes for the more exotic S isotopes.
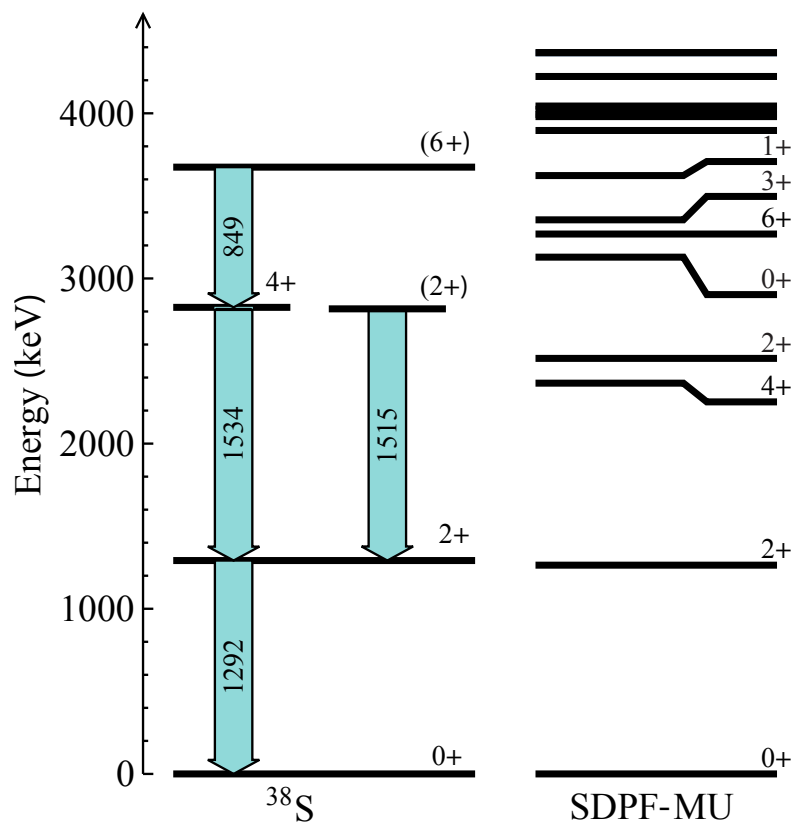
Figure C.4: Proposed experimental level schemes for ^{38}S based on previous data and coincidence relationships. The experimental level scheme is confronted with shell-model calculations using the SDPF-MU Hamiltonian.
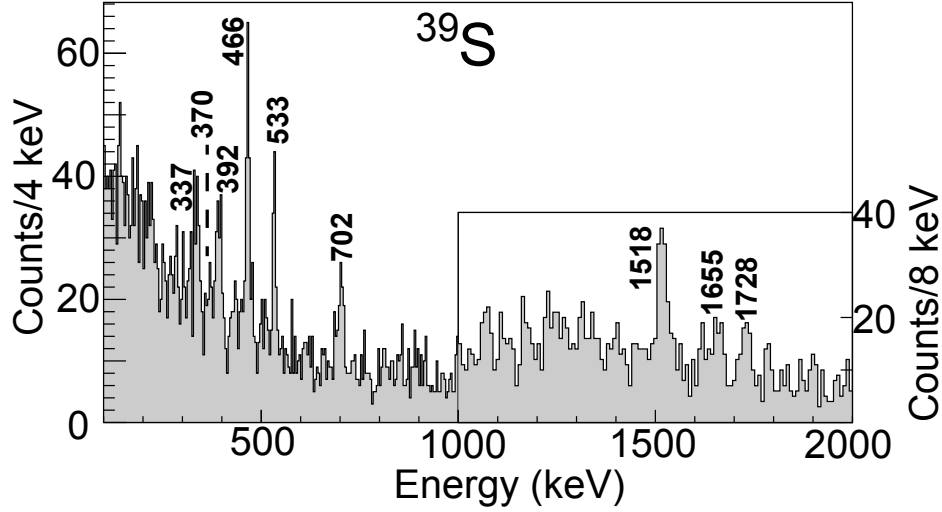
Figure C.5: Doppler-reconstructed γ-ray spectrum in coincidence with ^{39}S ($v/c = 0.348$). The inset expands the higher-energy region of the spectrum.

^{39}S

Figure C.5 shows the Doppler-reconstructed γ-ray spectrum taken in coincidence with ^{39}S reaction residues produced in the projectile fragmentation of ^{48}Ca. The transitions at 337(4), 392(6), 466(4), 702(4), 1518(4), 1655(6), 1728(5) keV have been reported before from mult-inucleon transfer reactions [93, 110], β decay of ^{39}P [111], and ^{40}P βn emission [94]. We identify the 392(6) keV line with the 398 keV transition reported in the references above

Coincidences of the 392, 337 and 466 keV transitions were reported from the β-decay work [94]. In our intensity and peak-to-background regime at low energies, weak evidence was seen only for the 337-466 keV coincidence (see Fig. C.6). The two new transitions reported in this work, at 370(6) keV and 533(4) keV, appear to be in coincidence, with the 370 keV transition feeding the state that decays by emitting a 533 keV γ ray, based on intensity arguments.

The transition energies, intensities, and coincidence relationships are summarized in Ta-

131
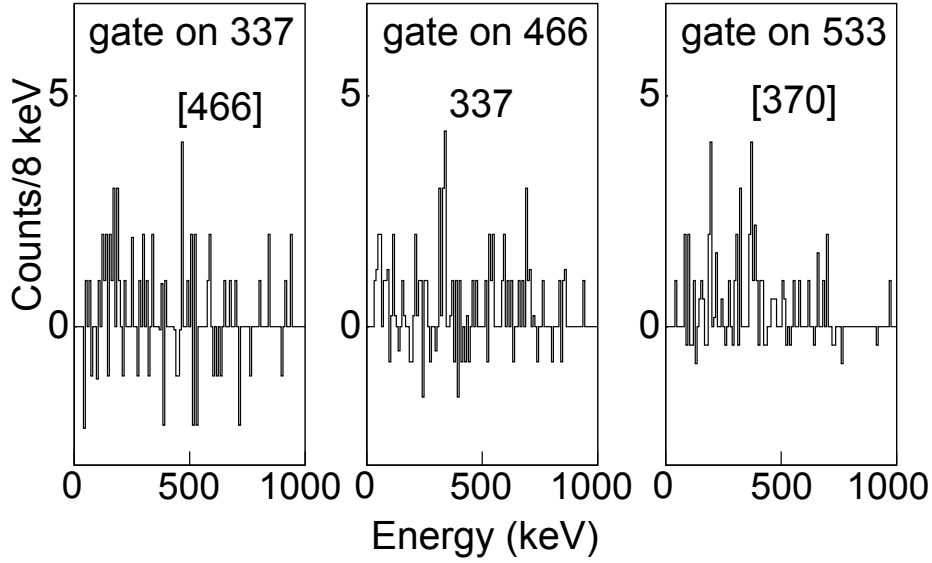
Figure C.6: Background-subtracted $\gamma\gamma$ coincidence spectra for ^{39}S. Software gates on the 337, 466, and 533 keV transitions are displayed. The coincidence spectra shown in the left and in the middle panel investigate the previously claimed 337-466 keV coincidence [94], which seems plausible based on our low-statistics data. The right panel provides weak evidence for a coincidence between the newly observed 533 and 370 keV transitions.

ble C.2. We confirm previously reported γ-ray transitions and add two news ones at 370 and 533 keV that appear to be in coincidence.

From the present data on ^{39}S, it is hardly possible to propose a firm level scheme – this is not just due to the lack of coincidences but also related to the expected structure at low energies. The difficulty becomes apparent from the predicted level scheme displayed in Fig. C.7. A triplet of states is expected within an energy range of $\sim$200 keV. Depending on the exact excitation energies, the two lowest-lying excited states may be nanosecond isomers, as predicted by the shell-model calculation. In-beam γ-ray spectroscopy at our beam velocities has limited sensitivity to nanosecond isomers. This makes it difficult to construct a level scheme since transitions or cascades can feed the ground state or any of the possible isomers.
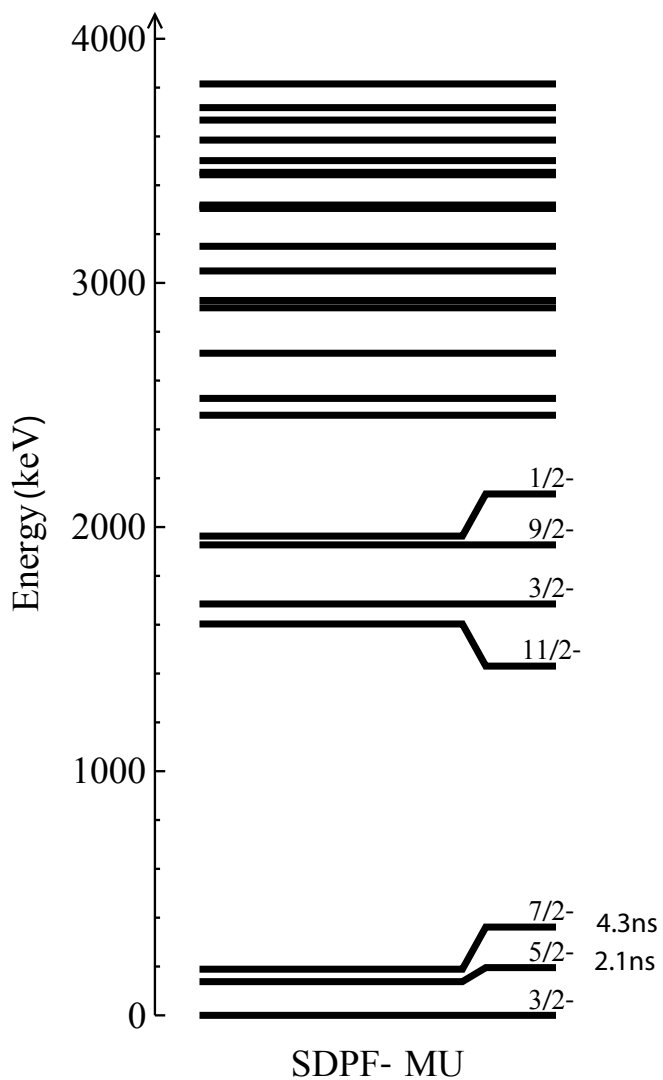
Figure C.7: Predicted level scheme and nanosecond lifetimes for ^{39}S from shell-model calculations using the SDPF-MU effective interaction.

E_γ [keV]	Rel. Intensities (%)	Coinc.
337(4)	28(5)	[466]
370(6)	9(3)	
392(6)	42(7)	
466(4)	71(10)	337
533(4)	38(7)	[370]
702(4)	42(8)	
1518(4)	100(15)	
1655(6)	59(11)	
1728(5)	43(9)	

Table C.2: Energies, intensities and coincidence relationships for γ-ray decays in ^{39}S.

Chapman *et al.* [110] propose a level scheme in comparison to shell-model calculations and $N = 23$ isotones, with 398- and 339-keV transitions depopulating the $(3/2_1^-)$ excited state to the $(7/2^-)$ ground state and the $(5/2_1^-)$ first-excited level at 59 keV. The $(3/2^-)$ is then suggested to be fed by the 466-keV decay of the first $(3/2^+)$ cross-shell excitation. While this is consistent with previously reported coincidence relationships, it would mean that, based on our intensities $I_\gamma(337) + I_\gamma(392) \approx I_\gamma(466)$, there is no room for any significant direct population or additional unobserved, discrete feeding of the $(3/2^-)$ level. The transitions reported here (Table C.2) are indeed indicative of positive-parity states, i.e. $3/2^+$ and $1/2^+$, located in the gap from 300 keV to 1600 keV that separates the first two groups of negative-parity states in ^{39}S (Fig. C.7). The higher-energy transitions are likely connecting the second group of negative-parity states expected between 1.6 and 2 MeV to the first group near the ground state. The observed energies of 1518, 1655 and 1728 keV fit this picture well. Certainly, a firm level scheme for ^{39}S requires a measurement with sufficient statistics for $\gamma\gamma$ coincidences, and sensitivity to low-energy γ-ray transitions and isomers.

^{40}S

Figure C.8 shows the Doppler-reconstructed γ-ray spectrum taken in coincidence with the ^{40}S reaction residues. ^{40}S was produced in the fragmentation of ^{48}Ca as well as from the ^{46}Ar projectile beam (see Fig. C.1). The two data sets were added for the purpose of γ-ray spectroscopy. Previous information on the spectroscopy of ^{40}S stems from intermediate-energy Coulomb excitation [71], fragmentation [92], ^{40}P β decay [94], and most recently multinucleon transfer [93].

Nine γ-ray transitions are apparent in our spectrum. Compared to the β-decay work, the only common transitions are at 902 and 1350 keV [94]. This complementarity in the population pattern can most likely be attributed to the suspected $(2^-, 3^-)$ ground state of the β-decay parent and the resulting selective population of final states in the decay daughter. This is in contrast to the observation that fragmentation reactions seem to populate low-lying yrast states the strongest. Other overlapping transitions with previous work are 891(13) keV from intermediate-energy Coulomb excitation [71], 909(5) and 1356(6) keV from projectile fragmentation [92], and 904, 1352, and 1572 keV from multinucleon transfer [93].

In addition, $\gamma\gamma$ coincidence relations could be established for several transitions, as shown in Fig. C.9. The coincidence spectra of the 902, 1350, and 1572 keV transitions show that they are mutually coincident, consistent with decaying to each other in a cascade. Weak evidence is visible in the spectrum gated on 1350 keV for a coincidence with the 2057 keV transition.

The observed transition energies, intensities and coincidence relations are listed in Table C.3. It is clear from the coincidence spectra in Fig. C.9 that the statistics in the 1572 keV line is just sufficient for a $\gamma\gamma$ coincidence analysis and, therefore, a placement of the weaker
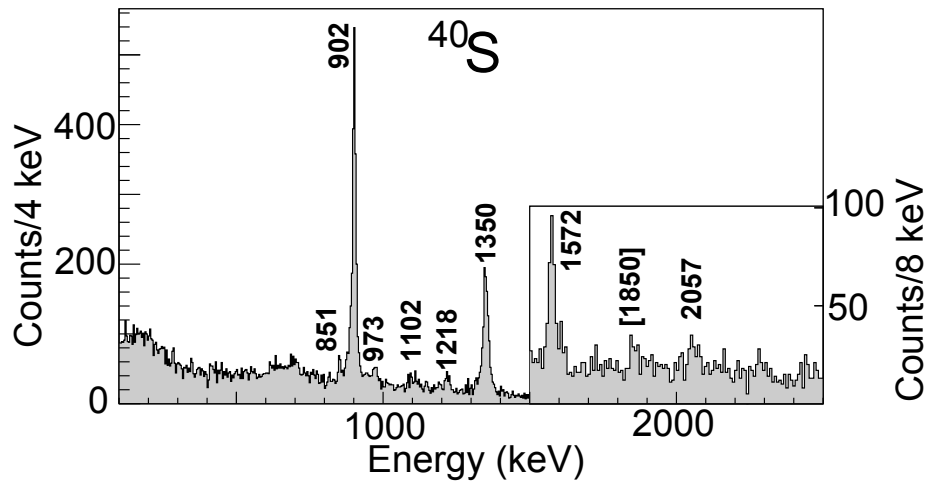
Figure C.8: Doppler-reconstructed γ-ray spectrum in coincidence with ^{40}S (with $v/c = 0.341$ for ^{40}S from ^{48}Ca beam and $v/c = 0.350$ for ^{40}S from ^{46}Ar beam).
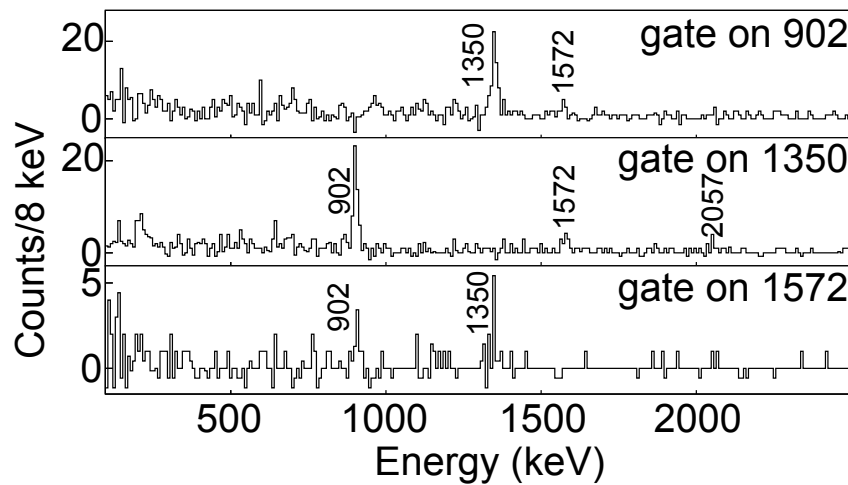
Figure C.9: Background-subtracted $\gamma\gamma$ coincidence spectra for ^{40}S. Spectra in coincidence with the strongest transitions at 902, 1350, and 1572 keV are shown.

E_γ [keV]	Rel. Intensity (%)	Coinc.
851(4)	5(1)	
902(4)	100(8)	1350, 1572
973(4)	5(1)	
1102(6)	9(1)	
1218(4)	7(1)	
1350(4)	76(6)	902, 1572, 2057
1572(4)	20(2)	902, 1350
[1850(5)]	4(1)	
2057(6)	8(1)	

Table C.3: Energies, efficiency-corrected relative intensities, and coincidence relations for γ-ray decays observed in ^{40}S. As for ^{38}S, the transitions suspected to form the even-spin yrast cascade are the most intense.

transitions reported here in the level scheme was not possible.

Figure C.10 shows the experimental level scheme proposed in this work. Based on the coincidences and the γ-ray intensities reported here, see Fig. C.9 and Table C.3, we propose the 1572 – 1350 – 902 keV cascade to correspond to the $(6_1^+) \to (4_1^+) \to 2_1^+ \to 0_1^+$ even-spin yrast sequence, consistent with Wang *et al.* [93]. Also, the 902, 1350 and 1572 keV transitions are the most intense in our spectrum, consistent with the population pattern reported in Section III.A for ^{38}S where the strongest transitions were the decays within the ground-state band up to the 6^+ state. The 2057 keV transition is placed tentatively as feeding the (4_1^+) state based on the spectrum in coincidence with the 1350 keV line.

We note that Winger *et al.* attribute the 1350 keV transition to the $(2_2^+) \to 2_1^+$ decay. This is at odds with our work and with the results from the multinucleon transfer [93] and the earlier projectile fragmentation measurement [92], where the 902 and 1350 keV transitions are attributed to the $2_1^+ \to 0_1^+$ and $(4_1^+) \to 2_1^+$ decays, respectively. We see no evidence for the 1013 keV γ ray that was tentatively proposed by Winger *et al.* to connect the yrast 4^+ and 2^+ states.

Shell-model calculations with the SDPF-MU effective interaction describe the even-spin
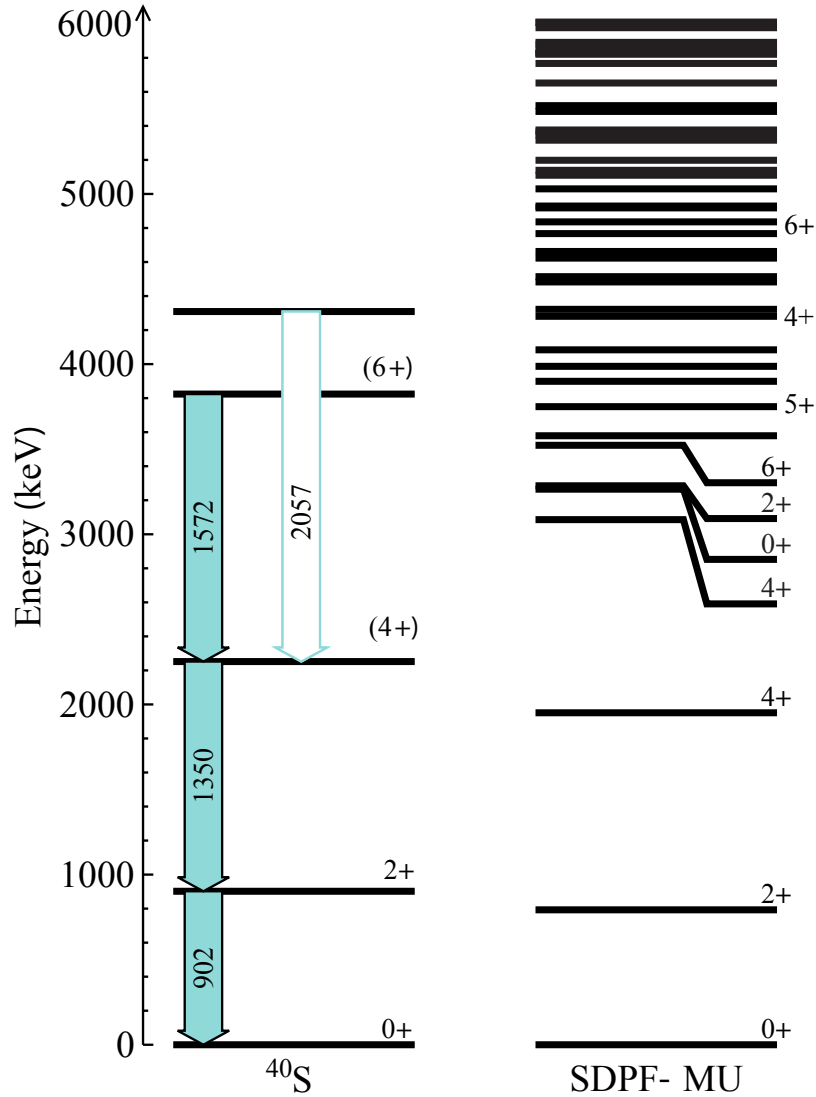
Figure C.10: Proposed experimental level scheme for ^{40}S compared to the SDPF-MU shell-model calculations. The level scheme is based on the $\gamma\gamma$ coincidence spectra and intensities. The tentative placement of the 2057 keV transition is indicated. The tentative identification of the low-lying even-spin yrast sequence is based on comparison with the shell model and the population pattern of excited states observed throughout this work.
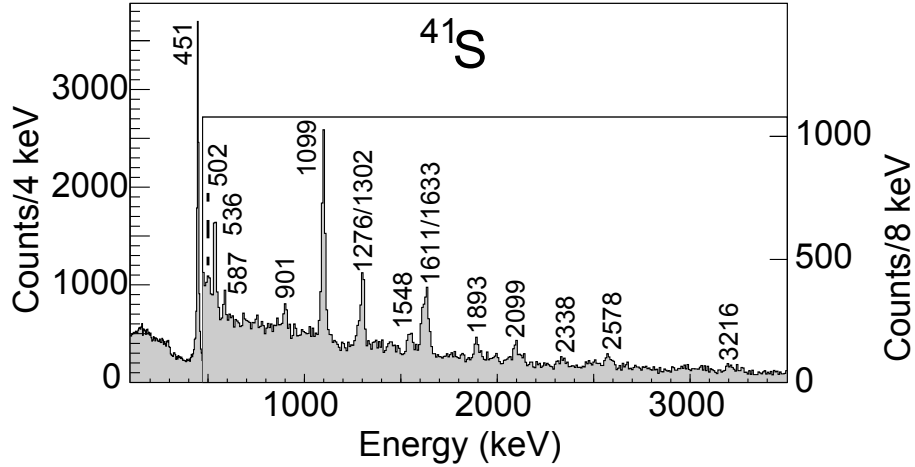
Figure C.11: Doppler-reconstructed γ-ray spectrum in coincidence with ^{41}S ($v/c = 0.342$). The spectrum is expanded with changed binning beyond 500 keV to highlight the high density of small peaks up to $\sim$3.2 MeV.

yrast sequence of ^{40}S well as shown in the comparison in Fig. C.10. The level density in ^{40}S is predicted to increase significantly at about 3 MeV. The many weak transitions not placed within the level scheme will originate from the multitude of states in this excitation energy region. Possible candidate states for the level established by the 2057 keV transition are higher-lying 4^+ or 6^+ states or the first 5^+ level (see Fig. C.10).

^{41}S

Figure C.11 shows the Doppler-reconstructed γ-ray spectrum taken in coincidence with ^{41}S reaction residues produced in the fragmentation of ^{46}Ar projectiles. Sixteen γ-ray transitions are visible in the complex spectrum. Of these, transitions that likely correspond to our 451, 902, and 1613 keV γ-ray transitions have been previously observed in intermediate-energy Coulomb excitation [90] (449 and 904 keV), in β decay from ^{41}P [111] (904, 1308 and 1613 keV) and in multinucleon transfer [86] (449 keV).

E_γ [keV]	Rel. Intensity (%)	Coinc.
451(4)	100(6)	536, 1099, 1633
502(4)	1.0(2)	
536(4)	8.8(8)	451, 1099
587(4)	2.5(2)	
901(4)	4.8(4)	
1099(4)	41(3)	451, 536
1276(4)	4.2(5)	
1302(4)	13.4(1.2)	
1548(4)	7.3(8)	
1611(4)	11.5(1.1)	
1633(4)	19(2)	451
1893(4)	7.4(8)	
2099(5)	6.4(7)	
2338(6)	5.0(6)	
2578(5)	6.0(7)	
3216(8)	6.7(8)	

Table C.4: Energies, efficiency-corrected relative γ-ray intensities, and coincidences for ^{41}S.

Our level of statistics allowed for a $\gamma\gamma$ coincidence analysis, as shown in Fig. C.12, with several conclusive relationships established. In a software gate on the 451 keV line, 536, 1099 and 1633 keV transitions are clearly visible. The 536 keV transition is in coincidence with both 451 and 1099 keV and a gate on 1099 keV returns the 451 and 536 keV lines. The 1633 keV transition is cleanly observed only in coincidence with 451 keV. We note that the peak structure at $\sim$1620 keV is a doublet of two peaks with centroids of 1611 and 1633 keV, where a software gate on the right peak, mainly 1633 keV, returns the 451 keV while a gate on the lower-energy side, narrowly on 1611 keV, does not (see Fig. C.13). Similarly, the 1302 keV transition is comparably intense and no coincidence is apparent, as shown in Fig. C.13. The transition energies, intensities, and coincidence relationships are summarized in Table C.4.

The proposed level scheme is shown in Fig. C.14. The placement of the transitions is based on $\gamma\gamma$ coincidences, energy sums, and intensities observed in the present work.
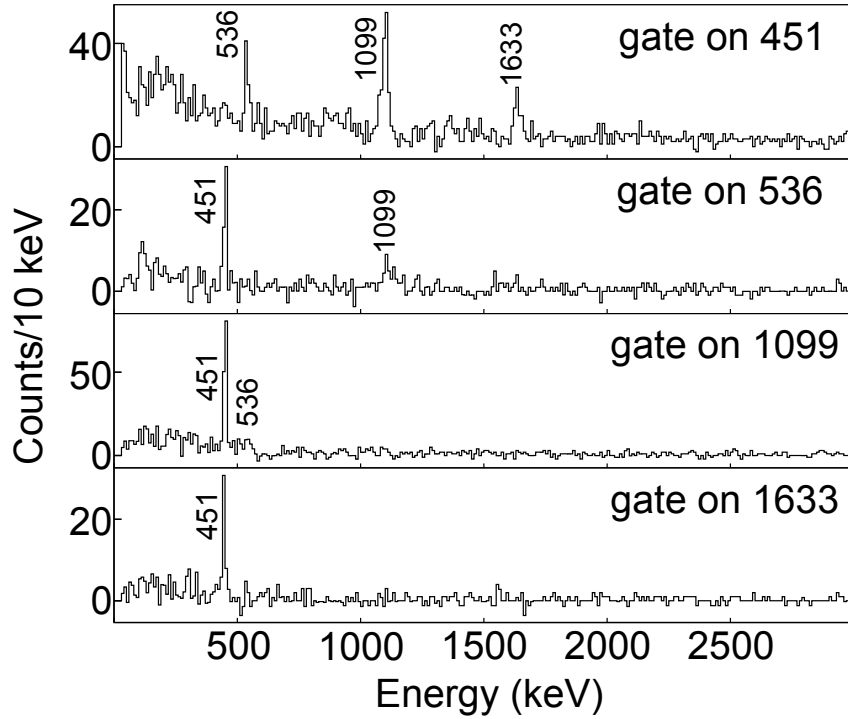
Figure C.12: Background-subtracted $\gamma\gamma$ coincidence spectra for ^{41}S. Spectra in coincidence with 451, 536, 1099, and 1633 keV are shown.
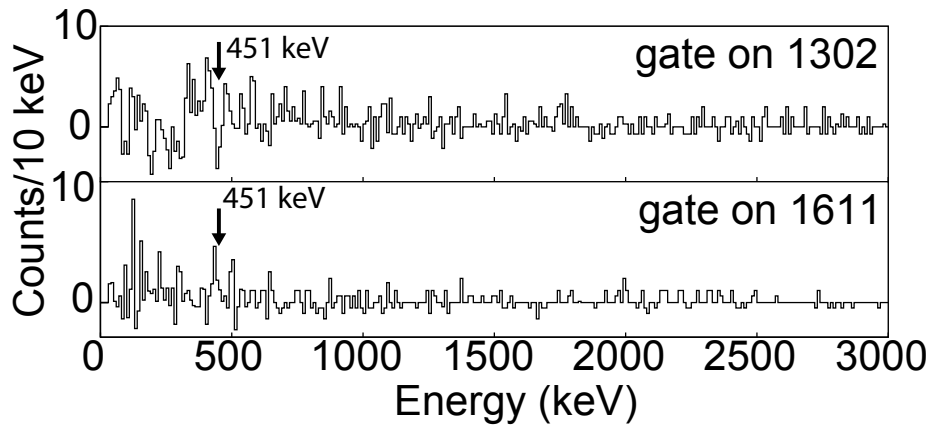
Figure C.13: Background-subtracted $\gamma\gamma$ coincidence spectra for ^{41}S. Spectra gated on 1611 and 1302 keV transitions in ^{41}S are shown. These transitions do not appear in coincidence with 451 keV (see also Fig. C.12) or any other transitions that they would feed.
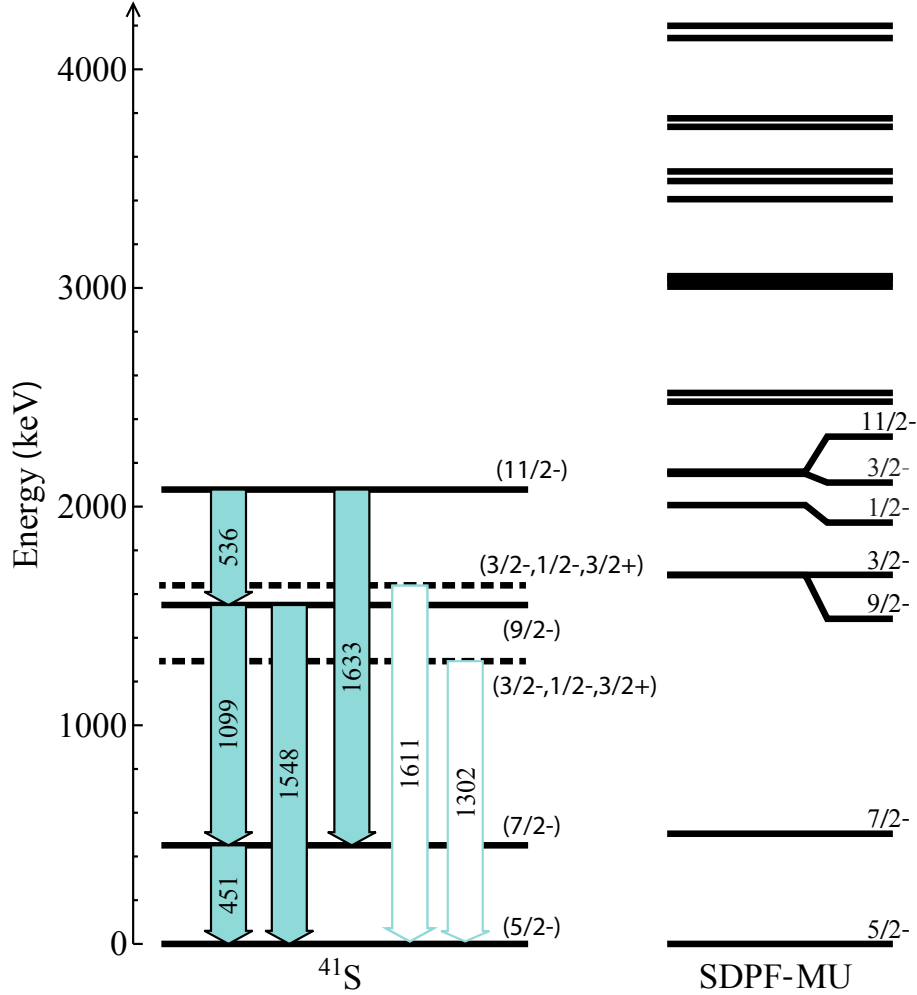
Figure C.14: Proposed experimental level schemes for ^{41}S based on the observed coincidences, intensities, energy sums and comparison to the shell model (SDPF-MU Hamiltonian). Solid lines and filled arrows indicate firm level and transition assignments, the dashed line and unfilled arrows indicate a tentative placement. Given that the 1611 and 1302 keV γ-ray transitions are strong and not in coincidence with 451 keV, we argue that they likely populate the ground state directly. Comparison to shell-model energies, decay branchings, and systematics was used to assign tentative J^π values (see text).

Based on comparison between shell-model calculations and observed decay patterns, spin-parities of $(5/2^-)$, $(7/2^-)$, $(9/2^-)$, $(3/2^-, 1/2^-, 3/2^+)$ and $(11/2^-)$ are tentatively assigned to the lowest-lying states in our experimental level scheme. These assignments provide reasonable matches of measured and calculated excitation energies, and in addition, are supported by comparison of the measured and calculated decay patterns. The $9/2^-$ state is predicted to have a branching ratio of 83% to the $7/2^-$ state and 17% to the $5/2^-$ ground state. As listed in Table C.4, the branching ratio for $(9/2^-)$ from our work is 85(2)% to the $(7/2^-)$ state and 15(2)% to the ground state. For the level that we tentatively identify as the $(11/2^-)$ state, the strongest decay leads to the $(7/2^-)$ state with 68(3)% of the total strength, and the remaining 32(3)% feeds the tentative $(9/2^-)$ state. The predicted branching ratios for these transitions are 69% and 31%, respectively, in good agreement with the data. Our $(3/2^-, 1/2^-, 3/2^+)$ assignments are based on the fact that the 1302 and 1611 keV γ rays are among the most intense transitions (see Table C.4) while not being in coincidence with 451 keV or other strong transitions. We propose that both decay to the ground state directly, forming excited states at 1302(4) and 1611(4) keV. Comparison to the SDPF-MU shell-model calculations reveal the $3/2_1^-$ and $1/2_1^-$ states as the closest in energy with transitions to the ground state exceeding 97% of all de-excitations. The previous β-decay work offers support for this proposition. Winger $et\ al.$ [111] report 1308 and 1614 keV γ rays that likely correspond to the 1302 and 1611 keV transitions observed in the present work. Our shell-model calculations with the SDPF-MU Hamiltonian suggest that the decay parent ^{41}P has a ground-state spin-parity of $1/2^+$ and a first excited $3/2^+$ state at 274 keV. Either of these possible J^π values for the ^{41}P ground state could populate the $1/2^-$ and $3/2^-$ states in ^{41}S, allowing their observation in [111]. If the $1/2^-$ and $3/2^-$ states were indeed at 1302 and 1611 keV, we would have observed all low-lying negative-parity states below 2.2 MeV

consistent with the systematics of excited states populated in fragmentation. However, positive parity-states, corresponding to neutron cross-shell excitations across $N = 20$ as discussed for the Si isotopic chain [112], may be found at low excitation energy as well. A $3/2^+$ level would be expected to decay to the $(5/2^-)$ ground state and would have been strongly populated in the β decay of the positive-parity ground state. Such a positive-parity state is expected from systematics, but is based on cross-shell excitations and is therefore outside of the shell-model space employed here.

We show the shell-model level scheme up to 4 MeV and it is clear that the multitude of weaker, unplaced γ-ray transitions likely depopulate the higher-lying states. It is noted that our level scheme disagrees with the scheme proposed by Wang *et al.* [86] based on a low-statistics γ-ray singles spectrum obtained in multinucleon transfer. Wang *et al.* suggest that the 904 keV γ-ray transition reported in intermediate-energy Coulomb excitation [90], although they did not observe it in their own work, corresponds to the decay of the $9/2^-$ state to the ground state. This contradicts the expected decay pattern for such a state that would predominantly decay to the $7/2^-$ state.

Since multistep processes are severely suppressed in intermediate-energy Coulomb excitation [12], the observed γ rays in the work by Ibbotson *et al.* [90] were attributed to the depopulation of states at 449 and 904 keV, respectively. Based on a particle-rotor approach, the ground state and the proposed 449 and 904 keV levels were assigned $7/2^-$, $5/2^-$ and $9/2^-$ quantum numbers, respectively [90]. $M1$ excitations are heavily suppressed in Coulomb excitation and, in the absence of parity change, only $E2$ excitations have to be considered. In intermediate-energy Coulomb excitation, the proportionality between the excitation cross section and the $B(E\lambda; J_{gs} \rightarrow J_f)$ transition strength depends on the multipolarity, λ, but not explicitly on the spin values [12]. Therefore, we will refer to the $E2$

144

excitation strengths deduced by Ibbotson *et al.* as $B(E2 \uparrow)$. Now, assuming the SDPF-MU shell-model spin and parity assignments, the $B(E2 \uparrow)_{449 \text{ keV}} = 167(65) \ e^2\text{fm}^4$ and $B(E2 \uparrow)_{904 \text{ keV}} = 232(56) \ e^2\text{fm}^4$ values from [90] have to be compared to $B(E2; 5/2^- \rightarrow 7/2^-) = 147 \ e^2\text{fm}^4$ and $B(E2; 5/2^- \rightarrow 9/2^-) = 59 \ e^2\text{fm}^4$, respectively. While the measured $B(E2)$ strength to the first excited state agrees well with the shell-model picture, all other calculated $B(E2)$ excitation strengths, including the one to the $9/2^-$ state, are expected to be smaller by a factor of 4 ($9/2_1^-$) or two orders of magnitude ($3/2_1^-$ and $1/2^-$) than what is reported for the $B(E2 \uparrow)_{904 \text{ keV}}$ value in [90]. While a very weak γ-ray transition at 902 keV is visible in our spectrum, it would be surprising if it corresponded to a low-lying state based on the population pattern of excited states in projectile fragmentation that we have observed so far. Ibbotson *et al.* explored the possibility of $E1$ excitations in their measurement and concluded that the measured cross sections would be beyond the recommended upper limits for $E1$ strength in the region but that this possibility of a parity-changing transition cannot be fully excluded [90].

Wang *et al.* further report a γ ray at 638 keV based on very low statistics and without coincidence data and assign it to connect the $11/2^-$ and the $7/2^-$ states. We see no evidence for a 638 keV transition in our ^{41}S spectrum.

The energies and γ-ray branching ratios of our level scheme agree with the shell-model calculation using the SDPF-MU effective interaction. The fact that we observe candidate states matching all calculated levels below 2.2 MeV is consistent with a picture where, with no discernible final-state selectivity, the lowest-lying states are the most prominent, likely populated directly in the reaction and fed indirectly through a multitude of higher-lying excited states that cascade toward the ground state.
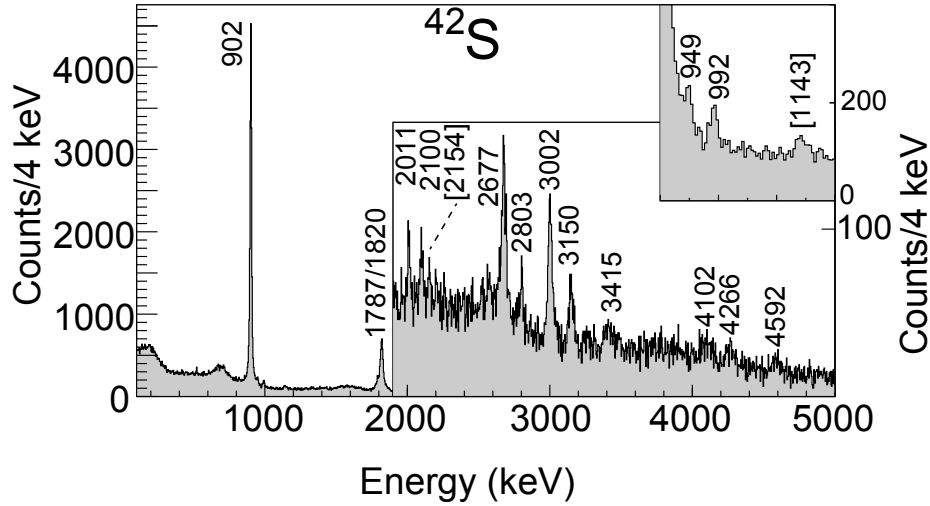
Figure C.15: Doppler-reconstructed γ-ray spectrum in coincidence with ^{42}S ($v/c = 0.335$). The insets expand energy regions of the spectrum with weaker intensity transitions. Transitions at 1143 and 2154 keV are tentative.

^{42}S

Figure C.15 shows the Doppler-reconstructed γ-ray spectrum taken in coincidence with ^{42}S reaction residues resulting from the fragmentation of ^{46}Ar. More than 15 γ-ray transitions are identified in the spectrum. Of these transitions, only the 902 keV and 1820 keV γ rays have been reported before, in intermediate-energy Coulomb excitation (890(15) keV) [71] and in the fragmentation of a ^{48}Ca primary beam (904 and 1821 keV) [92]. Two γ-ray transitions, at 1466(8) keV and 1875(9) keV, reported in [92] are not observed in the present work.

In addition, $\gamma\gamma$ coincidences were observed between several transitions, as shown in Figs. C.16 and C.17. First, the coincidence spectra for 902, 1787, and 1820 keV indicate that all three transitions are in coincidence with each other, forming a cascade that can be sorted by intensity. Furthermore, the 2100 keV transition is in coincidence with 902 keV
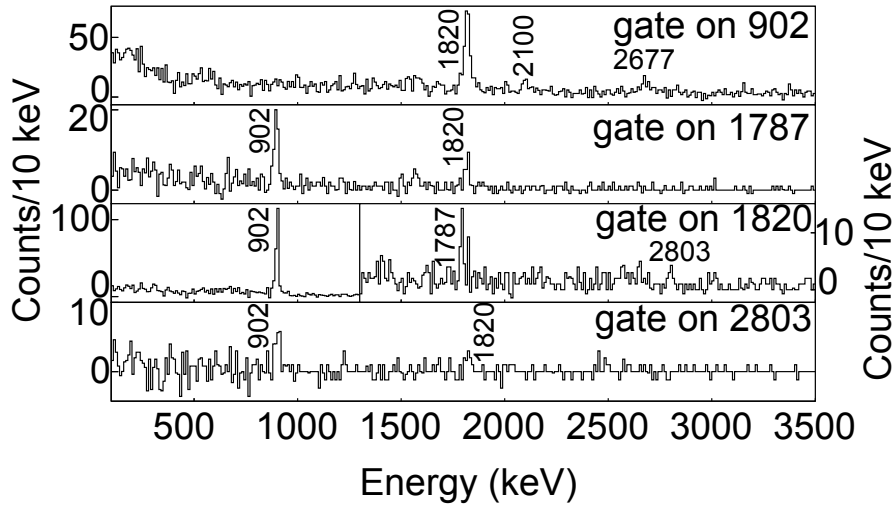
Figure C.16: Background-subtracted $\gamma\gamma$ coincidence spectra for ^{42}S. Spectra in coincidence with 902, 1787, 1820, and 2803 keV are shown.

and the 2803 keV γ-ray decay populates the state decaying by the 1820 keV transition.

An interesting structure emerges at high excitation energy. The background-subtracted coincidence spectrum for the weak 949 keV transition (see inset of Fig. C.15) shows the 992 and 2677 keV transitions. A gate on the 992 keV line returns 902, 949 and 2677 keV transitions and shows a 992 keV self-coincidence that may point to a doublet structure. In coincidence with 2677 keV, all three transitions, 902, 949, and 992 keV, are visible.

The γ-ray transition energies, intensities and coincidence relationships are listed in Table C.5.

Based on $\gamma\gamma$ coincidences, intensities and energy sums, the level scheme shown in Fig. C.18 is proposed. From the coincidence spectra of Fig. C.16 and the intensities listed in Table C.5 we propose the $1787 - 1820 - 902$ keV cascade to correspond to the even-spin yrast sequence $(6^+) \rightarrow (4^+) \rightarrow 2^+ \rightarrow 0^+$. This is in reasonable agreement with the shell-model calculation where the biggest deviation is observed for the 6^+ state with the calculation placing the
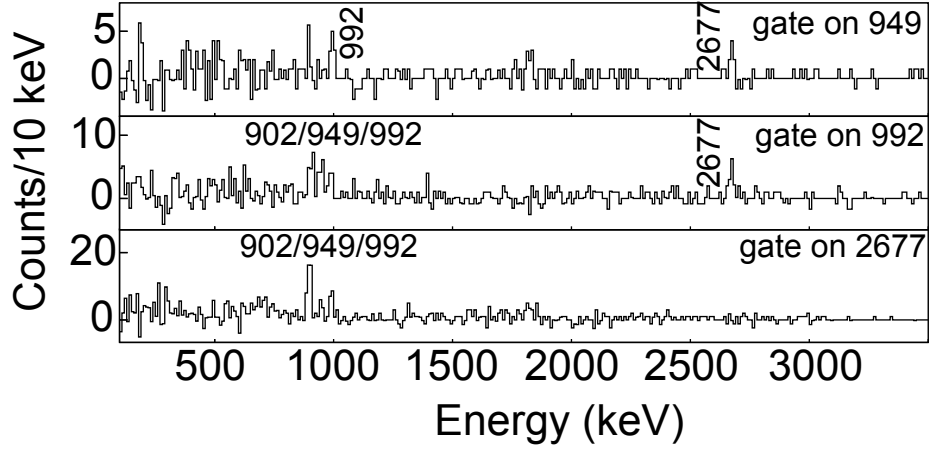
Figure C.17: Background-subtracted $\gamma\gamma$ coincidence spectra for ^{42}S. Spectra in coincidence with 949, 992, and 2677 keV are shown.

E_γ [keV]	Rel. Intensity (%)	Coinc.
902(4)	100(6)	1820, 2100, 2677
949(4)	1.2(1)	992, 2677
992(6)	2.2(2)	902, 949, 992, 2677
[1143(4)]	1.6(2)	
1787(4)	8.4(7)	902, 1820
1820(4)	33(2)	902, 1787
2011(4)	2.2(3)	
2100(4)	1.8(2)	
[2154(4)]	0.9(1)	
2677(4)	10.6(9)	902, 949, 992
2803(4)	1.7(2)	902, 1820
3002(4)	10.1(9)	
3150(4)	5.4(6)	
3415(9)	5.1(5)	
4102(8)	5.2(6)	
4266(7)	3.1(4)	
4592(7)	2.9(4)	

Table C.5: Energies, efficiency-corrected relative γ-ray intensities, and coincidences for ^{42}S. The 992 keV peak appears in coincidence with itself, suggesting that a doublet cannot be excluded for this transition.

state about 400 keV higher than the suggestion from experiment.

Placing the 2100 keV transition on top of the 2^+_1 state leads to a state at 3002(6) keV. In fact, we observe a 3002 keV γ-ray that then becomes a candidate to depopulate this new state directly to the ground state. We associate this state tentatively with the second 2^+ state of ^{42}S. The shell model predicts the 2^+_2 level at 3072 keV with a 84% branch to the ground state and the remaining 16% decaying to the 2^+_1 state. From our intensities in Table C.5 we obtain a decay branching of 85(2)% to the ground state and 15(2)% to the 2^+_1 level. We note that our assignment is at odds with the level scheme proposed by Sohler $et\ al.$ [92]. We do not observe the 1875 keV transition that is attributed in their work to depopulate the second 2^+ state to the first 2^+ state. Such a situation, where the $2^+_2 \rightarrow 0^+_1$ transition is not observed while the $2^+_2 \rightarrow 2^+_1$ is, would also be in contradiction to the shell-model calculations that have $2^+_2 \rightarrow 0^+_1$ as the strongest branch by a factor of five. We also observe no evidence for the 1466(8) keV γ-ray transition that establishes a 4245 keV state in ^{42}S in the work by Sohler $et\ al.$ [92].

The 2677 keV transition feeding the 2^+_1 state leads to a state at 3579(6) keV that, based on excitation energy alone, may be identified with the 3^+_1 state from the shell model or with a state from the group just above, comprising the 4^+_2, 3^+_2 and 0^+_2 states. From the decay pattern, however, the 3^+_1 and 4^+_2 levels are the only two with an essentially exclusive branch to the first 2^+ state. The 3^+_2 and 0^+_2 states are expected to exhibit significant decays to the second 2^+ state. A 3^- spin-parity assignment cannot be excluded and is outside of our shell-model configuration space.

From Fig. C.17 and the intensities of Table C.5, we construct a cascade 949 – 992 – 2677 keV on top of the 2^+_1 state. This leads to two new excited states, at 4571(7) keV and 5520(8) keV. The 2803 keV transition that was found in coincidence with the (4^+_1) state now

149
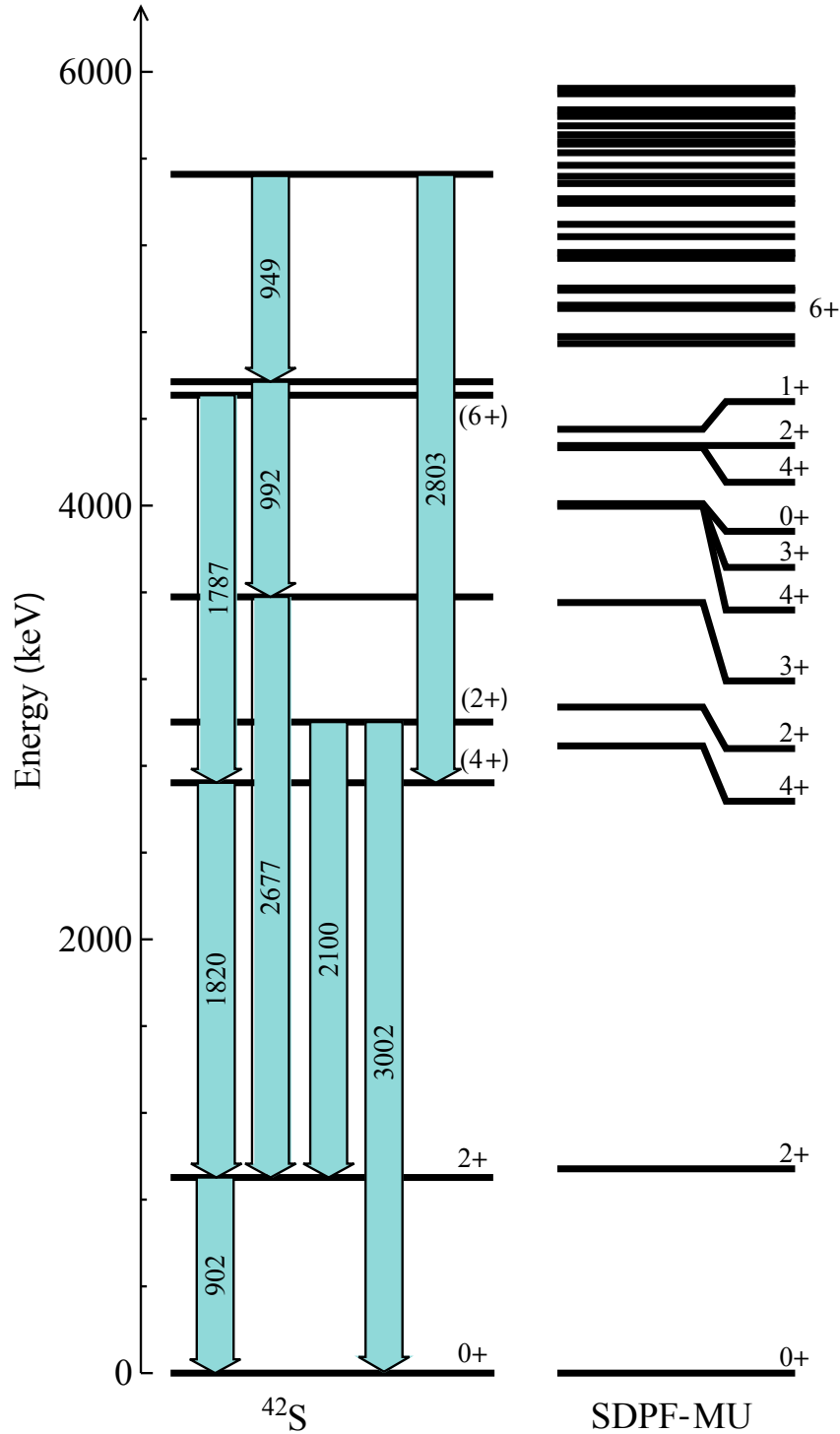
Figure C.18: Proposed experimental level scheme for ^{42}S based on the $\gamma\gamma$ coincidence spectra, intensities, and energy sums. The experimental data is confronted with shell-model calculations using the SDPF-MU effective interaction. Comparison to shell-model energies and decay branchings was used to assign tentative J^π quantum numbers (see text).

is a second branch of the new level at 5520 keV. Due to the high expected level density in this excitation energy region, it is not possible to associate this structure with states and decays of the SDPF-MU shell-model calculation. Many of the higher-lying 4^+ and 6^+ states, for example, show decay patterns broadly consistent with the high-lying structure in our level scheme.

Discussion

In Section III, we compare the ^{38,40,41,42}S level schemes from experiment to shell-model calculations with the SDPF-MU Hamiltonian. The motivation for choosing this shell-model effective interaction is rooted in its optimization to explain the complex structure of the $N = 28$ isotones ^{42}Si and ^{44}S, comprising phenomena such as shape and configuration coexistence, on a common footing [84]. Furthermore, SDPF-U level schemes are available in the literature for ^{39}S [110], ^{40}S [93], and ^{41}S [86]. In contrast to SDPF-MU, the SDPF-U effective interaction consists of two parts, one valid for $Z \leq 14$ and one applicable to $Z \geq 15$ [100]. Earlier work benchmarked the performance of SDPF-MU in the chain of Si leading up to $N = 28$ [112] and the present work extends this comparison to the S isotopic chain. Below, (i) the character of the quadrupole collectivity of the even-mass S isotopes is considered from $E(4^+)/E(2^+)$ and $E(6^+)/E(2^+)$ energy ratios, (ii) the transition into the $N = 28$ "island of inversion" is characterized by an analysis of the decay properties of the 2_2^+ state, (iii) the odd-mass S isotopes are discussed, and the emerging pattern for the population of excited states in fragmentation reactions is summarized.

For even-even nuclei, the ratios of yrast excitation energies have long been used to classify collectivity in terms of vibrational, rotational, and transitional character. The chain of S

isotopes, however, is challenging as shape and configuration coexistence is at play. We use $E(4_1^+)/E(2_1^+)$ and $E(6_1^+)/E(2_1^+)$ energy ratios to compare the ground-state bands of our proposed level schemes to the SDPF-MU shell-model calculations. Figure C.19 shows the comparison of these ratios for the even-mass sulfur isotopes with $N = 20 - 28$. Assuming the 6_1^+ energies proposed in this work, good agreement is reached for the measured and calculated $E(6_1^+)/E(2_1^+)$ ratios in ^{38,40,42}S. For ^{36,44}S, the 6_1^+ state has not been identified in the literature. The systematics, which are not solely based on comparison with the shell model but also the population pattern of excited states that has emerged in this work, lend support to our new tentative 6_1^+ assignments for ^{40,42}S. For the $E(4_1^+)/E(2_1^+)$ ratio, close agreement is observed for ^{40,42}S while measurement and theory are only within $\sim 25\%$ for the semi-magic ^{36}S and neighboring ^{38}S. It is noted that the shell-model calculation is not expected to work well for ^{36}S since the neutrons are restricted to the sd shell.

The case of ^{44}S is complex - a low-lying 4^+ state has been observed [73] that, based on two-proton knockout cross sections [73] and evidence for a long lifetime from a γ-ray line-shape analysis [73, 113], is suggested to correspond to a $K = 4$ isomer [73, 74]. This state differs in configuration from the 2_1^+ state, resulting in a strongly hindered $4_1^+ \rightarrow 2_1^+$ transition. The 4^+ level of ^{44}S that is connected to the collective 2_1^+ state [72] by a strong $E2$ decay has not yet been identified experimentally. With the intent of probing the collective nature of states with a similar underlying structure, we use the energies of the 4_2^+ shell-model state for ^{44}S since the corresponding cascade $6_1^+ \rightarrow 4_2^+ \rightarrow 2_1^+ \rightarrow 0_1^+$ is connected by the strongest $E2$ transitions. Using the 4_1^+ and 6_2^+ energies instead would not be noticeable in Fig. C.19 as the energies of the first and second 4^+ and 6^+ states differ only by 56 and 134 keV, respectively. Future experiments will put the predictive power of the SDPF-MU shell-model Hamiltonian to the test once the collective structures beyond the first 2^+ state
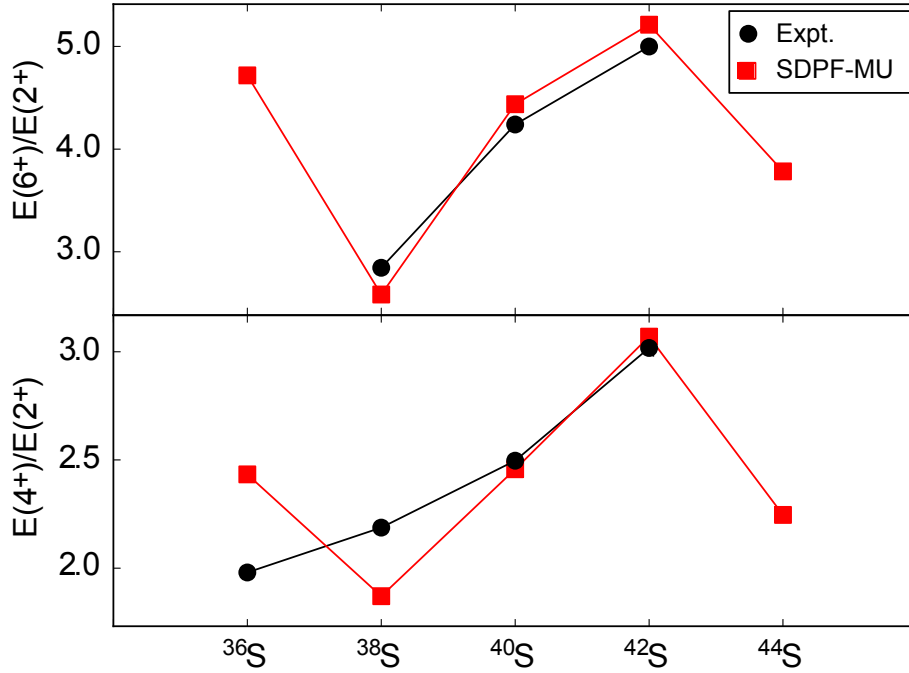
Figure C.19: Comparison of the excitation energy ratios of the first excited 2^+, 4^+, and 6^+ states across the neutron-rich sulfur isotopes. For ^{36}S, the 6_1^+ state has not yet been identified in the literature [98], and is expected at high excitation energy where the level density is significant. The collective 4^+ and 6^+ states of ^{44}S have not yet been observed either. For the calculated ^{44}S $E(4^+)/E(2^+)$ ratio, the shell-model energy of the second 4^+ state is used since the $6_1^+ \rightarrow 4_2^+ \rightarrow 2_1^+ \rightarrow 0_1^+$ cascade is connected by the strongest $E2$ transitions. However, the energy ratios would not change if the 4_1^+ or 6_2^+ energies were used instead since $E(6_2^+) - E(6_1^+) = 56$ keV and $E(4_2^+) - E(4_1^+) = 134$ keV. The tentative 6_1^+ assignments for ^{40,42}S stem from the measurements presented here.

are identified in the complex nucleus ^{44}S whose low-lying structure is sensitively determined by shape and configuration coexistence.

An interesting systematic trend emerges for the 2_2^+ states in the S isotopic chain. According to the shell-model calculations with the SDPF-MU Hamiltonian, the second 2^+ state in ^{42}S has a unique structure that is reflected in the $2_2^+ \rightarrow 0_1^+$ and $2_2^+ \rightarrow 2_1^+$ branching ratio. For ^{38}S and ^{40}S, the $2_2^+ \rightarrow 2_1^+$ transitions are predicted to dominate with 96.4% and 99.4%, respectively. For ^{42}S, the branching is essentially reversed with 84% predicted for the $2_2^+ \rightarrow 0_1^+$ transition and only 16% for the $2_2^+ \rightarrow 2_1^+$ decay. The non-observation of

the $2^+_2 \rightarrow 0^+_1$ branch in ^{38}S here and in [95] and the 85(2)% branch for $(2^+_2) \rightarrow 0^+_1$ in ^{42}S reported here are in remarkable agreement with this sudden structural change. We note that in ^{40}S the 2^+_2 level could not be identified — it is expected in a region of already high level density — and, solely based on energy, the 1850 keV γ ray may be a candidate for the 2^+_2 to 2^+_1 transition.

The reason for the abrupt change in the decay pattern of the 2^+_2 state in ^{42}S lies in its neutron single-particle structure. The 2^+_1 and 2^+_2 states in ^{42}S differ in the occupancies of the $0f_{7/2}$ and $1p_{3/2}$ neutron orbitals as detailed below. These two orbitals cannot be connected by the $M1$ magnetic dipole transition operator. Consequently, the $B(M1; 2^+_2 \rightarrow 2^+_1) \equiv B(M1)$ transition strength is strongly hindered with $B(M1) = 0.1355 \cdot 10^{-3}$ μ^2_N in ^{42}S versus $B(M1) = 0.1924$ μ^2_N in ^{40}S, disfavoring the $2^+_2 \rightarrow 2^+_1$ branch at $N = 26$. Figure C.20 illustrates this by showing the occupancies of the neutron $1p_{3/2}$ orbital for the 0^+ (red) and 2^+ (blue) states up to 4.5 MeV from the calculations with the SDPF-MU Hamiltonian. Here, an increase of the neutron $1p_{3/2}$ occupancy is correlated with a decrease of the neutron $0f_{7/2}$ occupancy. The 2^+ state with the largest $1p_{3/2}$ occupancy is lowered in energy between ^{38}S and ^{42}S due to a reduction in the $1p_{3/2} - 0f_{7/2}$ single-particle gap as the neutron number increases. Up to ^{42}S, the configurations of the 0^+ and 2^+ states below 2 MeV are dominated by the $(a) = (0f_{7/2})^n$ configuration. The wave functions of the states above 2 MeV in ^{42}S are dominated by the $(b) = (0f_{7/2})^{(n-2)}(1p_{3/2})^2$ configuration[2]. Of all S isotopes shown, the neutron $p_{3/2}$ occupancy differs the most between the 2^+_1 and 2^+_2 states in ^{42}S, leading to the hindrance of the corresponding $2^+_2 \rightarrow 2^+_1$ $M1$ transition and the resulting very small $B(M1)$ value quoted above.

---

[2]Due to the mixing of (a) and (b) and a small occupancy of the $0f_{5/2}$ and $1p_{1/2}$ orbitals, the change in the occupancy of the $p_{3/2}$ orbital is not exactly 2 between the two groups of states.

Figure C.20 shows a dramatic change in the 0^+ and 2^+ level density below 4 MeV for ^{44}S and ties this to the excitation of neutrons across the $N = 28$ shell gap into the $p_{3/2}$ orbital. In ^{44}S, the correlation energy of the shell-breaking (b) configuration now becomes larger than that of the closed-shell configuration (a), putting ^{44}S inside the "island of inversion" at $N = 28$. The sensitivity of the $2_2^+ \rightarrow 2_1^+$ $M1$ decay to the $p_{3/2}$ neutron intruder occupancy now provides a very stringent test for the shell evolution leading up to the $N = 28$ "island of inversion". Our observation of a small $2_2^+ \rightarrow 2_1^+$ branch in ^{42}S, in agreement with the SDPF-MU calculations, indicates that this shell-model Hamiltonian indeed captures the changes in the neutron single-particle structure in the S isotopic chain as $N = 28$ is approached. It also illustrates how sudden the comparably simple structure of ^{42}S evolves into the complexity encountered for ^{44}S as the $N = 28$ shell closure breaks down.

For the odd-mass isotope ^{39}S, the expected low-lying nanosecond isomers, to which the present measurement is insensitive, prevent the construction of an experimental level scheme based on energy sums in the absence of clear coincidences and knowledge of the energies of the isomeric states. For ^{41}S on the other hand, the proposed experimental level scheme seems complete below 2.2 MeV and agrees remarkably well with the shell-model predictions. Given the complexity of the structure of the S isotopes, this agreement is noteworthy.

From all cases investigated here, a consistent picture emerges for the population of excited states in fragmentation reactions. Transitions from yrast states are the most prominent, visible even at low statistics (e.g. ^{38}S). For the higher statistics cases of ^{40,41,42}S, the presence of a multitude of weaker transitions can be understood as resulting from connections between the regions of high level density, upward from 3-4 MeV excitation energy, and the low-lying level scheme. While this may always have been the assumption behind the population of excited states in fragmentation reactions, evidence is presented here for
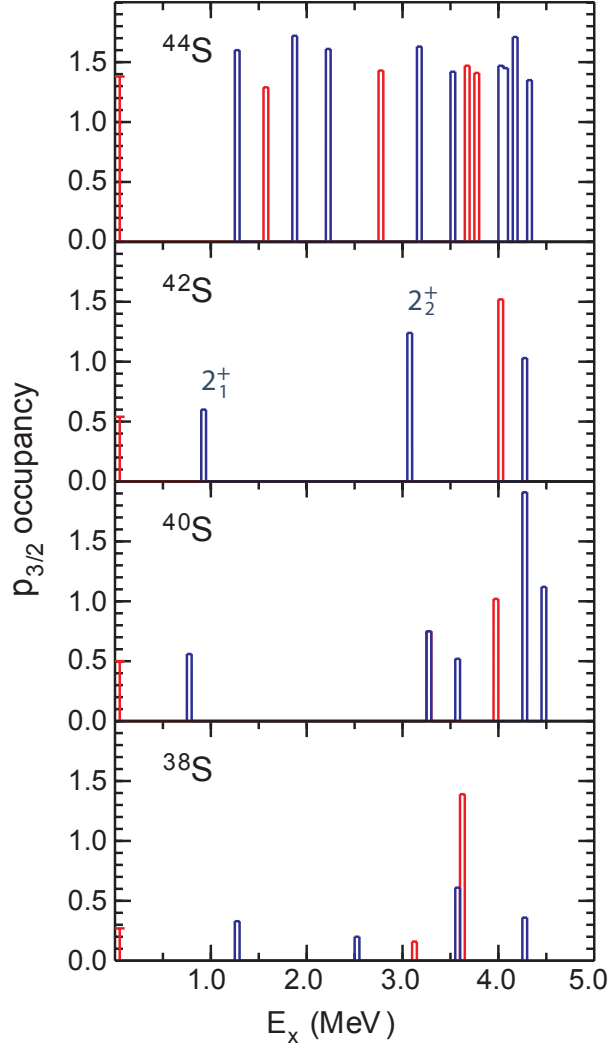
Figure C.20: Shell-model (SDPF-MU) neutron $p_{3/2}$ occupancy for the 0^+ (red) and 2^+ (blue) states of $^{38-44}$S below 4.5 MeV. The rapid onset of neutron $p_{3/2}$ occupancy together with the dramatic increase in the level density of 0^+ and 2^+ states in ^{44}S signals a sudden transition into the $N = 28$ "island of inversion" in the S isotopic chain. The role of ^{42}S as a sensitive probe for the neutron configurations is discussed in the text.

the many feeding transitions that have remained unobserved in previous work discussing fragmentation reactions specifically for S isotopes [92] or the population of excited states in projectile-like fragmentation residues in general [109]. In the case of ^{41}S(^{42}S), all calculated negative(positive) parity states below 2.2 MeV(3.5 MeV) have been matched to states in our proposed level schemes, including off-yrast states, while many weaker transitions remain unplaced. The prominence of yrast states can likely be attributed to their significant indirect feeding from the regions of high level density in addition to their direct population in the fragmentation reaction.

Summary

We have performed in-beam γ-ray spectroscopy on neutron-rich sulfur isotopes populated by fragmentation of intermediate-energy ^{48}Ca and ^{46}Ar projectile beams. New transitions were identified in $^{39-42}$S and new level schemes for $^{40-42}$S are proposed from $\gamma\gamma$ coincidence information, energy sums and comparison to the shell model. Shell-model calculations with the SDPF-MU Hamiltonian provide remarkable agreement and consistency with the proposed level schemes. For the even-mass S isotopes, the evolution of the yrast sequence is discussed in terms of $E(6^+)/E(2^+)$ and $E(4^+)/E(2^+)$ energy ratios. For ^{42}S, a candidate for the 2_2^+ state is proposed that exhibits a unique decay pattern as compared to ^{38,40}S. This is rooted in its neutron single-particle structure and confirmed by the SDPF-MU shell-model calculations. For the odd-mass ^{41}S, a level scheme is presented that appears complete below 2.2 MeV and consistent with the predictions by SDPF-MU shell-model Hamiltonian; this is a remarkable benchmark given the rapid shell and shape evolution prevalent in this textbook isotopic chain as the diminished $N = 28$ shell gap is approached.

BIBLIOGRAPHY

BIBLIOGRAPHY

[1] Douglas Cline. Nuclear shapes studied by Coulomb excitation. *Annual Review of Nuclear and Particle Science*, 36(1):683–716, 1986.

[2] K. Alder, A. Winther, and John L. Gammel. Electromagnetic excitation: Theory of Coulomb excitation with heavy ions. *Physics Today*, 29:63, 1976.

[3] A. Bohr and B.R. Mottelson. *Nuclear Structure*, volume 2 of *Nuclear Structure*. World Scientific, 1998.

[4] B. Alex Brown. Lecture notes in nuclear structure physics. *National Superconducting Cyclotron Laboratory*, 2017.

[5] G. M. Temmer and N. P. Heydenburg. Coulomb excitation of medium-weight nuclei. *Phys. Rev.*, 104:967–980, Nov 1956.

[6] P. H. Stelson and F. K. McGowan. Coulomb excitation of medium-weight even-even nuclei. *Phys. Rev.*, 110:489–506, Apr 1958.

[7] O. Sorlin and M.-G. Porquet. Nuclear magic numbers: New features far from stability. *Progress in Particle and Nuclear Physics*, 61(2):602 – 673, 2008.

[8] Alexandra Gade and Thomas Glasmacher. In-beam nuclear spectroscopy of bound states with fast exotic ion beams. *Progress in Particle and Nuclear Physics*, 60(1):161 – 224, 2008.

[9] Michigan State University. Cyclotron Laboratory. *Isotope Science Facility at Michigan State University: Upgrade of the NSCL Rare Isotope Research Capabilities*. Michigan State University, 2006.

[10] David J. Morrissey and Bradley M. Sherrill. Radioactive nuclear beam facilities based on projectile fragmentation. *Philosophical Transactions of the Royal Society of London A: Mathematical, Physical and Engineering Sciences*, 356(1744):1985–2006, 1998.

[11] Thomas Glasmacher. Coulomb excitation at intermediate energies. *Annual Review of Nuclear and Particle Science*, 48(1):1–31, 1998.

[12] Aage Winther and Kurt Alder. Relativistic Coulomb excitation. *Nuclear Physics A*, 319(3):518 – 532, 1979.

[13] T. Motobayashi, Y. Ikeda, Y. Ando, K. Ieki, M. Inoue, N. Iwasa, T. Kikuchi, M. Kurokawa, S. Moriya, S. Ogawa, H. Murakami, S. Shimoura, Y. Yanagiswaw,

T. Nakamura, Y. Watanabe, M. Ishihara, T. Teranishia, H. Okuno, and R.F. Casten. Large deformation of the very neutron-rich nucleus ^{32}Mg from intermediate-energy Coulomb excitation. *Physics Letters B*, 346(1):9–14, 1995.

[14] A. Gade, D. Bazin, C. M. Campbell, J. A. Church, D. C. Dinca, J. Enders, T. Glasmacher, Z. Hu, K. W. Kemper, W. F. Mueller, H. Olliver, B. C. Perry, L. A. Riley, B. T. Roeder, B. M. Sherrill, and J. R. Terry. Detailed experimental study on intermediate-energy Coulomb excitation of ^{46}Ar. *Phys. Rev. C*, 68:014302, Jul 2003.

[15] K. L. Yurkewicz, D. Bazin, B. A. Brown, C. M. Campbell, J. A. Church, D.-C. Dinca, A. Gade, T. Glasmacher, M. Honma, T. Mizusaki, W. F. Mueller, H. Olliver, T. Otsuka, L. A. Riley, and J. R. Terry. Intermediate-energy Coulomb excitation of ^{52}Fe. *Phys. Rev. C*, 70:034301, Sep 2004.

[16] C. Vaman, C. Andreoiu, D. Bazin, A. Becerril, B. A. Brown, C. M. Campbell, A. Chester, J. M. Cook, D. C. Dinca, A. Gade, D. Galaviz, T. Glasmacher, M. Hjorth-Jensen, M. Horoi, D. Miller, V. Moeller, W. F. Mueller, A. Schiller, K. Starosta, A. Stolz, J. R. Terry, A. Volya, V. Zelevinsky, and H. Zwahlen. $Z = 50$ shell gap near ^{100}Sn from intermediate-energy Coulomb excitations in even-mass $^{106-112}$Sn isotopes. *Phys. Rev. Lett.*, 99:162501, Oct 2007.

[17] S. Ettenauer, H. Zwahlen, P. Adrich, D. Bazin, C. M. Campbell, J. M. Cook, A. D. Davies, D.-C. Dinca, A. Gade, T. Glasmacher, J.-L. Lecouey, W. F. Mueller, T. Otsuka, R. R. Reynolds, L. A. Riley, J. R. Terry, Y. Utsuno, and K. Yoneda. Intermediate-energy Coulomb excitation of ^{30}Na. *Phys. Rev. C*, 78:017302, Jul 2008.

[18] R. Winkler, A. Gade, T. Baugher, D. Bazin, B. A. Brown, T. Glasmacher, G. F. Grinyer, R. Meharchand, S. McDaniel, A. Ratkiewicz, and D. Weisshaar. Quadrupole collectivity beyond $N = 28$: Intermediate-energy Coulomb excitation of ^{47,48}Ar. *Phys. Rev. Lett.*, 108:182501, Apr 2012.

[19] T. Baugher, A. Gade, R. V. F. Janssens, S. M. Lenzi, D. Bazin, B. A. Brown, M. P. Carpenter, A. N. Deacon, S. J. Freeman, T. Glasmacher, G. F. Grinyer, F. G. Kondev, S. McDaniel, A. Poves, A. Ratkiewicz, E. A. McCutchan, D. K. Sharp, I. Stefanescu, K. A. Walsh, D. Weisshaar, and S. Zhu. Intermediate-energy Coulomb excitation of ^{58,60,62}Cr: The onset of collectivity toward $N = 40$. *Phys. Rev. C*, 86:011305, Jul 2012.

[20] D.C. Kean. Measurement of quadrupole moments through Coulomb excitation. pages 80–94. Springer, 1976.

[21] A. Gade and S.N. Liddick. Shape coexistence in neutron-rich nuclei. *Journal of Physics G: Nuclear and Particle Physics*, 43(2):024001, 2016.

[22] A.C.C. Villari. The accelerated ISOL technique and the SPIRAL project. *Nuclear Physics A*, 693(1):465 – 476, 2001.

[23] M. A. Schumaker, D. Cline, G. Hackman, C. Pearson, C. E. Svensson, C. Y. Wu, A. Andreyev, R. A. E. Austin, G. C. Ball, D. Bandyopadhyay, J. A. Becker, A. J. Boston, H. C. Boston, L. Buchmann, R. Churchman, F. Cifarelli, R. J. Cooper, D. S. Cross, D. Dashdorj, G. A. Demand, M. R. Dimmock, T. E. Drake, P. Finlay, A. T. Gallant, P. E. Garrett, K. L. Green, A. N. Grint, G. F. Grinyer, L. J. Harkness, A. B. Hayes, R. Kanungo, A. F. Lisetskiy, K. G. Leach, G. Lee, R. Maharaj, J-P. Martin, F. Moisan, A. C. Morton, S. Mythili, L. Nelson, O. Newman, P. J. Nolan, J. N. Orce, E. Padilla-Rodal, A. A. Phillips, M. Porter-Peden, J. J. Ressler, R. Roy, C. Ruiz, F. Sarazin, D. P. Scraggs, J. C. Waddington, J. M. Wan, A. Whitbeck, S. J. Williams, and J. Wong. Coulomb excitation of radioactive ^{20,21}Na. *The European Physical Journal A*, 42(3):477, Jun 2009.

[24] J. Van de Walle, F. Aksouh, F. Ames, T. Behrens, V. Bildstein, A. Blazhev, J. Cederkäll, E. Clément, T. E. Cocolios, T. Davinson, P. Delahaye, J. Eberth, A. Ekström, D. V. Fedorov, V. N. Fedosseev, L. M. Fraile, S. Franchoo, R. Gernhauser, G. Georgiev, D. Habs, K. Heyde, G. Huber, M. Huyse, F. Ibrahim, O. Ivanov, J. Iwanicki, J. Jolie, O. Kester, U. Köster, T. Kröll, R. Krücken, M. Lauer, A. F. Lisetskiy, R. Lutter, B. A. Marsh, P. Mayet, O. Niedermaier, T. Nilsson, M. Pantea, O. Perru, R. Raabe, P. Reiter, M. Sawicka, H. Scheit, G. Schrieder, D. Schwalm, M. D. Seliverstov, T. Sieber, G. Sletten, N. Smirnova, M. Stanoiu, I. Stefanescu, J.-C. Thomas, J. J. Valiente-Dobón, P. Van Duppen, D. Verney, D. Voulot, N. Warr, D. Weisshaar, F. Wenander, B. H. Wolf, and M. Zielińska. Coulomb excitation of neutron-rich Zn isotopes: First observation of the 2_1^+ state in ^{80}Zn. *Phys. Rev. Lett.*, 99:142501, Oct 2007.

[25] E. Kwan, C.Y. Wu, N.C. Summers, G. Hackman, T.E. Drake, C. Andreoiu, R. Ashley, G.C. Ball, P.C. Bender, A.J. Boston, H.C. Boston, A. Chester, A. Close, D. Cline, D.S. Cross, R. Dunlop, A. Finley, A. Garnsworthy, A.B. Hayes, A. Laffoley, T. Nano, P. Voss, S.J. Williams, and Z.M. Wang. Precision measurements of the B(E1) strengths in ^{11}Be. Technical report, Lawrence Livermore National Laboratory (LLNL), Livermore, CA, 2012.

[26] L. P. Gaffney, P. A. Butler, M. Scheck, A. B. Hayes, F. Wenander, M. Albers, B. Bastin, C. Bauer, A. Blazhev, S. Bonig, N. Bree, J. Cederkall, T. Chupp, D. Cline, T. E. Cocolios, T. Davinson, H. De Witte, J. Diriken, T. Grahn, A. Herzan, M. Huyse, D. G. Jenkins, D. T. Joss, N. Kesteloot, J. Konki, M. Kowalczyk, Th Kroll, E. Kwan, R. Lutter, K. Moschner, P. Napiorkowski, J. Pakarinen, M. Pfeiffer, D. Radeck, P. Reiter, K. Reynders, S. V. Rigby, L. M. Robledo, M. Rudigier, S. Sambi, M. Seidlitz, B. Siebeck, T. Stora, P. Thoele, P. Van Duppen, M. J. Vermeulen, M. von Schmid, D. Voulot, N. Warr, K. Wimmer, K. Wrzosek-Lipska, C. Y. Wu, and M. Zielinska. Studies of pear-shaped nuclei using accelerated radioactive beams. *Nature*, 497(7448):199–204, May 2013.

[27] I. Stefanescu, G. Georgiev, F. Ames, J. Äystö, D. L. Balabanski, G. Bollen, P. A. Butler, J. Cederkäll, N. Champault, T. Davinson, A. De Maesschalck, P. Delahaye, J. Eberth, D Fedorov, V. N. Fedosseev, L. M. Fraile, S. Franchoo, K. Gladnishki, D. Habs, K. Heyde, M. Huyse, O. Ivanov, J. Iwanicki, J. Jolie, B. Jonson, Th. Kröll, R. Krücken, O. Kester, U Köster, A. Lagoyannis, L. Liljeby, G. Lo Bianco, B. A. Marsh, O. Niedermaier, T. Nilsson, M. Oinonen, G. Pascovici, P. Reiter, A. Saltarelli, H. Scheit, D. Schwalm, T. Sieber, N. Smirnova, J. Van De Walle, P. Van Duppen, S. Zemlyanoi, N. Warr, D. Weisshaar, and F. Wenander. Coulomb excitation of ^{68,70}Cu: First use of postaccelerated isomeric beams. *Phys. Rev. Lett.*, 98:122701, Mar 2007.

[28] A. Ekström, J. Cederkäll, C. Fahlander, M. Hjorth-Jensen, T. Engeland, A. Blazhev, P. A. Butler, T. Davinson, J. Eberth, F. Finke, A. Görgen, M. Górska, A. M. Hurst, O. Ivanov, J. Iwanicki, U. Köster, B. A. Marsh, J. Mierzejewski, P. Reiter, S. Siem, G. Sletten, I. Stefanescu, G. M. Tveten, J. Van de Walle, D. Voulot, N. Warr, D. Weisshaar, F. Wenander, and M. Zielińska. Coulomb excitation of the odd-odd isotopes ^{106,108}In. *The European Physical Journal A*, 44(3):355–361, Jun 2010.

[29] G. Savard, R. C. Pardo, S. Baker, C. N. Davids, A. Levand, D. Peterson, D. G. Phillips, T. Sun, R. Vondrasek, B. J. Zabransky, and G. P. Zinkann. CARIBU: a new facility for the study of neutron-rich isotopes. *Hyperfine Interactions*, 199(1):301–309, Jul 2011.

[30] B. Bucher, S. Zhu, C. Y. Wu, R. V. F. Janssens, D. Cline, A. B. Hayes, M. Albers, A. D. Ayangeakaa, P. A. Butler, C. M. Campbell, M. P. Carpenter, C. J. Chiara, J. A. Clark, H. L. Crawford, M. Cromaz, H. M. David, C. Dickerson, E. T. Gregor, J. Harker, C. R. Hoffman, B. P. Kay, F. G. Kondev, A. Korichi, T. Lauritsen, A. O. Macchiavelli, R. C. Pardo, A. Richard, M. A. Riley, G. Savard, M. Scheck, D. Seweryniak, M. K. Smith, R. Vondrasek, and A. Wiens. Direct evidence of octupole deformation in neutron-rich ^{144}Ba. *Phys. Rev. Lett.*, 116:112503, Mar 2016.

[31] B. Bucher, S. Zhu, C. Y. Wu, R. V. F. Janssens, R. N. Bernard, L. M. Robledo, T. R. Rodríguez, D. Cline, A. B. Hayes, A. D. Ayangeakaa, M. Q. Buckner, C. M. Campbell, M. P. Carpenter, J. A. Clark, H. L. Crawford, H. M. David, C. Dickerson, J. Harker, C. R. Hoffman, B. P. Kay, F. G. Kondev, T. Lauritsen, A. O. Macchiavelli, R. C. Pardo, G. Savard, D. Seweryniak, and R. Vondrasek. Direct evidence for octupole deformation in ^{146}Ba and the origin of large $E1$ moment variations in reflection-asymmetric nuclei. *Phys. Rev. Lett.*, 118:152504, Apr 2017.

[32] D.T. Doherty, J.M. Allmond, R.V.F. Janssens, W. Korten, S. Zhu, M. Zieliska, D.C. Radford, A.D. Ayangeakaa, B. Bucher, J.C. Batchelder, C.W. Beausang, C. Campbell, M.P. Carpenter, D. Cline, H.L. Crawford, H.M. David, J.P. Delaroche, C. Dickerson, P. Fallon, A. Galindo-Uribarri, F.G. Kondev, J.L. Harker, A.B. Hayes, M. Hendricks, P. Humby, M. Girod, C.J. Gross, M. Klintefjord, K. Kolos, G.J. Lane, T. Lauritsen, J. Libert, A.O. Macchiavelli, P.J. Napiorkowski, E. Padilla-Rodal, R.C. Pardo, W. Reviol, D.G. Sarantites, G. Savard, D. Seweryniak, J. Srebrny, R. Varner, R. Vondrasek,

A. Wiens, E. Wilson, J.L. Wood, and C.Y. Wu. Triaxiality near the ^{110}Ru ground state from Coulomb excitation. *Physics Letters B*, 766:334 – 338, 2017.

[33] A. Gade and B.M. Sherrill. NSCL and FRIB at Michigan State University: Nuclear science at the limits of stability. *Physica Scripta*, 91(5):053003, 2016.

[34] W.F. Mueller, J.A. Church, T. Glasmacher, D. Gutknecht, G. Hackman, P.G. Hansen, Z. Hu, K.L. Miller, and P. Quirin. Thirty-two-fold segmented germanium detectors to identify γ-rays from intermediate-energy exotic beams. *Nuclear Instruments and Methods in Physics Research Section A: Accelerators, Spectrometers, Detectors and Associated Equipment*, 466(3):492 – 498, 2001.

[35] Kurt Alder, Aage Bohr, Torben Huus, Ben Mottelson, and Aage Winther. Study of nuclear structure by electromagnetic excitation with accelerated ions. *Reviews of Modern Physics*, 28(4):432, 1956.

[36] D. Cline, T. Czosnyka, A. Hayes, P. Napiorkowski, N. Warr, and C.Y. Wu. GOSIA user manual for simulation and analysis of Coulomb excitation experiments. *Gosia Steering Committee*, 18:19–60, 2012.

[37] Kris Heyde. *Basic ideas and concepts in nuclear physics: an introductory approach.* CRC Press, 2004.

[38] T. Czosnyka, D. Cline, L. Hasselgren, C.Y. Wu, R.M. Diamond, H. Kluge, C. Roulet, E.K. Hulet, R.W. Lougheed, and C. Baktash. E2 properties of the ground state band in ^{248}Cm. *Nuclear Physics A*, 458(1):123 – 136, 1986.

[39] William R. Leo. *Techniques for nuclear and particle physics experiments: a how-to approach.* Springer Science & Business Media, 2012.

[40] James F. Ziegler, M.D. Ziegler, and J.P. Biersack. SRIM — the stopping and range of ions in matter (2010). *Nuclear Instruments and Methods in Physics Research Section B: Beam Interactions with Materials and Atoms*, 268(1112):1818 – 1823, 2010. 19th International Conference on Ion Beam Analysis.

[41] M. J. Berger, J. H. Hubbell, S. M. Seltzer, J. Chang, J. S. Coursey, R. Sukumar, D. S. Zucker, and K. Olsen. XCOM: Photon Cross Sections Database (version 1.5). *National Institute of Standards and Technology, Gaithersburg, MD*, 2010.

[42] Glenn F. Knoll. *Radiation detection and measurement.* John Wiley & Sons, 2010.

[43] Steven Ragnar Stroberg. *Single-particle structure of neutron-rich silicon isotopes and the breakdown of the N=28 shell closure.* Michigan State University, 2014.

[44] C.J. Prokop, S.N. Liddick, B.L. Abromeit, A.T. Chemey, N.R. Larson, S. Suchyta, and J.R. Tompkins. Digital data acquisition system implementation at the national superconducting cyclotron laboratory. *Nuclear Instruments and Methods in Physics Research Section A: Accelerators, Spectrometers, Detectors and Associated Equipment*, 741:163 – 168, 2014.

[45] NSCL data acquisition documentation. `http://docs.nscl.msu.edu/daq/newsite/home.php`. Accessed: 2017-07-25.

[46] J.S. Fraser, J.C.D. Milton, H.R. Bowman, and S.G. Thompson. Precise kinetic energy measurements and fine structure in the spontaneous fission of Cf^{252}. *Canadian Journal of Physics*, 41(12):2080–2097, 1963.

[47] A.C.C. Villari, D. Alt, G. Bollen, D.B. Crisp, M. Ikegami, S.W. Krause, A. Lapierre, S.M. Lidia, D.J. Morrissey, S. Nash, R.J. Rencsok, R. Ringle, S. Schwarz, R. Shane, C. Sumithrarachchi, S.J. Williams, and Qiang Zhao. Commissioning and first accelerated beams in the reaccelerator (ReA3) of the National Superconducting Cyclotron Laboratory, MSU. *International Particle Accelerator Conference*, pages 1287–1290, 2016.

[48] A. Lapierre, S. Schwarz, T. M. Baumann, K. Cooper, K. Kittimanapun, A. J. Rodriguez, C. Sumithrarachchi, S. J. Williams, W. Wittmer, D. Leitner, and G. Bollen. First charge breeding of a rare-isotope beam with the electron-beam ion trap of the rea post-accelerator at the national superconducting cyclotron laboratory. *Review of Scientific Instruments*, 85(2):02B701, 2014.

[49] Morton A. Levine, R.E. Marrs, J.R. Henderson, D.A. Knapp, and Marilyn B. Schneider. The electron beam ion trap: A new instrument for atomic physics measurements. *Physica Scripta*, 1988(T22):157, 1988.

[50] A. Gade and H. Iwasaki. ReA energy upgrade. 2016.

[51] Herbert Goldstein, Charles Poole, and John Safko. Classical mechanics, 2002.

[52] Ameenah R. Farhan and Balraj Singh. Nuclear data sheets for A = 78. *Nuclear Data Sheets*, 110(9):1917 – 2080, 2009.

[53] H. Toki and Amand Faessler. Extended VMI model for asymmetric deformed nuclei. *Zeitschrift für Physik A Atoms and Nuclei*, 276(1):35–43, Mar 1976.

[54] R. L. Robinson, H. J. Kim, R. O. Sayer, W. T. Milner, R. B. Piercey, J. H. Hamilton, A. V. Ramayya, J. C. Wells, and A. J. Caffrey. High-spin levels and band structure in ^{78}Kr. *Phys. Rev. C*, 21:603–613, Feb 1980.

[55] F. Becker, A. Petrovici, J. Iwanicki, N. Amzal, W. Korten, K. Hauschild, A. Hurstel, Ch. Theisen, P.A. Butler, R.A. Cunningham, T. Czosnyka, G. de France, J. Gerl, P. Greenlees, K. Helariutta, R.-D. Herzberg, P. Jones, R. Julin, S. Juutinen, H. Kankaanp, M. Muikku, P. Nieminen, O. Radu, P. Rahkila, and Ch. Schlegel. Coulomb excitation of ^{78}Kr. *Nuclear Physics A*, 770(3):107 – 125, 2006.

[56] K. S. Krane and R. M. Steffen. Determination of the $\frac{E2}{M1}$ multipole mixing ratios of the gamma transitions in Cd^{110}. *Phys. Rev. C*, 2:724–734, Aug 1970.

[57] L. P. Gaffney, A. P. Robinson, D. G. Jenkins, A. N. Andreyev, M. Bender, A. Blazhev, N. Bree, B. Bruyneel, P. A. Butler, T. E. Cocolios, T. Davinson, A. N. Deacon, H. De Witte, D. DiJulio, J. Diriken, A. Ekström, Ch. Fransen, S. J. Freeman, K. Geibel, T. Grahn, B. Hadinia, M. Hass, P.-H. Heenen, H. Hess, M. Huyse, U. Jakobsson, N. Kesteloot, J. Konki, Th. Kröll, V. Kumar, O. Ivanov, S. Martin-Haugh, D. Mücher, R. Orlandi, J. Pakarinen, A. Petts, P. Peura, P. Rahkila, P. Reiter, M. Scheck, M. Seidlitz, K. Singh, J. F. Smith, J. Van de Walle, P. Van Duppen, D. Voulot, R. Wadsworth, N. Warr, F. Wenander, K. Wimmer, K. Wrzosek-Lipska, and M. Zielińska. Collectivity in the light radon nuclei measured directly via Coulomb excitation. *Phys. Rev. C*, 91:064313, Jun 2015.

[58] E. Nolte, Y. Shida, W. Kutschera, R. Prestele, and H. Morinaga. Investigation of neutron deficient nuclei in the region 28 < N, Z < 50 with the help of heavy ion compound reactions. *Z.Phys.*, 268:267, 1974.

[59] D. S. Andreev, K. I. Erokhina, I. Kh. Lemberg, A. A. Pasternak, L. A. Rassadin, and I. N. Chugunov. Lifetime measurements of excited states of ^{78}Kr. *Izv.Akad.Nauk. SSSR, Ser.Fiz.*, 46:30 – 44, 1982.

[60] G. Winter, F. Dubbers, J. Doring, L. Funke, P. Kemnitz, E. Will, D.S. Andreev, K.I. Erochina, I.Kh. Lemberg, A.A. Pasternak, L.A. Rassadin, and I.N. Chugunov. On the irregularities in the band structures of ^{78}Kr. *Journal of Physics G: Nuclear Physics*, 11(2):277, 1985.

[61] G. Garca Bermdez, M.A. Cardona, and A. Filevich. A simple plunger device and error analysis of nuclear lifetime measurements. *Nuclear Instruments and Methods in Physics Research Section A: Accelerators, Spectrometers, Detectors and Associated Equipment*, 292(2):367 – 372, 1990.

[62] H.P. Hellmeister, J. Keinonen, K.P. Lieb, U. Kaup, R. Rascher, R. Ballini, J. Delaunay, and H. Dumont. Study of high spin states in ^{78}Kr. *Nuclear Physics A*, 332(1):241 – 268, 1979.

[63] P.K. Joshi, H.C. Jain, R. Palit, G. Mukherjee, and S. Nagaraj. Shape evolution of yrast-band in ^{78}Kr. *Nuclear Physics A*, 700(1):59 – 69, 2002.

[64] R. L. Robinson, H. J. Kim, R. O. Sayer, W. T. Milner, R. B. Piercey, J. H. Hamilton, A. V. Ramayya, J. C. Wells, and A. J. Caffrey. High-spin levels and band structure in ^{78}Kr. *Phys. Rev. C*, 21:603–613, Feb 1980.

[65] T. J. Mertzimekis, N. Benczer-Koller, J. Holden, G. Jakob, G. Kumbartzki, K.-H. Speidel, R. Ernst, A. Macchiavelli, M. McMahan, L. Phair, P. Maier-Komor, A. Pakou, S. Vincent, and W. Korten. First measurements of g factors in the even Kr isotopes. *Phys. Rev. C*, 64:024314, Jul 2001.

[66] M. Zielińska, L.P. Gaffney, Kasia Wrzosek-Lipska, E. Clément, Tuomas Grahn, Nele Kesteloot, P. Napiorkowski, Janne Pakarinen, Piet Van Duppen, and N. Warr. Analysis methods of safe Coulomb-excitation experiments with radioactive ion beams using the GOSIA code. *The European Physical Journal A*, 52(4):99, 2016.

[67] A. Giannatiempo, A. Nannini, A. Perego, P. Sona, M. J. G. Borge, and O. Tengblad. Decay properties of the 0_2^+ state and spin-parity assignments in ^{78}Kr. *Phys. Rev. C*, 52:2444–2447, Nov 1995.

[68] J. Billowes, F. Cristancho, H. Grawe, C. J. Gross, J. Heese, A. W. Mountford, and M. Weiszflog. Neutron alignment at the first crossing in ^{78}Kr. *Phys. Rev. C*, 47:R917–R921, Mar 1993.

[69] G. K. Bavaria, J. E. Crawford, S. Calamawy, and J. E. Kitching. The decay of ^{78g}Rb and ^{78m}Rb to levels in ^{78}Kr. *Z.Phys.*, A302:329, 1981.

[70] N. Yoshikawa, Y. Shida, O. Hashimoto, M. Sakai, and T. Numao. Levels in ^{74}Se, ^{78,80}Kr and ^{84}Sr and systematics of quasi-γ bands. *Nuclear Physics A*, 327(2):477 – 489, 1979.

[71] H. Scheit, T. Glasmacher, B. A. Brown, J. A. Brown, P. D. Cottle, P. G. Hansen, R. Harkewicz, M. Hellström, R. W. Ibbotson, J. K. Jewell, K. W. Kemper, D. J. Morrissey, M. Steiner, P. Thirolf, and M. Thoennessen. New region of deformation: The neutron-rich sulfur isotopes. *Phys. Rev. Lett.*, 77:3967–3970, Nov 1996.

[72] T. Glasmacher, B.A. Brown, M.J. Chromik, P.D. Cottle, M. Fauerbach, R.W. Ibbotson, K.W. Kemper, D.J. Morrissey, H. Scheit, D.W. Sklenicka, and M. Steiner. Collectivity in ^{44}S. *Physics Letters B*, 395(3):163 – 168, 1997.

[73] D. Santiago-Gonzalez, I. Wiedenhöver, V. Abramkina, M. L. Avila, T. Baugher, D. Bazin, B. A. Brown, P. D. Cottle, A. Gade, T. Glasmacher, K. W. Kemper, S. McDaniel, A. Rojas, A. Ratkiewicz, R. Meharchand, E. C. Simpson, J. A. Tostevin, A. Volya, and D. Weisshaar. Triple configuration coexistence in ^{44}S. *Phys. Rev. C*, 83:061305, Jun 2011.

[74] Yutaka Utsuno, Noritaka Shimizu, Takaharu Otsuka, Tooru Yoshida, and Yusuke Tsunoda. Nature of isomerism in exotic sulfur isotopes. *Phys. Rev. Lett.*, 114:032501, Jan 2015.

[75] J. Luis Egido, Marta Borrajo, and Tomás R. Rodríguez. Collective and single-particle motion in beyond mean field approaches. *Phys. Rev. Lett.*, 116:052502, Feb 2016.

[76] J. J. Parker, I. Wiedenhöver, P. D. Cottle, J. Baker, D. McPherson, M. A. Riley, D. Santiago-Gonzalez, A. Volya, V. M. Bader, T. Baugher, D. Bazin, A. Gade, T. Ginter, H. Iwasaki, C. Loelius, C. Morse, F. Recchia, D. Smalley, S. R. Stroberg, K. Whitmore, D. Weisshaar, A. Lemasson, H. L. Crawford, A. O. Macchiavelli, and K. Wimmer. Isomeric character of the lowest observed 4^+ state in ^{44}S. *Phys. Rev. Lett.*, 118:052501, Jan 2017.

[77] C. Force, S. Grévy, L. Gaudefroy, O. Sorlin, L. Cáceres, F. Rotaru, J. Mrazek, N. L. Achouri, J. C. Angélique, F. Azaiez, B. Bastin, R. Borcea, A. Buta, J. M. Daugas, Z. Dlouhy, Zs. Dombrádi, F. De Oliveira, F. Negoita, Y. Penionzhkevich, M. G. Saint-Laurent, D. Sohler, M. Stanoiu, I. Stefan, C. Stodel, and F. Nowacki. Prolate-spherical shape coexistence at $N = 28$ in ^{44}S. *Phys. Rev. Lett.*, 105:102501, Sep 2010.

[78] T.R. Werner, J.A. Sheikh, W. Nazarewicz, M.R. Strayer, A.S. Umar, and M. Misu. Shape coexistence around $^{44}_{16}S_{28}$: the deformed $N = 28$ region. *Physics Letters B*, 335(3):259 – 265, 1994.

[79] M. Kimura, Y. Taniguchi, Y. Kanada-En'yo, H. Horiuchi, and K. Ikeda. Prolate, oblate, and triaxial shape coexistence, and the lost magicity of $N = 28$ in ^{43}S. *Phys. Rev. C*, 87:011301, Jan 2013.

[80] Rene Brun and Fons Rademakers. Root – an object oriented data analysis framework. *Nuclear Instruments and Methods in Physics Research Section A: Accelerators, Spectrometers, Detectors and Associated Equipment*, 389(1):81 – 86, 1997.

[81] D. Bazin, J.A. Caggiano, B.M. Sherrill, J. Yurkon, and A. Zeller. The S800 spectrograph. *Nuclear Instruments and Methods in Physics Research Section B: Beam Interactions with Materials and Atoms*, 204:629 – 633, 2003. 14th International Conference on Electromagnetic Isotope Separators and Techniques Related to their Applications.

[82] T. Kibdi, T.W. Burrows, M.B. Trzhaskovskaya, P.M. Davidson, and C.W. Nestor. Evaluation of theoretical conversion coefficients using BrIcc. *Nuclear Instruments and Methods in Physics Research Section A: Accelerators, Spectrometers, Detectors and Associated Equipment*, 589(2):202 – 229, 2008.

[83] E. Lunderberg, A. Gade, V. Bader, T. Baugher, D. Bazin, J. S. Berryman, B. A. Brown, D. J. Hartley, F. Recchia, S. R. Stroberg, D. Weisshaar, and K. Wimmer. In-beam γ-ray spectroscopy of $^{38-42}$S. *Phys. Rev. C*, 94:064327, Dec 2016.

[84] Yutaka Utsuno, Takaharu Otsuka, B. Alex Brown, Michio Honma, Takahiro Mizusaki, and Noritaka Shimizu. Shape transitions in exotic Si and S isotopes and tensor-force-driven Jahn-Teller effect. *Phys. Rev. C*, 86:051301, Nov 2012.

[85] R. Chevrier, J. M. Daugas, L. Gaudefroy, Y. Ichikawa, H. Ueno, M. Hass, H. Haas, S. Cottenier, N. Aoi, K. Asahi, D. L. Balabanski, N. Fukuda, T. Furukawa, G. Georgiev, H. Hayashi, H. Iijima, N. Inabe, T. Inoue, M. Ishihara, Y. Ishii, D. Kameda, T. Kubo, T. Nanao, G. Neyens, T. Ohnishi, M. M. Rajabali, K. Suzuki, H. Takeda, M. Tsuchiya, N. Vermeulen, H. Watanabe, and A. Yoshimi. Is the $7/2_1^-$ isomer state of ^{43}S spherical? *Phys. Rev. Lett.*, 108:162501, Apr 2012.

[86] Z. M. Wang, R. Chapman, F. Haas, X. Liang, F. Azaiez, B. R. Behera, M. Burns, L. Corradi, D. Curien, A. N. Deacon, Zs. Dombrádi, E. Farnea, E. Fioretto, A. Gadea, A. Hodsdon, F. Ibrahim, A. Jungclaus, K. Keyes, V. Kumar, A. Latina, N. Mărginean, G. Montagnoli, D. R. Napoli, J. Ollier, D. O'Donnell, A. Papenberg, G. Pollarolo, M.-D. Salsac, F. Scarlassara, J. F. Smith, K. M. Spohr, M. Stanoiu, A. M. Stefanini, S. Szilner, M. Trotta, and D. Verney. Collectivity in ^{41}S. *Phys. Rev. C*, 83:061304, Jun 2011.

[87] L. Gaudefroy, J. M. Daugas, M. Hass, S. Grévy, Ch. Stodel, J. C. Thomas, L. Perrot, M. Girod, B. Rossé, J. C. Angélique, D. L. Balabanski, E. Fiori, C. Force, G. Georgiev, D. Kameda, V. Kumar, R. L. Lozeva, I. Matea, V. Méot, P. Morel, B. S. Nara Singh, F. Nowacki, and G. Simpson. Shell erosion and shape coexistence in $^{43}_{16}$S$_{27}$. *Phys. Rev. Lett.*, 102:092501, Mar 2009.

[88] L. A. Riley, P. Adrich, T. R. Baugher, D. Bazin, B. A. Brown, J. M. Cook, P. D. Cottle, C. Aa. Diget, A. Gade, D. A. Garland, T. Glasmacher, K. E. Hosier, K. W. Kemper, A. Ratkiewicz, K. P. Siwek, J. A. Tostevin, and D. Weisshaar. Rotational and neutron-hole states in ^{43}S via the neutron knockout and fragmentation reactions. *Phys. Rev. C*, 80:037305, Sep 2009.

[89] R. Ringle, C. Bachelet, M. Block, G. Bollen, M. Facina, C. M. Folden, C. Guénaut, A. A. Kwiatkowski, D. J. Morrissey, G. K. Pang, A. M. Prinke, J. Savory, P. Schury, S. Schwarz, and C. S. Sumithrarachchi. High-precision Penning trap mass measurements of neutron-rich sulfur isotopes at the $N = 28$ shell closure. *Phys. Rev. C*, 80:064321, Dec 2009.

[90] R. W. Ibbotson, T. Glasmacher, P. F. Mantica, and H. Scheit. Coulomb excitation of odd-A neutron-rich $\pi(s-d)$ and $\nu(f-p)$ shell nuclei. *Phys. Rev. C*, 59:642–647, Feb 1999.

[91] F. Azaiez, M. Belleguic, D. Sohler, M. Stanoiu, Zs. Dombrádi, O. Sorlin, J. Timár, F. Amorini, D. Baiborodin, A. Bauchet, F. Becker, C. Borcea, C. Bourgeois, Z. Dlouhy, C. Donzaud, J. Duprat, D. Guillemaud-Mueller, F. Ibrahim, M.J. Lopez, R. Lucas, S.M. Lukyanov, V. Maslov, J. Mrazek, C. Moore, F. Nowacki, B.M. Nyakó, Yu.-E.

Penionzhkevich, M.G. Saint-Laurent, F. Sarazin, J.A. Scarpaci, G. Sletten, C. Stodel, M. Taylor, C. Theisen, and G. Voltolini. Probing shell structure in neutron-rich nuclei with in-beam γ-spectroscopy. *The European Physical Journal A - Hadrons and Nuclei*, 15(1):93–97, 2002.

[92] D. Sohler, Zs. Dombrádi, J. Timár, O. Sorlin, F. Azaiez, F. Amorini, M. Belleguic, C. Bourgeois, C. Donzaud, J. Duprat, D. Guillemaud-Mueller, F. Ibrahim, J. A. Scarpaci, M. Stanoiu, M. J. Lopez, M. G. Saint-Laurent, F. Becker, F. Sarazin, C. Stodel, G. Voltolini, S. M. Lukyanov, V. Maslov, Yu.-E. Penionzhkevich, M. Girod, S. Péru, F. Nowacki, G. Sletten, R. Lucas, C. Theisen, D. Baiborodin, Z. Dlouhy, J. Mrazek, C. Borcea, A. Bauchet, C. J. Moore, and M. J. Taylor. Shape evolution in heavy sulfur isotopes and erosion of the $N = 28$ shell closure. *Phys. Rev. C*, 66:054302, Nov 2002.

[93] Z. M. Wang, R. Chapman, X. Liang, F. Haas, F. Azaiez, B. R. Behera, M. Burns, E. Caurier, L. Corradi, D. Curien, A. N. Deacon, Zs. Dombrádi, E. Farnea, E. Fioretto, A. Gadea, A. Hodsdon, F. Ibrahim, A. Jungclaus, K. Keyes, V. Kumar, A. Latina, S. Lunardi, N. Mărginean, G. Montagnoli, D. R. Napoli, F. Nowacki, J. Ollier, D. O'Donnell, A. Papenberg, G. Pollarolo, M.-D. Salsac, F. Scarlassara, J. F. Smith, K. M. Spohr, M. Stanoiu, A. M. Stefanini, S. Szilner, M. Trotta, and D. Verney. γ-ray spectroscopy of neutron-rich ^{40}S. *Phys. Rev. C*, 81:054305, May 2010.

[94] J. A. Winger, P. F. Mantica, R. M. Ronningen, and M. A. Caprio. Low-energy structure of ^{40}S through ^{40}P β decay. *Phys. Rev. C*, 64:064318, Nov 2001.

[95] B. Fornal, R. H. Mayer, I. G. Bearden, Ph. Benet, R. Broda, P. J. Daly, Z. W. Grabowski, I. Ahmad, M. P. Carpenter, P. B. Fernandez, R. V. F. Janssens, T. L. Khoo, T. Lauritsen, E. F. Moore, and M. Drigert. Gamma ray studies of neutron-rich sdf shell nuclei produced in heavy ion collisions. *Phys. Rev. C*, 49:2413–2418, May 1994.

[96] A. Gade, P. Adrich, D. Bazin, B. A. Brown, J. M. Cook, C. Aa. Diget, T. Glasmacher, S. McDaniel, A. Ratkiewicz, K. Siwek, and D. Weisshaar. In-beam γ-ray spectroscopy of very neutron-rich nuclei: Excited states in ^{46}S and ^{48}Ar. *Phys. Rev. Lett.*, 102:182502, May 2009.

[97] A. Gade, J. A. Tostevin, V. Bader, T. Baugher, D. Bazin, J. S. Berryman, B. A. Brown, C. Aa. Diget, T. Glasmacher, D. J. Hartley, E. Lunderberg, S. R. Stroberg, F. Recchia, A. Ratkiewicz, D. Weisshaar, and K. Wimmer. Single-particle structure at $N = 29$: The structure of ^{47}Ar and first spectroscopy of ^{45}S. *Phys. Rev. C*, 93:054315, May 2016.

[98] Evaluated nuclear structure database. `http://www.nndc.bnl.gov/ensdf/`.

[99] S. Paschalis, I.Y. Lee, A.O. Macchiavelli, C.M. Campbell, M. Cromaz, S. Gros, J. Pavan, J. Qian, R.M. Clark, H.L. Crawford, D. Doering, P. Fallon, C. Lionberger, T. Loew, M. Petri, T. Stezelberger, S. Zimmermann, D.C. Radford, K. Lagergren, D. Weisshaar, R. Winkler, T. Glasmacher, J.T. Anderson, and C.W. Beausang. The performance of the gamma-ray energy tracking in-beam nuclear array GRETINA. *Nuclear Instruments and Methods in Physics Research Section A: Accelerators, Spectrometers, Detectors and Associated Equipment*, 709:44 – 55, 2013.

[100] F. Nowacki and A. Poves. New effective interaction for $0\hbar\omega$ shell-model calculations in the $sd-pf$ valence space. *Phys. Rev. C*, 79:014310, Jan 2009.

[101] D.J. Morrissey, B.M. Sherrill, M. Steiner, A. Stolz, and I. Wiedenhoever. Commissioning the A1900 projectile fragment separator. *Nuclear Instruments and Methods in Physics Research Section B: Beam Interactions with Materials and Atoms*, 204:90 – 96, 2003. 14th International Conference on Electromagnetic Isotope Separators and Techniques Related to their Applications.

[102] A. Gade, J. A. Tostevin, V. Bader, T. Baugher, D. Bazin, J. S. Berryman, B. A. Brown, D. J. Hartley, E. Lunderberg, F. Recchia, S. R. Stroberg, Y. Utsuno, D. Weisshaar, and K. Wimmer. One-neutron pickup into ^{49}Ca: Bound neutron $g_{9/2}$ spectroscopic strength at $N = 29$. *Phys. Rev. C*, 93:031601, Mar 2016.

[103] D. Weisshaar, D. Bazin, P.C. Bender, C.M. Campbell, F. Recchia, V. Bader, T. Baugher, J. Belarge, M.P. Carpenter, H.L. Crawford, M. Cromaz, B. Elman, P. Fallon, A. Forney, A. Gade, J. Harker, N. Kobayashi, C. Langer, T. Lauritsen, I.Y. Lee, A. Lemasson, B. Longfellow, E. Lunderberg, A.O. Macchiavelli, K. Miki, S. Momiyama, S. Noji, D.C. Radford, M. Scott, J. Sethi, S.R. Stroberg, C. Sullivan, R. Titus, A. Wiens, S. Williams, K. Wimmer, and S. Zhu. The performance of the γ-ray tracking array GRETINA for γ-ray spectroscopy with fast beams of rare isotopes. *Nuclear Instruments and Methods in Physics Research Section A: Accelerators, Spectrometers, Detectors and Associated Equipment*, 847:187 – 198, 2017.

[104] L.A. Riley. UCGretina GEANT4. Ursinus College (unpublished).

[105] NuShellX. http://www.garsington.eclipse.co.uk/.

[106] J. W. Olness, E. K. Warburton, J. A. Becker, D. J. Decman, E. A. Henry, L. G. Mann, and L. Ussery. ^{36}S$(t, p\gamma)^{38}$S reaction. *Phys. Rev. C*, 34:2049–2054, Dec 1986.

[107] E. K. Warburton, D. E. Alburger, and G. Wang. Confirmation of the 2805-keV level of ^{38}S. *Phys. Rev. C*, 36:429–430, Jul 1987.

[108] John A. Cameron and Balraj Singh. Nuclear data sheets for A = 38. *Nuclear Data Sheets*, 109(1):1 – 170, 2008.

[109] A. Obertelli, A. Gade, D. Bazin, C. M. Campbell, J. M. Cook, P. D. Cottle, A. D. Davies, D.-C. Dinca, T. Glasmacher, P. G. Hansen, T. Hoagland, K. W. Kemper, J.-L. Lecouey, W. F. Mueller, R. R. Reynolds, B. T. Roeder, J. R. Terry, J. A. Tostevin, K. Yoneda, and H. Zwahlen. Population of bound excited states in intermediate-energy fragmentation reactions. *Phys. Rev. C*, 73:044605, Apr 2006.

[110] R. Chapman, Z. M. Wang, M. Bouhelal, F. Haas, X. Liang, F. Azaiez, B. R. Behera, M. Burns, E. Caurier, L. Corradi, D. Curien, A. N. Deacon, Zs. Dombrádi, E. Farnea, E. Fioretto, A. Gadea, A. Hodsdon, F. Ibrahim, A. Jungclaus, K. Keyes, V. Kumar, S. Lunardi, N. Mărginean, G. Montagnoli, D. R. Napoli, F. Nowacki, J. Ollier, D. O'Donnell, A. Papenberg, G. Pollarolo, M.-D. Salsac, F. Scarlassara, J. F. Smith, K. M. Spohr, M. Stanoiu, A. M. Stefanini, S. Szilner, M. Trotta, and D. Verney. First in-beam γ-ray study of the level structure of neutron-rich ^{39}S. *Phys. Rev. C*, 94:024325, Aug 2016.

[111] J. A. Winger, H. H. Yousif, W. C. Ma, V. Ravikumar, W. Lui, S. K. Phillips, R. B. Piercey, P. F. Mantica, B. Pritychenko, R. M. Ronningen, and M. Steiner. Low-energy structure of neutron-rich S, Cl and Ar nuclides through β decay. *AIP Conference Proceedings*, 455(1):606–609, 1998.

[112] S. R. Stroberg, A. Gade, J. A. Tostevin, V. M. Bader, T. Baugher, D. Bazin, J. S. Berryman, B. A. Brown, C. M. Campbell, K. W. Kemper, C. Langer, E. Lunderberg, A. Lemasson, S. Noji, T. Otsuka, F. Recchia, C. Walz, D. Weisshaar, and S. Williams. Neutron single-particle strength in silicon isotopes: Constraining the driving forces of shell evolution. *Phys. Rev. C*, 91:041302, Apr 2015.

[113] L. A. Riley, P. Adrich, N. Ahsan, T. R. Baugher, D. Bazin, B. A. Brown, J. M. Cook, P. D. Cottle, C. Aa. Diget, A. Gade, T. Glasmacher, K. E. Hosier, K. W. Kemper, A. Ratkiewicz, K. P. Siwek, J. A. Tostevin, A. Volya, and D. Weisshaar. γ-ray spectroscopy of one-proton knockout from ^{45}Cl. *Phys. Rev. C*, 86:047301, Oct 2012.